2008

Dosimetry intercomparison using a 35-keV x-ray synchrotron beam

Scott Oves
Louisiana State University and Agricultural and Mechanical College, soves1@lsu.edu

DOSIMETRY INTERCOMPARISON USING A 35-KEV X-RAY SYNCHROTRON BEAM

A THESIS

Submitted to the Graduate Faculty of the
Louisiana State University and
Agricultural and Mechanical Collage
in partial fulfillment of the
requirements for the Degree of
Master of Science

in

The Department of Physics and Astronomy

By
Scott Oves
B.S. University of Delaware, 2004
May, 2008

Acknowledgements

I offer my sincerest gratitude to Dr. Kenneth Hogstrom for supervising this project, as well as my four other committee members: Dr. Les Butler, Dr. Joe Dugas, Dr. Maurice King, and Dr. Erno Sajo for their insight into the course of my thesis. I wish to acknowledge funding support for this project, including my graduate student assistantship. Funding support included Dr. Hogstrom's startup funds provided by the College of Basic Sciences.

This project would not have been possible without the availability of a wide array of equipment from several institutions. As such, I would like to thank members of the CAMD staff, especially Dr. Kyungmin Ham for the general assistance with the tomography beamline and beam-time scheduling, Dr. Lorraine Day for facilitating the use radioactive calibration sources, and Dr. Amitava Roy his help with the powder diffraction measurements. I thank Angela Stam and Eric Laufenberg of Mary Bird Perkins Cancer Center for help with the ^{125}I and megavoltage film calibrations, respectively. I thank Naresh Tolani of The University of Texas M. D. Anderson Cancer Center at Houston for assistance with and allowing the use of the orthovoltage x-ray machine. I also thank Dr. Kip Matthews for providing the movable stage and assisting with its programming. I am particularly grateful to Dr. Dugas with whom I worked and whom provided daily supervision to me.

Finally, I would like to thank the Yvonne Thomas and Arnell Dangerfield of the LSU Medical Physics Department for help in the administrative aspects of my graduate studies.

Thank you all, truly!

Table of Contents

List of Tables

List of Figures

Abstract

Significance: Photon activated Auger electron therapy utilizes a keV-ranged, monoenergetic x-ray beam, and radiobiological and animal experiments studying this therapy require accurate dosimetry techniques. However, there exist few dosimetry protocols for low-energy x-ray beams. This research intended to use the CAMD synchrotron as a source of monochromatic, 35-keV x-rays and test dosimetry techniques of film and ion chamber. The hypothesis of my research was that depth-dose measured in a PMMA phantom using an air-equivalent ionization chamber and radiochromic film dosimeters in a PMMA phantom irradiated by a 35-keV, monochromatic x-ray beam will agree to within 5% of each other and to within 5% of dose determined from fluence-scaled Monte Carlo dose simulations.

Methods: The narrow beam produced on the CAMD tomography beamline (0.1×2.8 cm^2) was effectively broadened (2.5×2.8 cm^2) by vertically oscillating experimental apparatus. Beam energy selected by the monochromator was verified using a Compton scatterer and powder diffraction methods. Depth-dose in PMMA was measured by an air-equivalent ion chamber using a modified AAPM's TG-61 (100-300 kV) formalism and by Gafchromic EBT film using 125-kVp calibration curves. Depth-dose was also determined from scaling MCNP5 Monte Carlo output by fluence measured using a NaI detector.

Results: The powder diffraction energy measurement agreed closest to the monochromator's setting (mean = -0.1±0.3 keV). Depth-doses performed on 5 separate experimental dates showed that beam fluence did not accurately scale to synchrotron ring current between dates. Depth-dose measurements from ion chamber and film at 2 cm resulted in film-measured dose underestimating ion-chamber measured dose by an average of 5.0±2.1%. Fractional Monte Carlo depth-dose simulations agreed well with ion chamber and film measurements, with

maximum disagreements of 3.9% at 9.0-cm depth and 0.9% at 8.25 cm, respectively. Fluence-scaled, Monte Carlo dose determination overestimated ion chamber-measured depth-dose by 6.4±0.8% and overestimated film-measured depth-dose by 9.1±0.7%.

Conclusions: Results of this research were unable to prove or disprove the hypothesis regarding 5% agreement of ion chamber and film dose measurements. Results also proved the hypothesis false for achieving 5% agreement between either ion chamber-measured dose or film-measured dose and dose determined from fluence-scaled Monte Carlo simulations.

1. Introduction

1.1 K-edge Capture Therapy

K-edge capture therapy, a proposed new radiotherapy paradigm, can be performed by two methodologies: either with chemical radiosensitizers containing Auger-emitting radionuclides or by inducing photoactivation of non-radiolabled drugs via external beam radiation. The research presented in this thesis is concerned with the latter method.

External beam K-edge capture therapy requires the radiosensitizing drug to exhibit two key features: (1) it must incorporate itself preferentially in the DNA of cancerous cells rather than surrounding normal tissues and (2) a high-Z element must be present in the radiosensitizer molecule.

(1) The former feature can be accomplished if the radiosensitizer's molecular structure mimics a component of the DNA molecule. Molecules that are similarly structured to a DNA component will be incorporated in place of the analog molecule during DNA synthesis (Hall *et al*, 2005). This incorporation is expected to be greater for cells undergoing rapid proliferation (e.g. cancerous cells) (Hall *et al*, 2005).

(2) When exposed to keV x-rays, high-Z elements exhibit considerably higher frequency of photon interaction (shown by a larger mass energy absorption coefficient in Figure 1) primarily because of increased photoelectric interactions. As a result, not only does the cancerous DNA experience greater frequency of photon interactions, but the resulting energy released is deposited within a very short range of a few microns through the emission of Auger electrons (see Figure 2 and Figure 3). Consequently, a higher frequency of cell death through DNA double strand breaks is expected per dose delivered to the tumor.

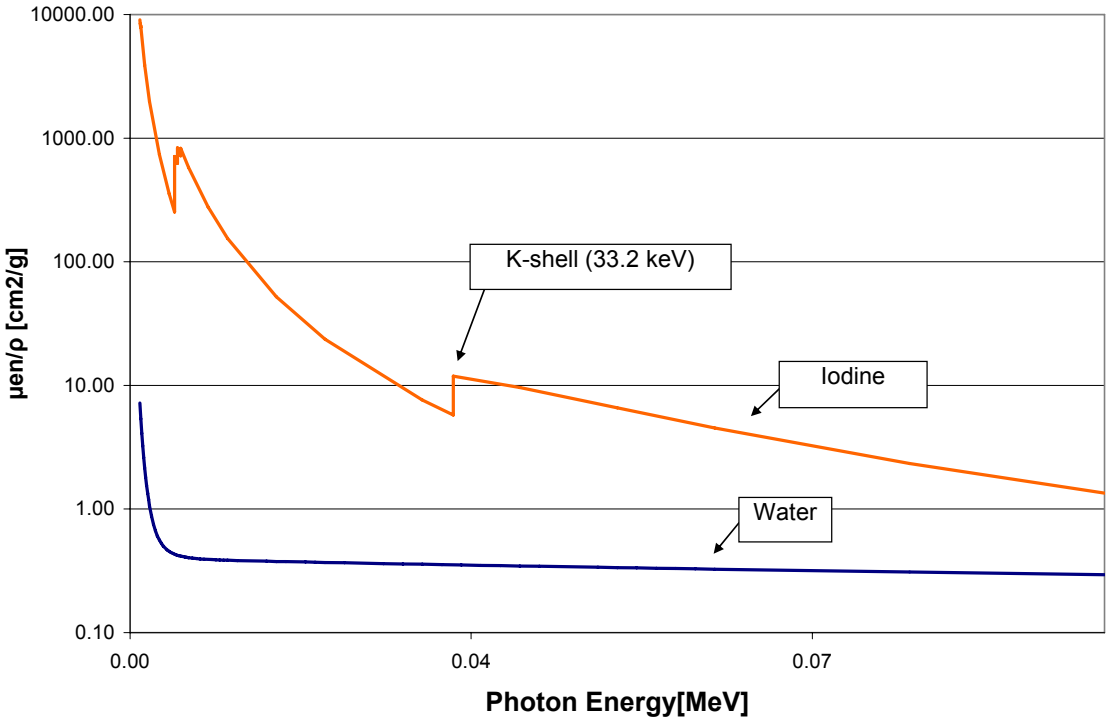

Figure 1: Mass energy absorption coefficients versus photon energy for water and iodine. Values acquired through NIST tables (Hubbell *et al*).

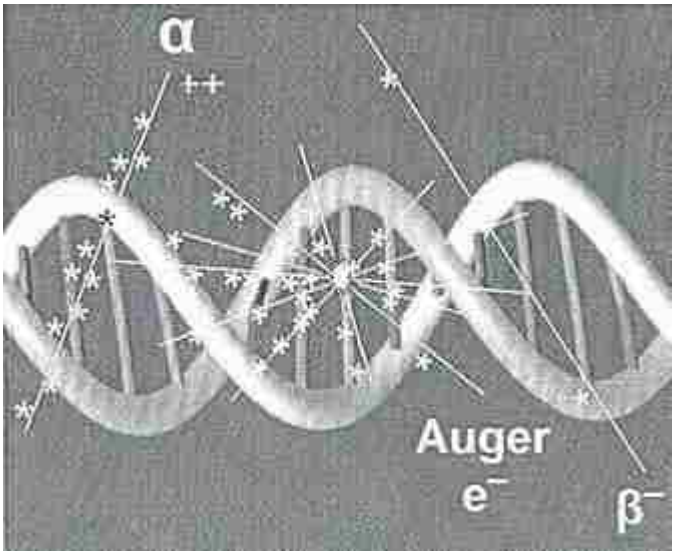

Figure 2: Illustration of the high LET of Auger electrons compared to alpha (α) and beta (β) particles (from Kassis *et al*, 2005).

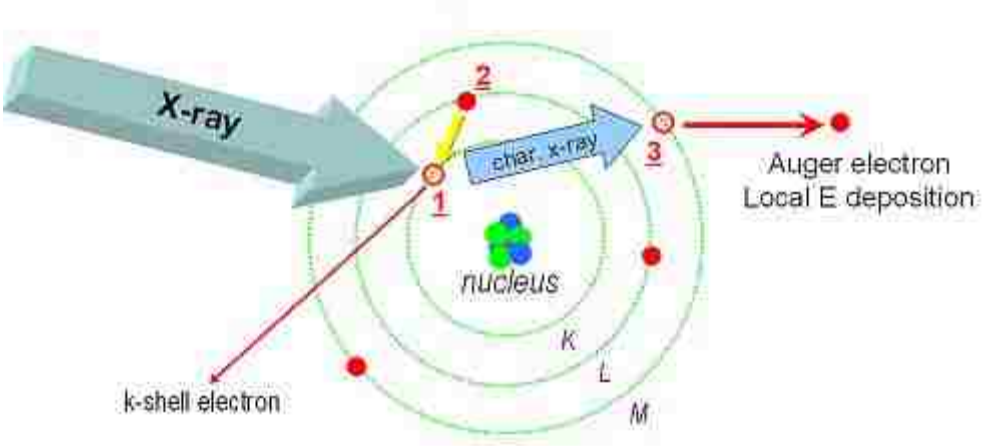

Figure 3: Schematic of Auger electron production from a photoelectric event. 1) Incident x-ray undergoes photo-electric event with orbital electron, 2) higher orbital electron falls to lower shell and emits characteristic x-ray, 3) characteristic x-ray ejects Auger electron.

One potential pharmaceutical that meets the stated criteria is iododeoxyuridine (IUdR), which contains the high Z-element iodine (k-shell binding energy of 33.2 keV). The IUdR molecule is an analog of thymidine, one of the four DNA nucleosides. As shown in Figure 4, thymidine and IUdR are identical except for an iodine atom in place of a methyl group (CH_3). Consequently, IUdR, if present, will replace significant portions of thymidine during DNA synthesis.

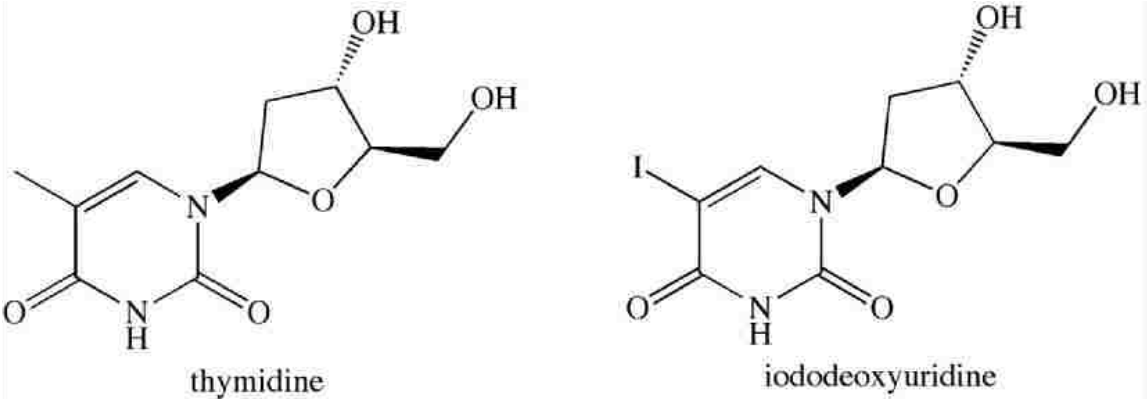

Figure 4: Molecular structures of thymidine and iododeoxyuridine (IUdR).

According to the theory of Auger electron therapy, there should be a significant difference between iodinated cell survival curves established from monochromatic x-ray

beams with energies above and below the iodine K-shell binding energy. To date, a few crucial studies have demonstrated this effect.

One example demonstration is the cell survival curves published by Laster *et al* (1993). In their study, cell survival curves were established from (A) non-iodated control cell culture irradiated with 32.9-keV x-rays (i.e. x-ray energy below 33.2-keV iodine K-shell binding energy), (B) IUdR incorporated cells irradiated with 32.9-keV x-rays, and (C) IUdR incorporated cells irradiated with 33.4 keV x-rays (i.e. x-ray energies above the iodine K-shell binding energies) (see Figure 5).

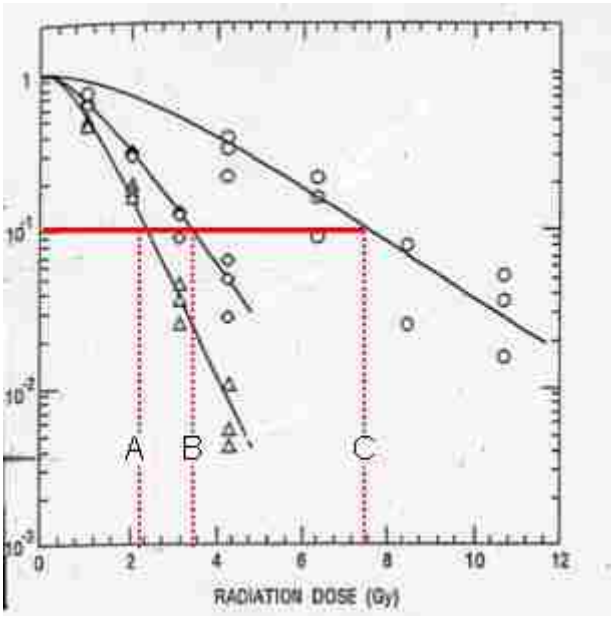

Figure 5: Results from Laster *et al* (1993) showing cell survival curves established from A) IUdR incorporated cells irradiated at 33.4 keV, B) IUdR incorporated cells irradiated at 32.9 keV, and C) IUDR free control cells irradiated at 32.9 keV.

In addition to the reported sensitizing effect (i.e. a 54% decrease in dose from curves C and B to achieve 10% survival), 33.4-keV x-rays were found to be 1.4 times more effective in IUdR incorporated cell killings than 32.9-keV x-rays (i.e. 29% less dose required to achieve 10% survival in curve A compared to curve B) (Laster *et al*, 1993).

Another demonstration of the photo-activated Auger electron therapy are experiments performed by Karnas *et al* (1999), who irradiated IUdR incorporated cells

using filtered kilovoltage x-ray beams with effective energies ranging from 45 to 55 keV. Cell survival curves in this study also showed a sharp increase in cell killing when irradiation was performed with beams of effective energies above the iodine K-shell binding energy (Karnas *et al*, 1999). The increase in cell killing was found to be proportional to the calculated dose enhancement ratio to DNA, which was given as the ratio of mass absorption coefficient of iodinated to non-iodinated DNA (Karnas *et al,* 1999) (Figure 6). The results of Karnas *et al* suggest that the increase in cell killing can be achieved using photon energies not just above the K-shell binding energy but rather in a range of 20 keV above it (Figure 7) implying that Auger electron therapy can be delivered using polychromatic beams.

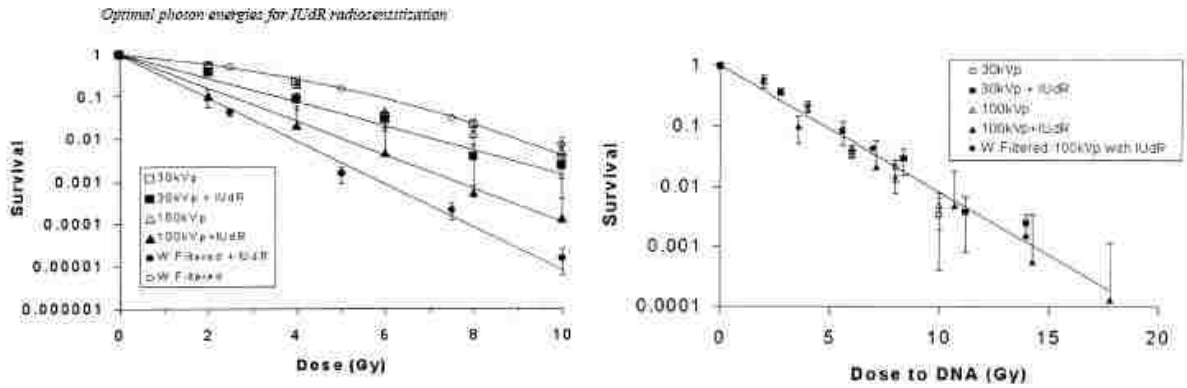

Figure 6: Cell survival curves as a function of delivered dose (left) and dose to IUdR laden DNA (right).

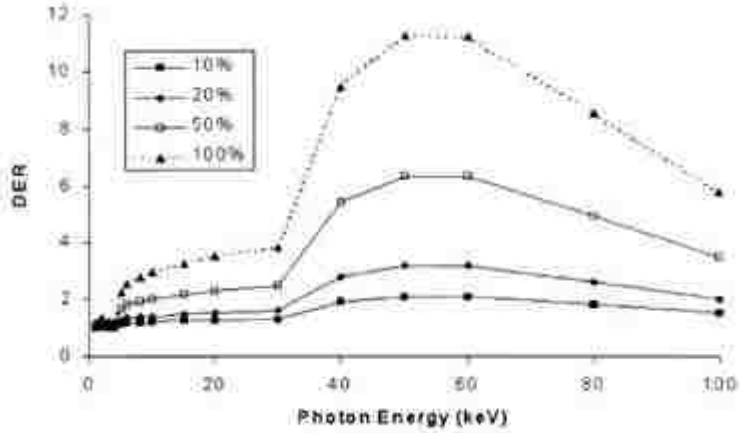

Figure 7: Dose enhancement ratio plotted against photon energy for auger electron therapy according to Karnas *et al* (1999).

Regardless of their absolute necessity in delivering Auger electron radiotherapy, monochromatic x-rays are speculated to be therapeutically advantageous because of the absence of any low energy component in the spectra that should (1) decrease the dose to tissue upstream from the tumor when performing external beam therapy and (2) ensure that most photons that do interact with the tumor will be above the critical K-shell binding energy (Carroll, 2003).

1.2 Monochromatic X-ray Sources

As K-edge capture therapy is theorized to maximize the cancerous-to-normal tissue killing ratio for a small energy range centered above the K-edge binding energy of the radiosensitizing, high-Z element, K-edge capture therapy should utilize tunable monochromatic energy. However, the only sources of monochromatic x-rays available in a clinical setting are radionuclides which cannot be tuned to any optimal energy. Moreover, such sources are expensive and unwieldy; especially if amassed in quantities sufficient to produce a therapeutically useful external beam. Another possible source of monochromatic x-rays would be the use of a monochromator, a devise which generates monochromatic spectra from polychromatic beams, in conjunction with a clinical x-ray therapy machine. However, the process of filtering x-ray spectra is far too inefficient to yield an acceptable fluence rate suitable for patient treatment (Carroll, 2002). As a consequence, sources of tunable monochromatic x-rays have heretofore been limited to powerful synchrotron facilities (Figure 8), which produce a polychromatic x-rays of high enough intensity to allow the use of a monochromator. As these facilities are expensive, their use in cancer therapy has been largely considered impractical in a hospital environment and has been limited to experimental use (Carroll, 2002).

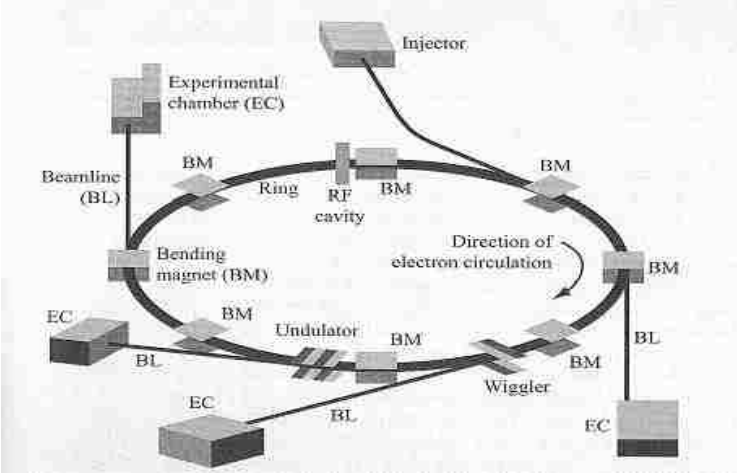

Figure 8: Typical schematic of synchrotron facility (from Margaritondo, 2002).

New modalities of x-ray production, based on the process of inverse Compton scattering, show the potential for being produced in a size and cost that will allow tunable monochromatic x-rays to be delivered in a clinical setting. One example is the MX200 of MXISystems (Carroll, 2002). This process begins with a stream of high energy electrons focused into a narrow beam with another tightly focused beam of photons is sent in the opposing direction of the electrons. Upon interaction, the electrons impart some of their energy to the photons, effectively shortening the wavelengths to the range of x-ray (Figure 9).

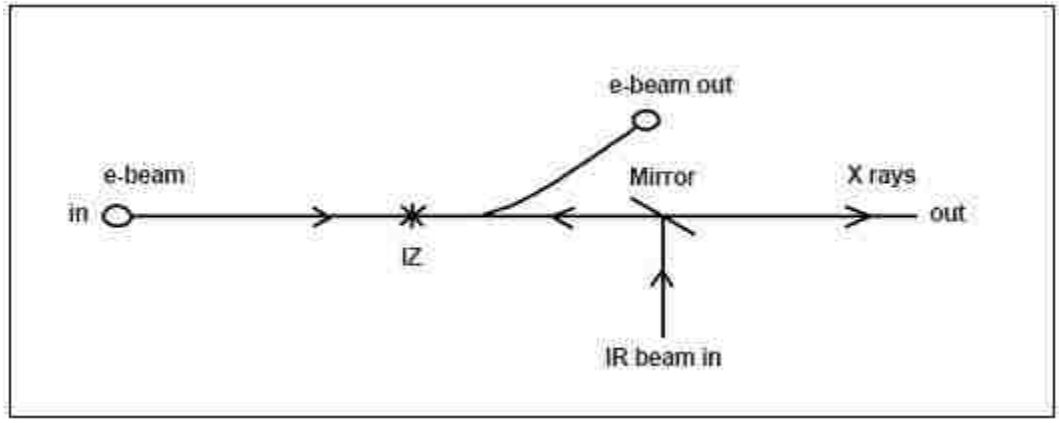

Figure 9: Schematic of x-ray production through inverse Compton scattering (from Carroll *et al*, 2002).

Unlike the traditional three-body interactions occurring in x-ray tubes and linacs (i.e. accelerated electron, target atom, photon), this "inverse Compton scattering" interaction consists of only two bodies (electron, photon). Conservation of energy and momentum dictates that a cone of photons is emitted with a single energy which can be tuned by changing the initial kinetic energy of the incident electrons (Girolami *et al*, 1995).

While such devices may make clinical application of Auger electron therapy a reality they also illuminate the need for experimental determination of the effectiveness of such therapies using monochromatic beams. To that end, the LSU medical physics program is currently pursuing this area.

Our research group has access to monochromatic x-rays from LSU's Center for Advanced Microstructures and Devises (CAMD) synchrotron facility. As stated previously, facilities of this nature are not expected for use with patient trials, but can be used for experiments relevant to developing Auger electron therapy (e.g. cell and small animal irradiations) with proper beam modification and characterization.

1.3 Current Dosimetry Protocols

Currently, there are no existing protocols for dosimetry involving low energy (keV), monochromatic x-rays. The most relevant protocol for a beam of this type is AAPM's TG-61 Report on Kilovoltage X-ray Beam Dosimetry. The protocol is designed for conventional, polychromatic x-ray beam dosimetry using an ionization chamber placed in air or at a reference depth of 2 cm (Ma *et al*, 2001). Previous investigations have also been performed for popular radiotherapy dosimeters using kilovoltage beams. Two types of LiF thermoluminescent dosimeters (TLD), MOSFET semiconductor detectors, two types of radiographic film, and two types of radiochromic films for both monochromatic

(10-99.6 keV) and superficial/orthovoltage (1.4 mm Al to 4 mm Cu HVL) x-ray beams have been studied by Kron *et al* (1998). Using a 0.2-cm^3, thin window, plane parallel-plate ionization chamber to calibrate the synchrotron radiation beams, Kron *et al* (1998) showed considerable variation of detector response with photon energy, particularly for the MOSFET detectors and radiochromic film (Figure 10).

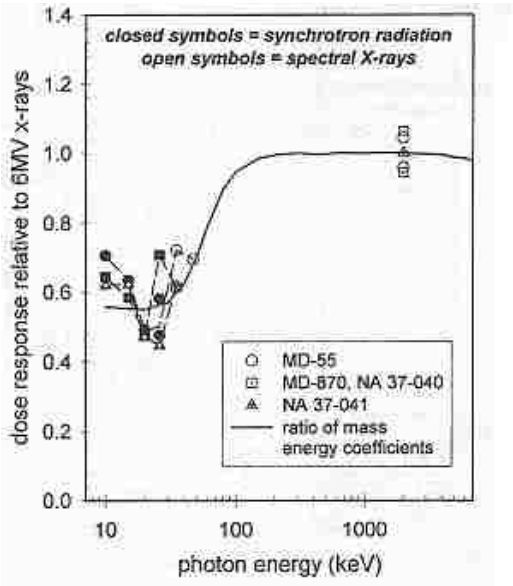

Figure 10: Various radiochromic film responses from kilovoltage and megavoltage exposures as shown by Kron *et al* (1998).

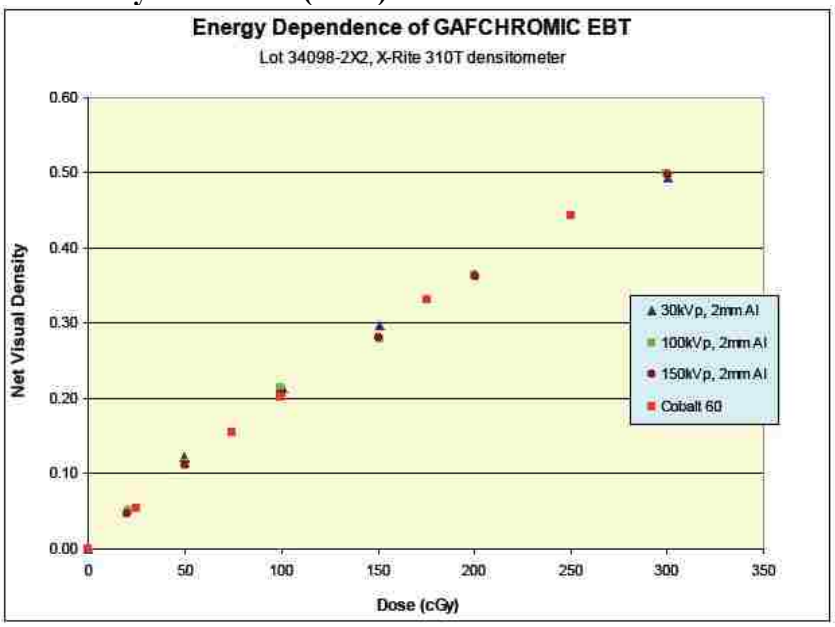

Figure 11: Net visual density of EBT Gafchromic film against various delivered doses. (from ISP Gafchromic EBT white paper, 2005).

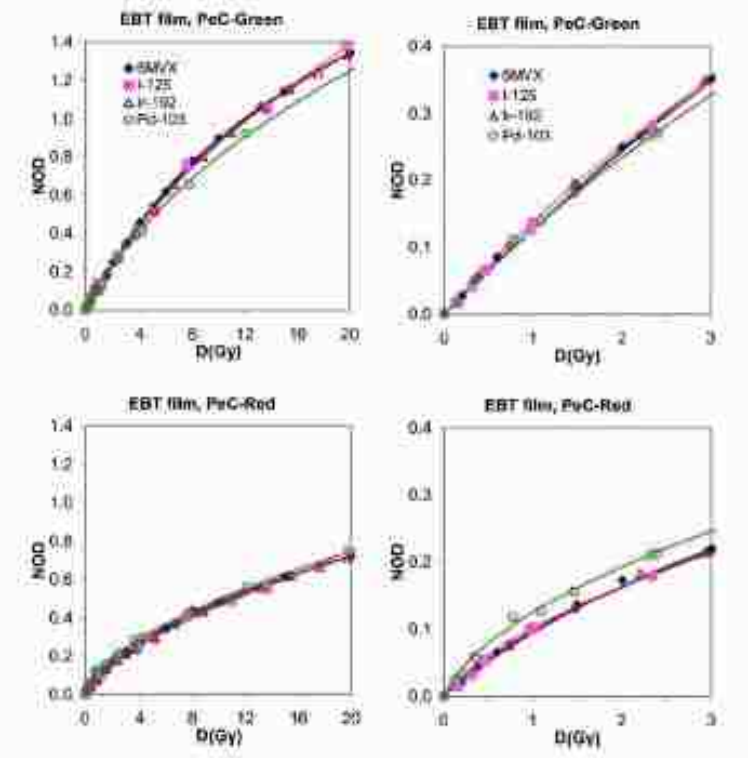

Figure 12: Results from Chiu-Tsao *et al* (2005) comparing film-dose curves established by several radionuclides and 6MV external beam.

More recently, Gafchromic EBT® (International Specialty Products, Wayne, NJ, USA) radiochromic film was reported to have little variation in its optical density versus dose calibration curves for 30-kVp, 100-kVp, 150-kVp, and ^{60}Co beams (ISP, 2007) (Figure 11). It is stated in the product's white paper (ISP, 2007) that the greater energy independence over other Gafchromic models is due to the inclusion of chlorine atoms in the film's active layer. The addition of chlorine increases the effective atomic number thereby increasing the film's sensitivity to dose at low photon energies and lessoning the megavoltage-kilovoltage film response discrepancy observed by Kron *et al* (1998).

Similarly, Chiu-Tsao *et al* (2005) showed little difference in optical density versus dose of EBT film irradiated using ^{125}I, ^{192}Ir, ^{103}Pd, and 6 MV x-ray beams when digitized using a red (665 nm) light source (Figure 12). However, Butson *et al* (2006) showed a somewhat different result with a 7% lower response from a 50-kVp beam (28-keV

effective energy) as compared to the same 2-Gy dose delivered from a 6 MV beam (Table 1).

Table 1: Results of Butson *et al* (2006) showing difference in film response from 2-Gy exposure established from several conventional beams.

Effective Energy		Relative Response
(keV)	(kVp)	(±0.037, SD)
28	50	0.923
32.5	75	0.926
39	100	0.93
53	125	0.929
68	150	0.928
94	200	0.946
119	250	0.956
1500	6000	1
5500	18000	0.996

Edwards *et al* (1997) investigated the sensitivity (response per unit air kerma rate) of MOSFET, p-type semiconductors, and LiF:Mg:Ti TLD dosimeters for quasi-monoenergetic x-ray beams having mean energies ranging from 12 to 108 keV relative to that for a 6 MV x-ray beam. Their results showed significant variation in sensitivity with mean x-ray energy for all detectors, being least for the LiF TLD. Boudou *et al* (2004) investigated the use of Fricke gel dosimetry for measuring two-dimensional dose distributions with a 78.8-keV synchrotron-generated photon beam by comparing them with MCNP-calculated dose distributions, showing good agreement.

In the present study, both an air-equivalent ionization chamber and Gafchromic® EBT radiochromic film were used to measure depth dose in a polymethylmethacrylate (PMMA) phantom. These dosimeters were selected because their sensitivity reportedly does not vary significantly with photon energy. We expect these dosimeters to be useful for Auger electron therapy studies of treatment planning, cell irradiations, and small animal irradiations at the CAMD synchrotron facility.

1.4 Hypothesis and Specific Aims

The hypothesis of this thesis is that depth-dose measured in a PMMA phantom using an air-equivalent ionization chamber and radiochromic film dosimeters in a PMMA phantom irradiated by a 35-keV, monochromatic x-ray beam (CAMD tomography Beamline) will agree to within 5% of each other and to within 5% of dose determined from fluence-scaled Monte Carlo dose simulations.

Four specific aims have been completed in order to test this hypothesis:

1) Beam Configuration and Characterization: configure the CAMD x-ray tomography beamline for experiments in Auger electron therapy and measure its beam properties.
2) Ion chamber Depth-Dose Measurements in PMMA: measure dose to water versus depth in a PMMA phantom using an air-equivalent ion chamber.
3) Film Depth-Dose Measurement in PMMA: measure dose to water versus depth in a PMMA phantom using radiochromic EBT film.
4) Comparison of Measurements with Fluence-Based Dose Calculations: compare results of film and ion chamber dose measurements to dose determined from fluence measurements and MCNP5 Monte Carlo.

2. Aim 1, Beam Configuration and Characterization

Configure the CAMD x-ray tomography beamline for experiments in Auger electron therapy and measure its beam properties.

2.1 Goal

To configure the CAMD tomography beamline such that the beam satisfied two criteria: (1) that the beam be monochromatic (35 keV) with insignificant low energy contamination and (2) that the beam be broadened to a size suitable for radiation biology cell and small animal irradiation. Further, to ensure that experiments are relevant to K-edge capture therapy and for subsequent fluence based beam simulation, the beam's mean energy and the relative dose distribution across the beam's axial plane was measured.

2.2 Theory of Beam Modification and Characterization

There are three main assertions in the approach to beam modification and characterization. They are:

1) The beam spectrum can be filtered, if needed, by passing the beam through a low-Z material to attenuate any low energy contamination.
2) A broad beam irradiation can be adequately simulated by modulating the experimental apparatus through the narrow beam (0.1×2.8 cm^2).
3) The mean beam energy can be measured using a number a NaI scintillation detector and powder diffraction-based film measurement.

2.3 Materials and Methods

2.3.1 Photon Production

X-rays were produced at the LSU CAMD synchrotron by passing a 1.3-GeV electron beam (I_{max} = 200 mA) through a 7-T superconducting wiggler. The resulting

polychromatic beam was passed through a double multilayer monochromator (Oxford Danfysik, UK) to generate a monochromatic 35-keV beam (Figure 13). The monochromator was calibrated by CAMD by measuring transmission of photons through targets with different K-edges (see section 2.3.5.3.). Beam restrictions due to the synchrotron, wiggler, monochromator, and beam slits resulted in a beam that was approximately 2.8-cm wide × 0.1-cm high beam.

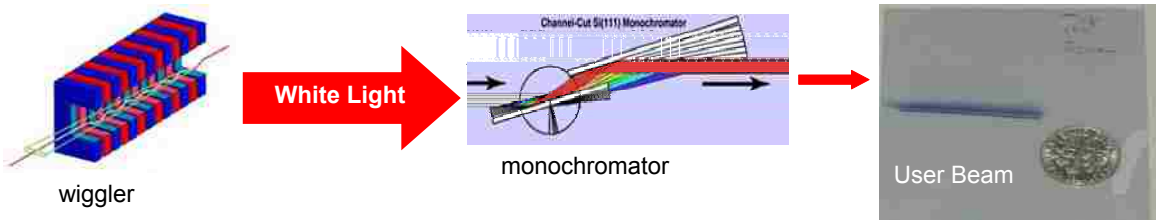

Figure 13: Simplified schematic of filtered monochromatic x-ray production on tomography beamline.

Due to beam loss in the synchrotron, the number of electrons cycling the storage ring decreases with time after initial injection (I<200mA); therefore, the photon intensity produced by these electrons passing through the wiggler simultaneously decreases. Intensity of the beamline was assumed to be linearly proportional to the fluence of electrons in the ring (measured in milliamps by a CAMD solenoid). Dose rate delivered to any apparatus in this study was assumed proportional to measured electron intensity, i.e. all dose measurements were scaled by the average beam current present during their exposure. Specifically, all fluence and dose measurements contained in this paper were linearly scaled to 100 mA electron beam current.

2.3.2 The Tomography Beamline

A schematic of the tomography beamline shown in (Figure 13) includes monochromator and experimental hutch. The allocated space in the experimental beam hutch was on the order of a square meter. Photons entered the hutch through a Kapton® window and passed 10 cm upstream to tungsten collimators (Figure 14 B), which were adjustable in

the vertical direction. The un-collimated x-ray beam profile exhibited secondary photons above the primary beam (Figure 15). To remove this and create a more uniform beam, collimators were used that limited the vertical beam expanse to approximately 1 mm.

The beam energy was set to the requested energy by CAMD personnel. This beam energy was determined at CAMD through calibrations of the monochromator using a K-edge absorption techniques in which beam intensity was measured after passing through a known target as a function of monochromator setting. As the monochromatic beam is passed through a given target, charge (exposure) is measured in two ion chambers located downstream of the target. When monochromator settings (spacings and angles of two parallel crystal planes) are adjusted to sweep across a range of beam energies, a clear jump is seen as the K-edge of the absorber material (e.g. Ag at 25.5 keV, Sn at 29.2 keV, etc) is crossed. Figure 16 shows several energy-versus-exposure curves for several materials, and the K-shell binding energy for each was correlated to the points of inflections on the jumps. Because the K-shell binding energy of each absorber material is well known, this method allows for determination of the beam energy to within ± 0.1 keV or better. The accuracy of energy, when set by the monochromator is not specified by CAMD, but is assumed to be ±0.5 keV or better.

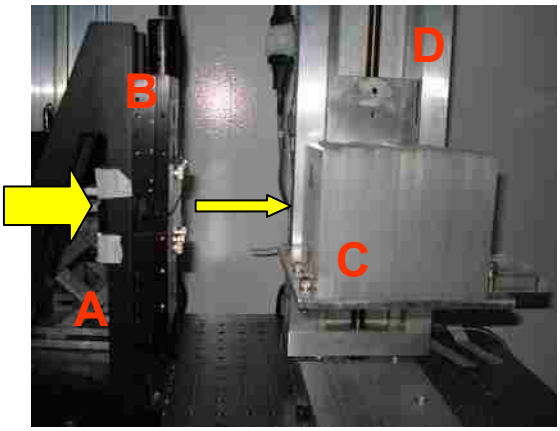

Figure 14: Photograph of tomography beamline's experimental hutch: A) Beam filtration (not seen), B) Tungsten collimator, C) PMMA slab phantom, D) Vertical motion stage.

Figure 15: Sample film shot of uncollimated, un-broadened beam. White arrow indicates vertical direction of the beam.

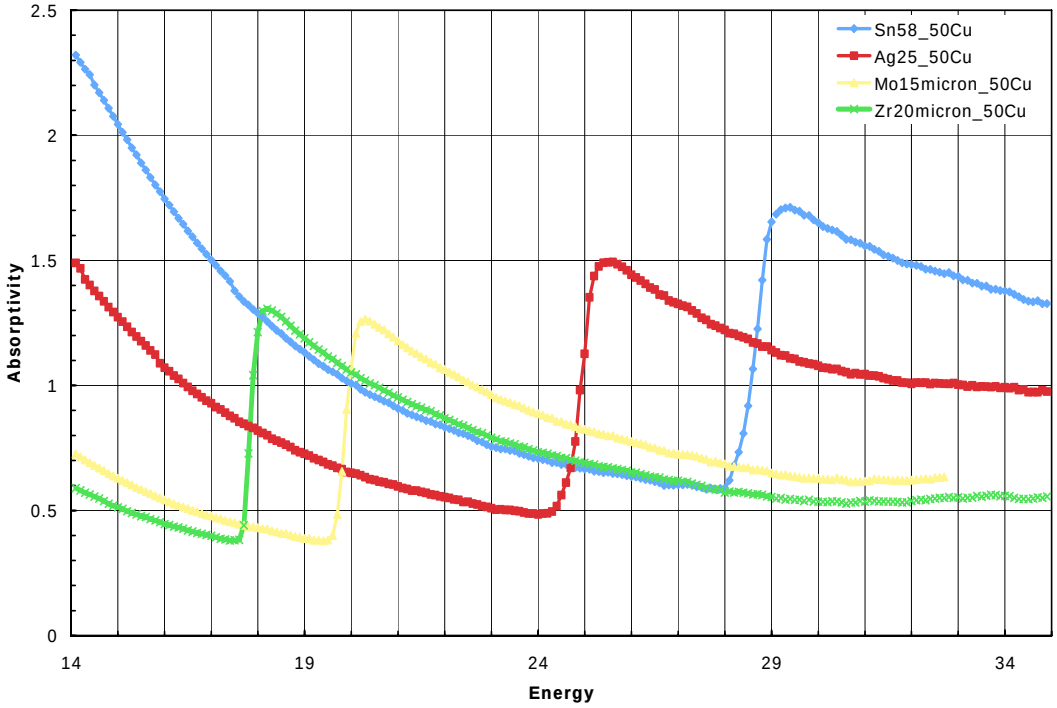

Figure 16: Results of K-edge spectroscopy.

2.3.3 Low Energy Filtration

An energy spectrum of the beam was calculated from measuring the energy spectrum of photons Compton scattered off a thin polyethylene scattering foil using a NaI(Tl) detector (Figure 17).

The experimental setup was identical to that used when obtaining data for Compton spectroscopy measurements and will be explained in Section 2.3.5.1 in greater detail. Early spectral analyses showed that a typical beam spectrum included a significant fraction of low-energy photons with energies from 0 to 10 keV (Figure 17). This contamination was removed using an aluminum foil of 800 μm thickness placed immediately upstream of the vertically-spaced tungsten collimators (Figure 14 A). The low energy component of the beam was reduced to less than 5% of its original intensity as shown in Figure 17. The peak centered around 8-12 keV that remains after filtration, shown in Figure 17, are iodine escape peaks and not a remaining of portion of the low energy contamination

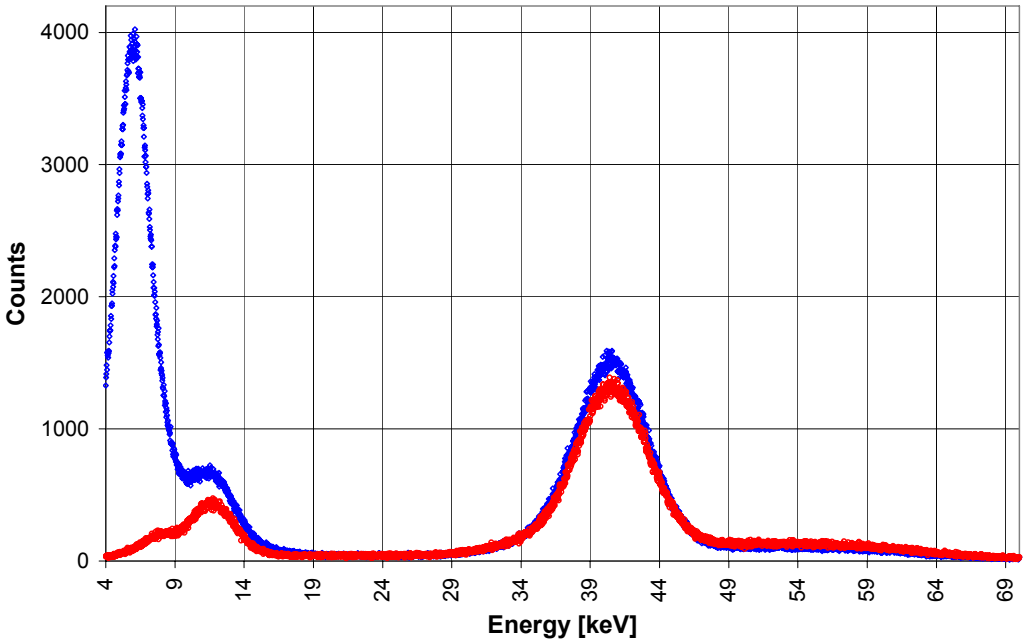

Figure 17: Calibrated MCA data showing Compton spectra taken at θ=45° with (red) and without (blue) aluminum filtration.

2.3.4 Beam Modulation

The narrow beam produced by the CAMD tomography beamline (0.1×2.8 cm^2) does not irradiate a large enough area to be useful for cell and animal irradiations. Because uncharged photon beams cannot be scanned as can charged particle beams, a broad beam in the experimental reference frame was achieved by oscillating the experimental apparatus across the fixed narrow beam. This was accomplished by mounting the apparatus on a screw-drive stage (Figure 18) with movement programmable in the vertical direction.

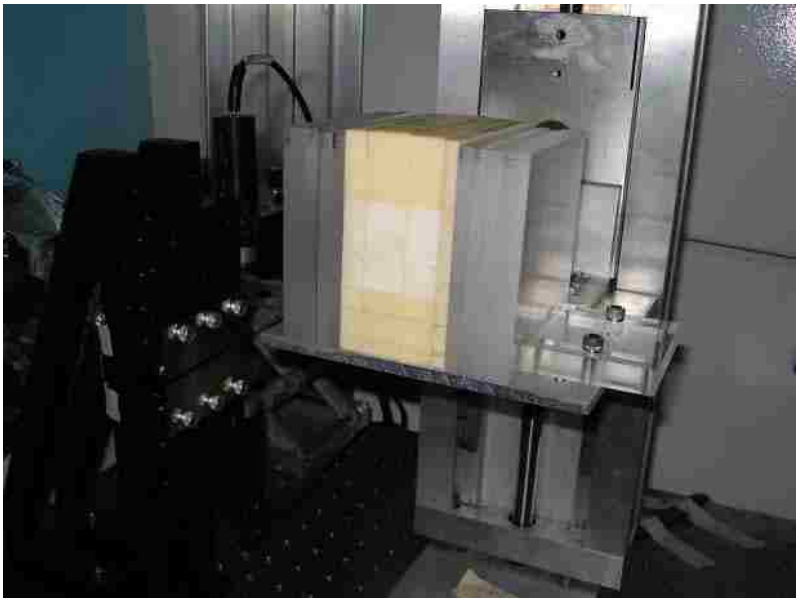

Figure 18: PMMA and lung equivalent slabs positioned on the programmable stage.

Upon commencing the scanning operation, the stage moved the apparatus rapidly downward until the beam was incident on the bottom edge of the area to be directly exposed. At this point the stage was slowly moved through a triangular waveform for a prescribed number of periods. Upon completion, the stage was rapidly moved upward to its original position. The scanning system was controlled by a computer using the computer program LabView, which allowed the user to specify the initial and final positioning, the speed of stage movement across the triangular wave form, the amplitude

of the wave, and the number of periods that irradiation took place resulting in a pattern of motion show in Figure 19.

When performing central-axis depth dose measurements (see sections 3. and 4.), the parameters were set as follows: (1) the speed of movement was 0.125 $cm \cdot s^{-1}$, sufficiently low as to minimize the change in exposure time due to change in acceleration at the stage's lowest and highest position; (2) the amplitude of the beam was set to 2.5 cm; and (3) the number of periods was set to eight, giving a total irradiation time of 320 seconds.

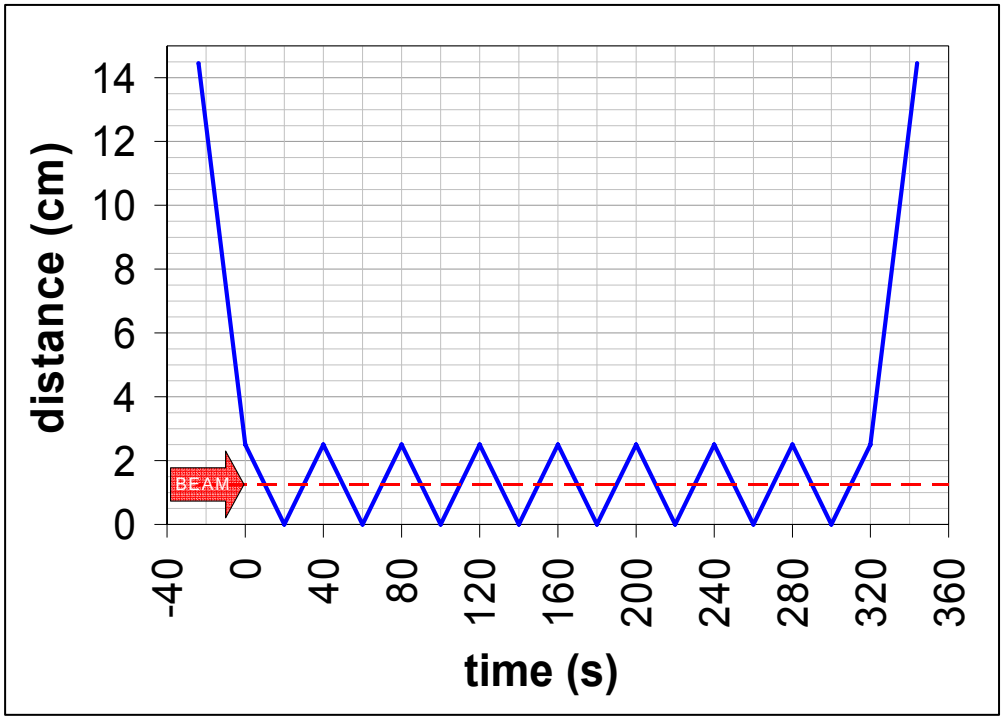

Figure 19: Example of programmed stage movement where distance zero represents the bottom edge of the broad beam.

2.3.5 Mean Energy Measurements

The beam's mean energy was measured using two independent techniques: Compton spectroscopy (section 2.3.5.1) and Powder Diffraction (section 2.3.5.2.). Results of the two measurements were compared to the K-edge calibrated monochromator's setting.

2.3.5.1 Compton Spectroscopy

The mean beam energy was measured from calibrated spectra of photons Compton-scattered through known angles using a scintillation detector. A scintillation detector's active volume consists of a transparent sodium iodide crystal which converts a particle's kinetic energy to light through a process called prompt fluorescence (Knoll, 2000). Each particle's interaction is assigned to a bin number, proportional to its energy, based on the light yield of the particle's interactions. By calibrating the scintillation detector to a source of radiation with known energy (e.g. radionuclides), output channel number can be correlated to a value of energy. Thallium doped sodium iodide, NaI(Tl), is a commonly used scintillation material for routine gamma-ray spectroscopy because of the NaI crystal which forms the active volume provides a high light yield and is easily manufactured in various sizes (Knoll, 2000).

The detector used for these experiments was a 0.1-cm thick, 2.54-cm diameter NaI(Tl) crystal scintillation detector (Alpha Spectra, Grand Junction, CO) with a 0.0254-cm thick beryllium entrance window. The scattering target was a thin sheet of polyethylene (either 50 or 80 mg-cm^{-2}). Detector high voltage was provided by a Canberra Model 3005 power supply. Detector output was amplified by an Ortex 575A amplifier and analyzed with a Canberra Series 10 multi-channel analyzer (MCA). MCA spectra were transferred to a PC for subsequent analysis. Both the high voltage power supply and the amplifier were positioned within the experimental hutch, but well out of the path of the incident x-ray beam. The MCA and PC were located outside the hutch for all exposures.

As the beam was too intense to allow direct acquisition of beam spectra using a NaI(Tl) detector, an alterative method was implemented which measured the energy

photons scattered through well defined angles was utilized. From two-body kinematics, the scattered photon energy can be related to incident energy as a function of scattering angle by:

$$E' = \frac{E}{1 + \frac{E}{m_o c^2}(1 - \cos\theta)} \qquad \text{(2-1a)}$$

and

$$E = \frac{E'}{1 - \frac{E'}{m_o c^c}(1 - \cos\theta)} \qquad \text{(2-1b)}$$

where:

E' is the scattered photon energy,

E is the initial photon energy,

$m_o c^2$ is the electron rest energy (511 keV), and

θ is the angle subtended by the initial and scatter photon trajectories.

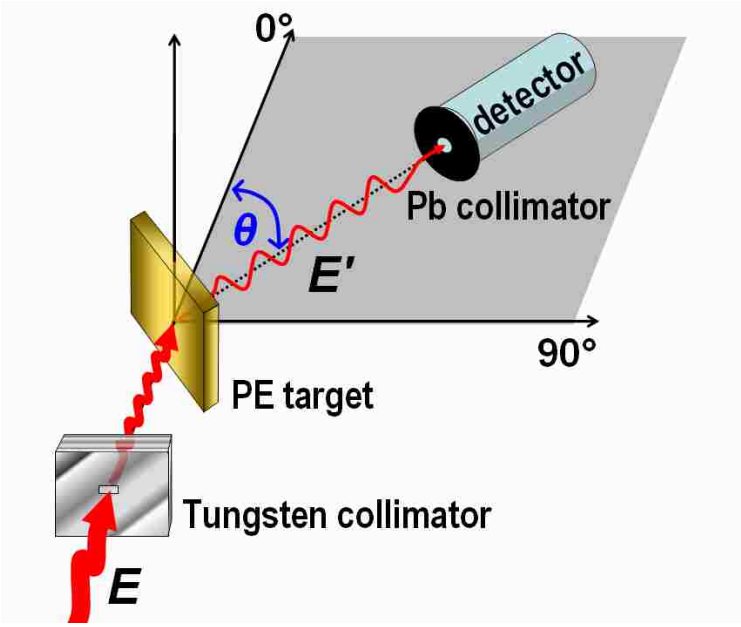

Figure 20: Compton spectroscopy apparatus.

The NaI(Tl) detector was placed in the spectrometer apparatus shown in Figure 20, which consisted of a scattering target, a detector holder that shielded the detector from background radiation, and an aluminum base plate that allowed for accurate positioning of components. The base plate was a ¼" thick aluminum plate. The top surface of the plate was marked in 5° increments from 0° (parallel to the beam's axis) to 90°. The detector and scatterer holder were pivoted on the base plate such that the beam was centered on the scatterer with the detector's face remaining parallel to the plane of the scatterer and the scatter to detector distance being 39.7 cm.

The narrow beam was collimated in the horizontal direction using tungsten slits yielding an approximately 0.1×0.3 cm^2 beam area, which was measured by exposing a film placed immediately downstream of the collimator. A lead aperture (0.171 or 0.195 cm^2) was centered over the beryllium window of the NaI(Tl) detector defining its active area. Compton scattered spectra were acquired for 1000 seconds at angles, θ, of 15º, 30º, 45º and 60º. For each angle, a separate acquisition was taken with no scatterer; and resulting spectra were subtracted from the corresponding readings to correct for background radiation.

Isotopes, ^{55}Fe (E_γ = 5.9 keV) and ^{241}Am (E_γ = 13.9, 17.8, and 59.5 keV) were used to calibrate the detector. Sources were located on the cylindrical axis of the NaI crystal, approximately 20 cm from the face with the detector's lead collimator in place.

Experimental data indicated that percentage of detector face irradiated, the distance between detector and source, and the detector warm-up time affected channel number of the peaks. For these reason, the setup radioactive calibration sources was designed to closely resemble beam irradiation as possible: the detector was collimated

when irradiated by the source; sources were placed as far away from the detector as possible; and the detector was given several hours to warm-up before analysis.

All spectral data was uploaded to a PC, the peaks were fit to Gaussians using Sigma Plot™ (Systat Software Inc, San Jose, CA). Scintillation detectors have a significant stochastic error in energy measurements ($\Delta E/E \approx 10\%$). As a result, energy spectra from such sources are displayed on the MCA as a series of broad peaks rather than discrete energies. Figure 21 shows a typical calibration acquisition. The channel numbers located at the peak centroids, were taken as those corresponding to the known source emission energies. Plots of characteristic energies versus MCA channel number were fit with a linear trend-line by means of the method of least squares (Figure 22). The equation of the trend-line served as the conversion from channel number to energy. Figure 23 shows two typical Compton Spectroscopy measurement with channel numbers converted to energies using the described calibration method.

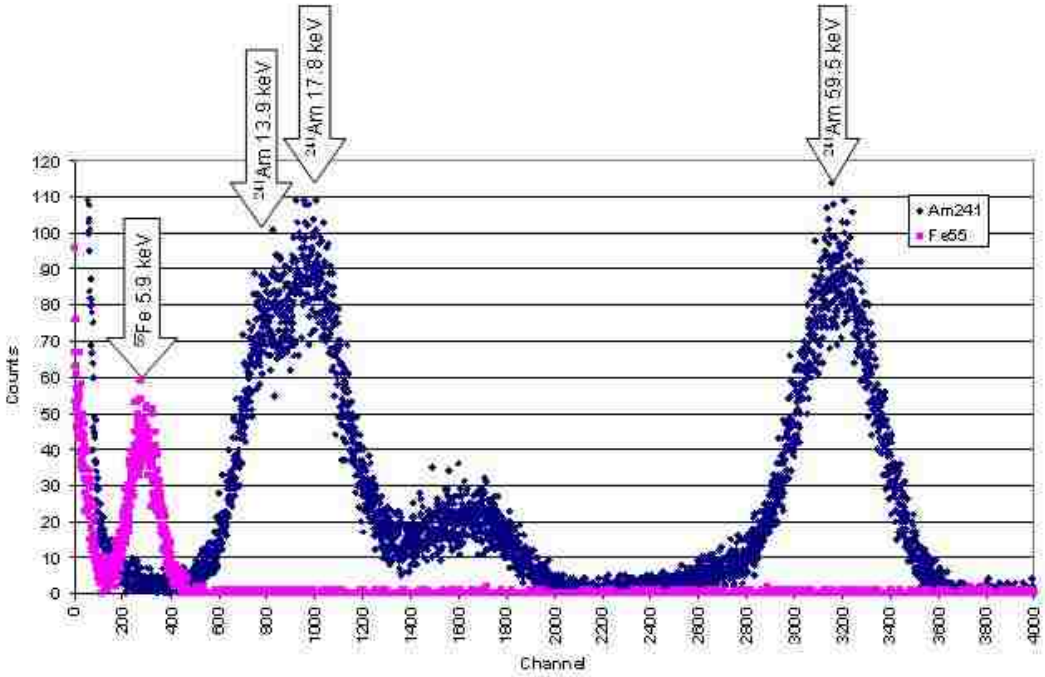

Figure 21: Sample NaI(Tl) detector spectral acquisition with radionuclides energies (keV) identified. The escape peak centered around 1600 was not used.

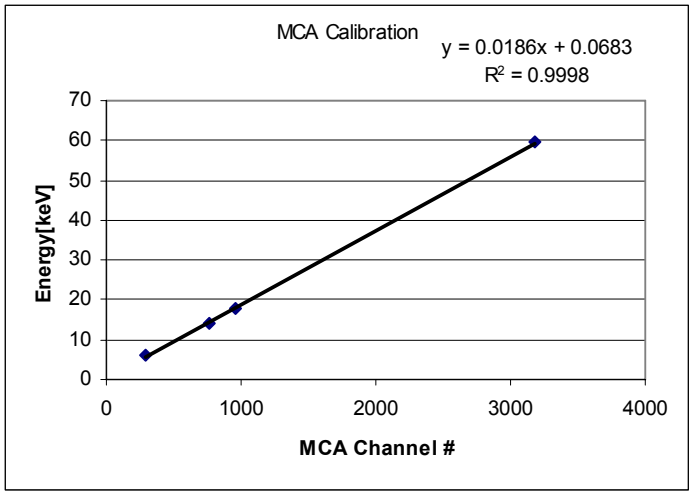

Figure 22: Example of calibration peak centroid channels plotted against corresponding characteristic energies.

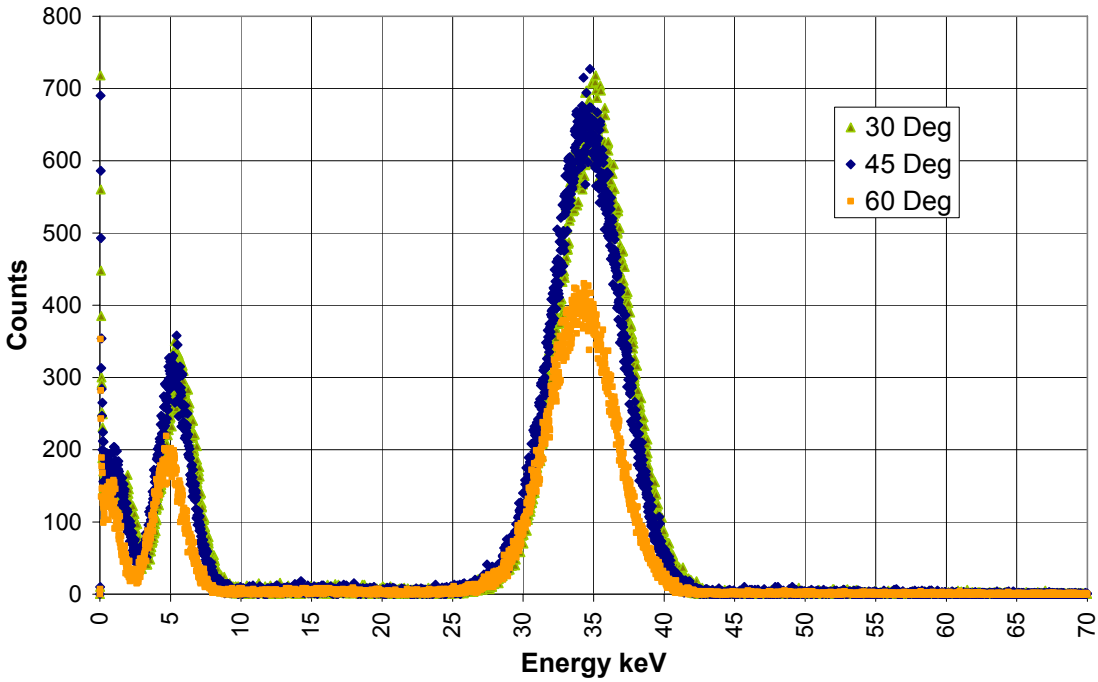

Figure 23: Compton spectra obtained at 30, 45 and 60 degrees from uncollided beam path.

2.3.5.2 Powder Diffraction Spectroscopy

In the application of x-ray powder diffraction, x-rays penetrate a sample of crystalline powder (i.e. isotropic distribution of crystal planes), resulting in coherent scattering that exhibits maxima (scattered radiation that constructively interferes) at discrete angles measured from the initial beam path (i.e., in two dimensional cones called

Debye-Scherrer cones), as shown in Figure 24. The angle between the beam axis and the cone equals 2θ, where θ is the Bragg angle defined in Figure 25. The discrete angles that these maxima occur satisfy Bragg's Law:

$$n\lambda = 2d\sin(\theta) \qquad (2\text{-}2)$$

where:

d is any lattice spacing of the crystal sample,

λ is the incident x-ray wavelength,

n is an integer, and

θ is half the angle measured from initial beam path to the resulting maxima shown in Figure 25.

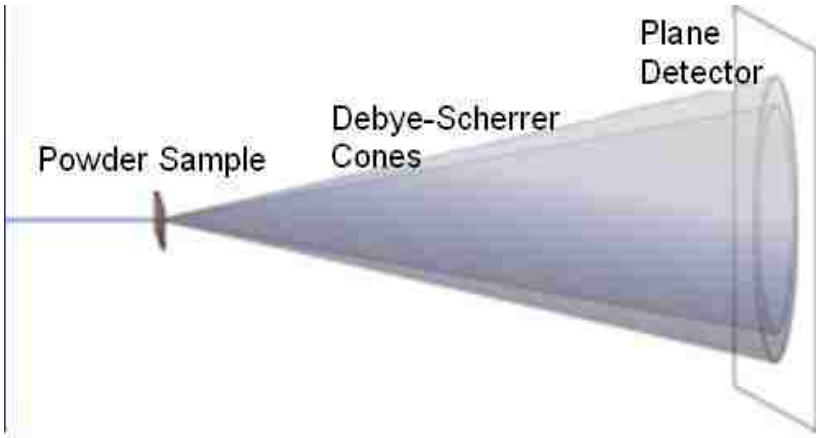

Figure 24: Illustration of x-ray powder diffraction taken from using Debye-Scherrer setup (http://en.wikipedia.org/powder_diffraction).

The value n indicates that for every wavelength satisfying the Bragg's law equation at a lattice spacing, d, and angle, θ, photons of multiple wavelengths will also satisfy it. As the CAMD tomography beamline is functionally monochromatic, n can be set to unity for the purposes of energy measurements.

By irradiating a crystalline powder of known lattice spacings *d*, and measuring the angular divergence of the Debye-Sherrer cones (2θ), Bragg's law allows the calculation of photon wavelength λ and also energy ($E = h\frac{c}{\lambda}$) by extension.

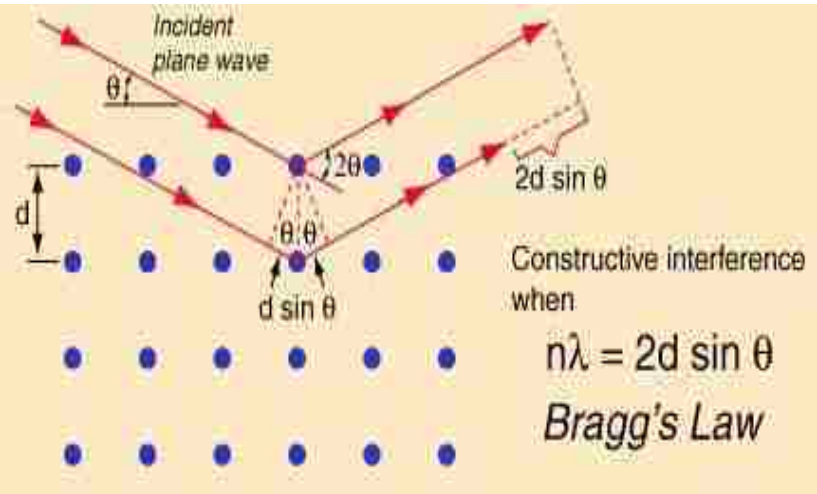

Figure 25: Illustration constructive interference of coherently scattered x-rays from a crystalline lattice. Notice that the angle between constructive interference and uncollided beam is *2θ* (http://hyperphysics.phy-astr.gsu.edu/hbase/quantum/bragg.html).

The sample used was silicon with space group 640c (Si640c), a common standard, meaning that its lattice properties are well known, and is regularly used to calibrate x-ray diffraction equipment. Lattice parameters corresponding to the brightest x-ray maxima are displayed in Table 2.

For the measurement setup, the Si640c sample was held in a 3-mm PMMA slab with a 45^{o} cone milled into its center (Figure 26). The crystalline powder was packed into the conical opening and held in place using Scotch® tape.

The sample holder was placed with the small cone entrance facing the beamline window. It was then raised to a height such that the beam axis was coaxial with the conical sample. Tungsten blocks were placed upstream from the sample holder to collimate the beam in the horizontal direction. The resultant beam had a cross-section of

approximately 2×2 mm^2. A single sheet of radiographic EDR2 film (selected because of its availability) was placed approximately 10 cm downstream from the powder sample, upright against a Styrofoam block (Styrofoam material chosen to minimize backscatter) and normal to the beam path. After completing the exposure, the process was repeated for three more films with each film being placed at increasingly greater distances from the powder sample, in approximately 7-cm increments. The exposure time for each film was approximately five minutes for every 7-cm distance from the sample. Films were developed with a KODAK X-Omat 2000 Processor located at Mary Bird Perkins Cancer Center within twelve hours of exposure. Developed films were digitized by an EPSON 1680 flatbed scanner using the program Image Acquisition® (ISP, Wayne, NJ), scanned at 300 dpi, and saved as TIF files. Because the films were placed normal to the beam path, the developed films displayed a series of rings with radii that increased linearly with distance from the powder sample.

Image analysis was performed using the image manipulation program ImageJ (NIH, Bethesda, MD). Film images were processed with a bandpass Fourier filter which smoothes the graininess of the film by subtracting higher frequencies and eliminating exposure from non-coherent scattering by subtracting lower frequencies (Figure 27 illustrates this process).

Table 2: Lattice spacings, d, corresponding to the three brightest Debye-Scherrer cones in order of intensity with values obtained from dividing the Si640c lattice parameter, a, (available through NIST) by the square root of the sum of the Miller indices, h, k, l.

a = 0.54312 Å			
d(Å)	**h**	**k**	**l**
3.1355	1	1	1
1.9201	2	2	0
1.6375	3	1	1

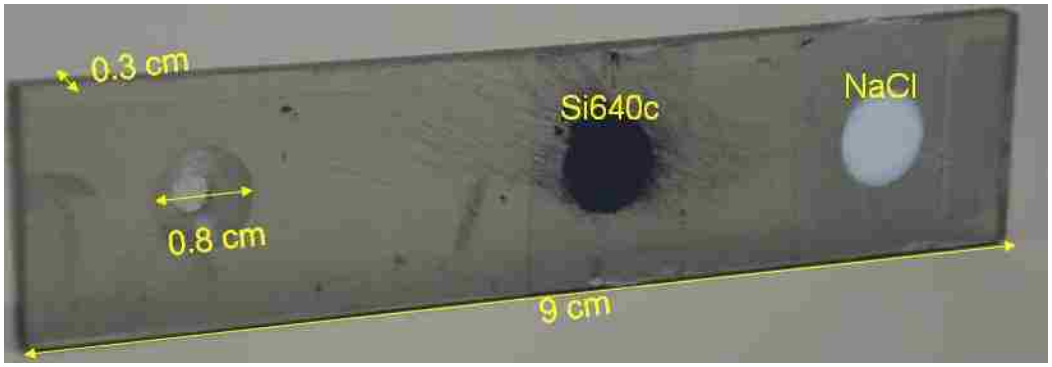

Figure 26: Image of Si640c in sample holder which contained three identical 45º cone mills. (left mill) no powder sample showing scale; (center mill) Si640c; (right mill) NaCl not used in this study.

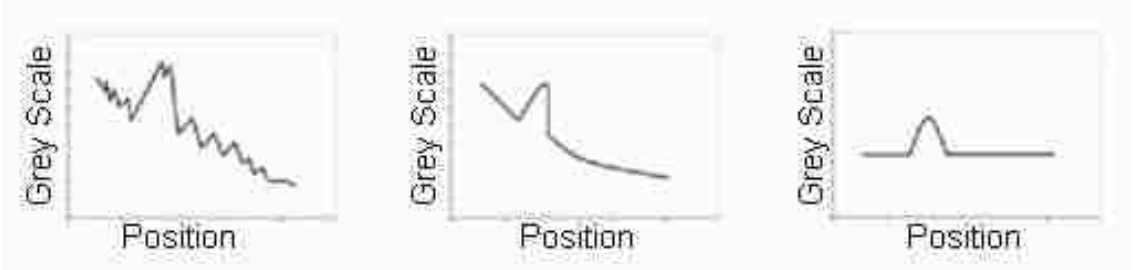

Figure 27: Theoretical line profiles crossing a diffraction ring on film images (left) unfiltered, (center) high pass filtered, and (right) band pass filtered.

The ring diameters were determined using the following steps: first, a line segment was constructed connecting any two points of the same ring; second, the point equidistant between the two ring intersections was located; third, a line containing this point and perpendicular to the previous line was constructed and taken as the profile in which ring diameters (i.e. distance between peak pixel values) were measured.

Figure 28: Powder diffraction experimental apparatus.

Since the powder sample was not a point, it was difficult to determine the distance between the effective center of the sample and the film and thus, the angle θ by means of a single direct measurement alone. Instead, four film shots separated by a known spacing were exposed, and diameters and radii on each film were measured, plotted against film position, and fitted to a linear trend-line. Each cone angle (2θ) was calculated without any need of locating the effective origin, i.e. using the following equation:

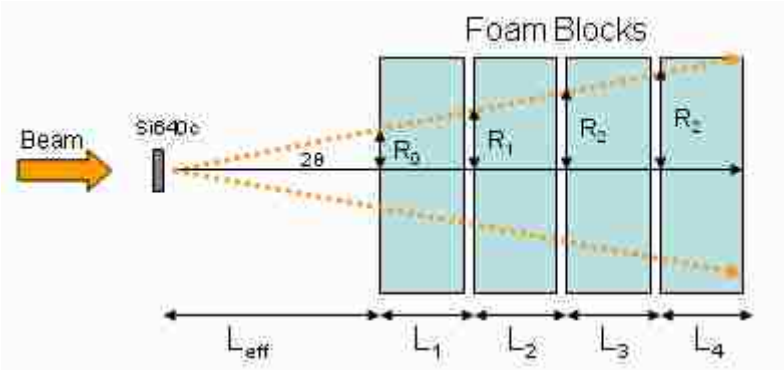

Figure 29: Schematic of powder diffraction experimental apparatus.

$$R_i = (L_{eff} + \sum_{j=1}^{i} L_j) \cdot \tan(2\theta) \qquad (2\text{-}3)$$

A linear fit of ring diameters versus film position yields a slope of tan(2θ) as illustrated in Figure 29 and Equation (2-3). Thus θ can be calculated through:

$$\theta = \frac{1}{2}\tan^{-1}\left(Slope_{radii \cdot vs \cdot filmPosition}\right) \qquad (2\text{-}3)$$

Wavelength and photon energy by extension was determined by inserting this θ value along with the corresponding lattice parameter of the analyzed ring into the Bragg diffraction equation:

$$E = \frac{hc}{\lambda} = \frac{hc}{2d\sin(\theta)} \qquad (2\text{-}4)$$

2.4 Results

2.4.1 Beam Broadening

EBT films were modulated through the beam using the stage programmed described in section 2.3.4 and then digitized on a flatbed scanner with considerations listed in Section 4.3.2. Pixel values were converted to dose using film calibrations described in Section 4.3.3. Beam profiles for each experimental date and are shown in Figure 31 through Figure 35. Dose points were normalized to the dose at the center of the beam and flatness and symmetry were measured over 80% of the field width (Figure 30).

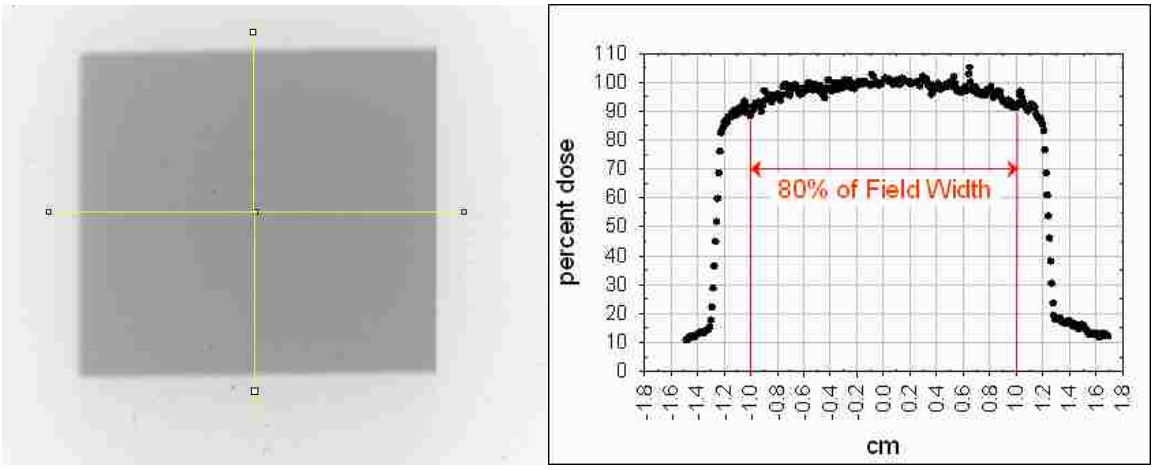

Figure 30: EBT film exposed to a broadened beam with line profile placement (left). Example line profile illustrating the 80% field width within which beam flatness and symmetry were measured (right).

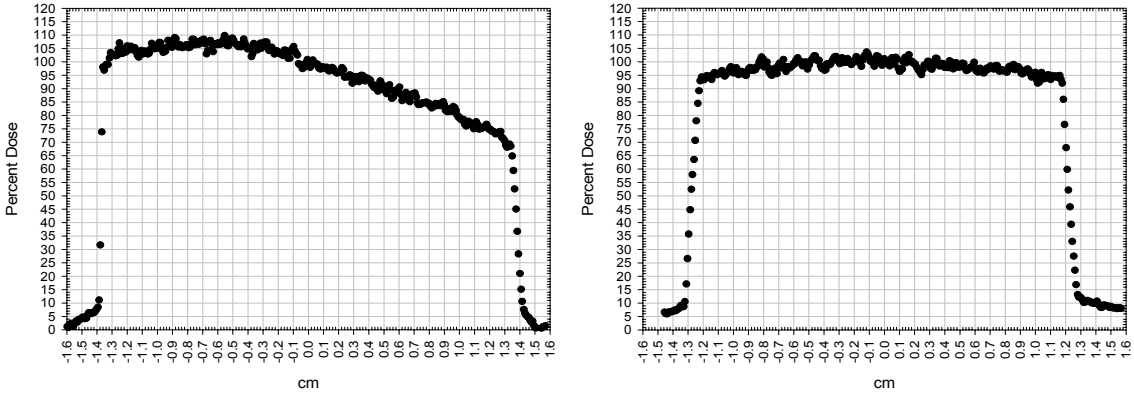

Figure 31: Horizontal (left) and vertical (right) relative dose line profile for December 16, 2006 beam.

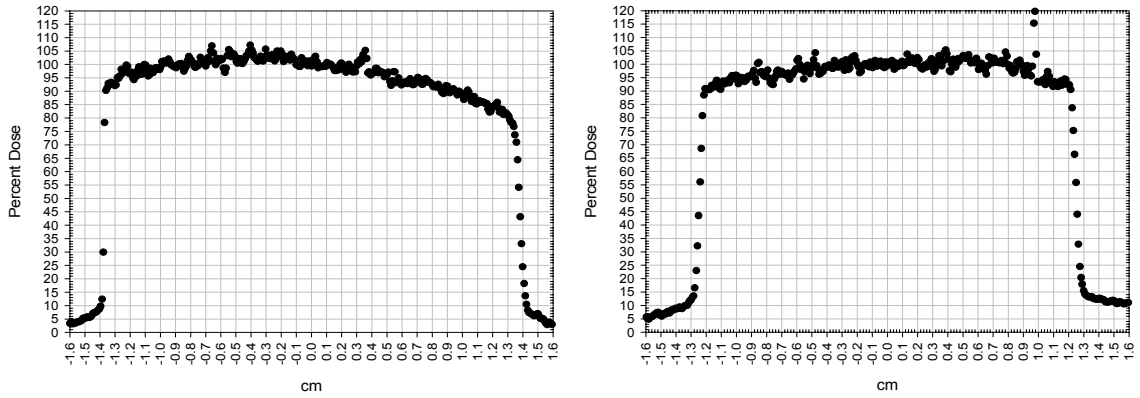

Figure 32: Horizontal (left) and vertical (right) relative dose line profile for March 24, 2007 beam.

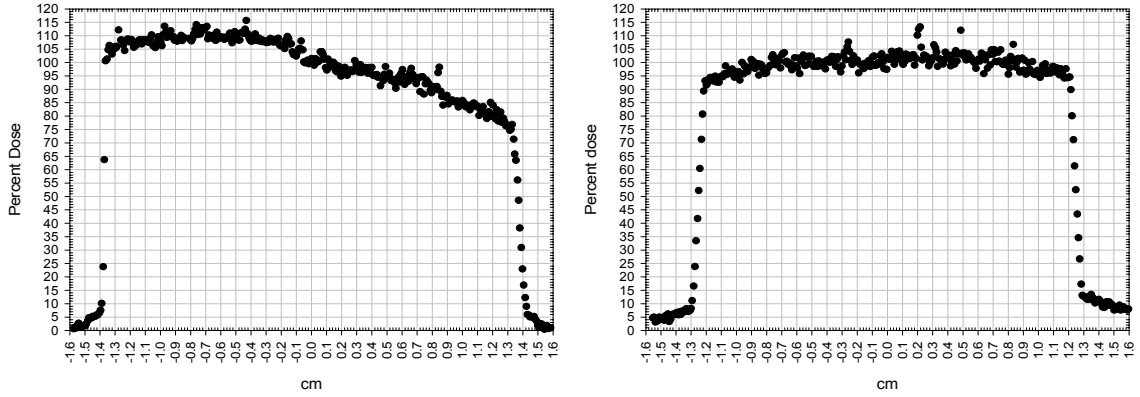

Figure 33: Horizontal (left) and vertical (right) relative dose line profile for April 28, 2007 beam.

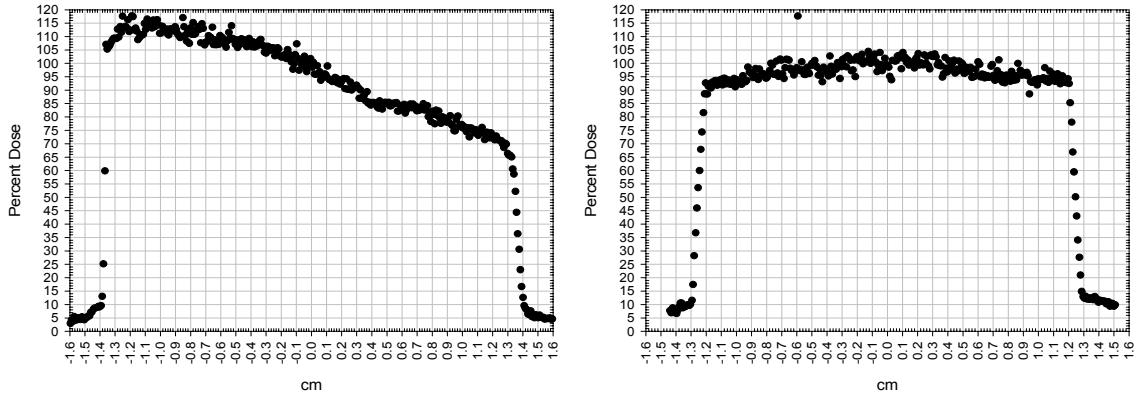

Figure 34: Horizontal (left) and vertical (right) relative dose line profile for May 4, 2007 beam.

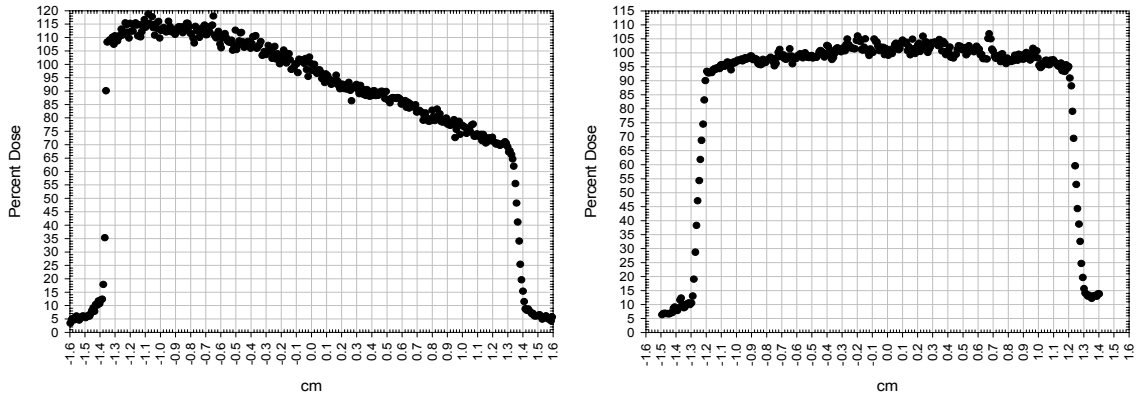

Figure 35: Horizontal (left) and vertical (right) relative dose line profile for May 5, 2007 beam.

As can be seen from the profiles, dose was approximately uniform across the vertical direction of the beam. While some increase in dose was expected on the upper and lower edges of the beam profile from deceleration of the stage when transitioning between upward and downward motion, no such increase was seen. Vertically, dose across 80% of the field varied from 90% to 100% with respect to central-axis, resulting in beam symmetry of 2% and flatness of (-10%, +0%).

The horizontal direction of the beam exhibited a moderate to large variation in intensity from side-to-side, varying with experimental dates. Horizontally, spatial dose distribution, within 80% field width, exhibited on average an asymmetry of 38% with a standard deviation of 18%.

Because of the beam non-uniformity, the exact position of the ion chamber within the beam and the exact portion of beam analyzed in Compton scattering experiments were recorded. For ion chamber depth dose measurements, this was achieved by placing a film downstream from the ion chamber holding slab and exposing it to a broad-beam (Figure 36).

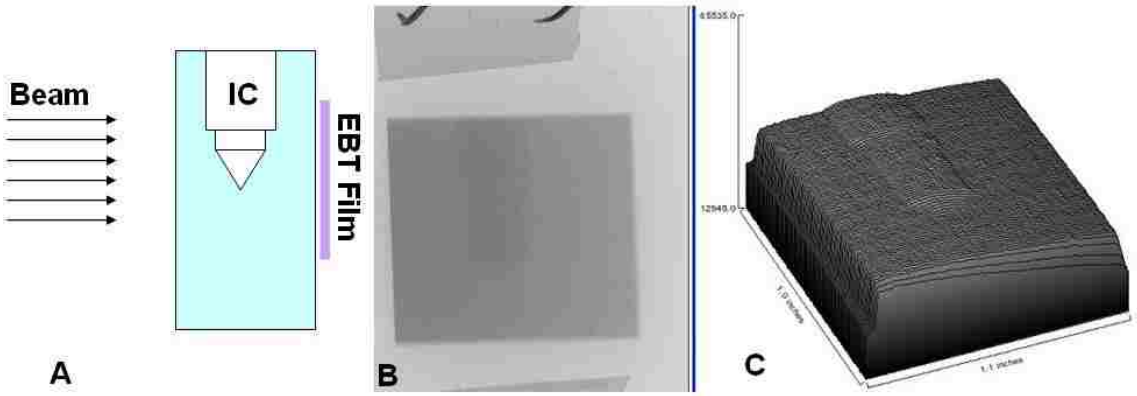

Figure 36: Result of film exposed behind ion chamber block: (A) illustration of setup; (B) sample film exposure; and (C) surface plot of film dose.

The position of the ion chamber within the broad beam can be located on the exposed film. When performing film pixel value-to-dose conversions (Section 4), pixel values were taken over the area of the film that encompassed the active volume of the ion chamber.

2.4.2 Energy Measurements

2.4.2.1 Powder Diffraction

A typical film shot of crystallographic rings is shown in Figure 37. In order to display the diffraction rings more clearly, exposure due to the un-collided beam, normally seen in the center of the rings, has been manually removed. When applying the band pass filter to the image profile, it was found that when digitizing the films at 300 dpi, filtering the image structures smaller than three pixels and greater than 40 pixels was adequate to provide smooth Gaussian peaks with a relatively flat baseline.

A typical result of an energy measurement is shown in Figure 38. The diameters of the rings in the digitized images are plotted versus distance from the center of the Si640c powder sample. The three energy measurements performed per experimental

date, i.e. slopes of three ring profiles, yielded a standard deviation of the mean of 0.1 keV.

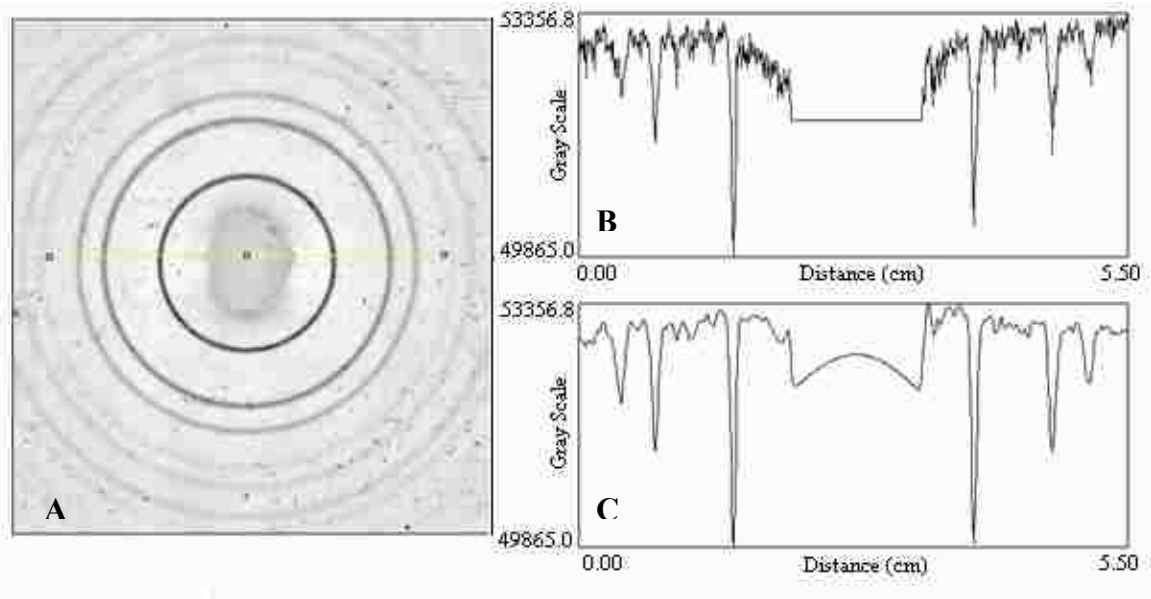

Figure 37: Sample powder diffraction film (A) with line profiles (pixel values vs. position) taken before (B) and after (C) band-pass filtering.

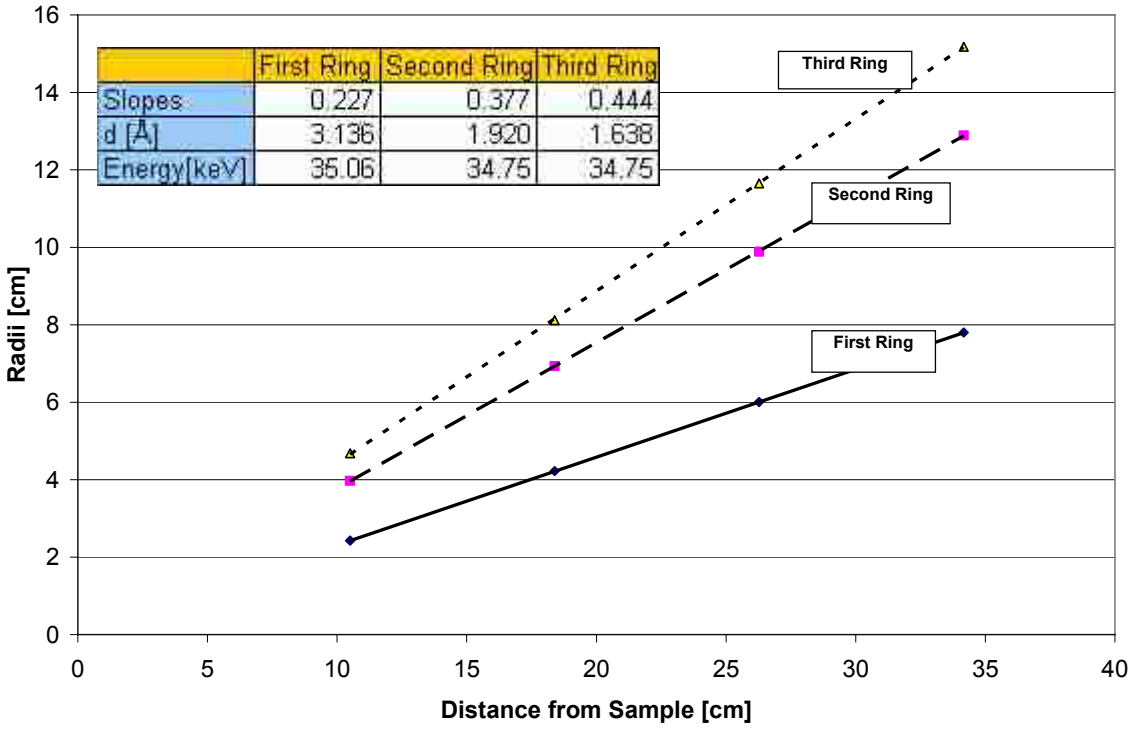

Figure 38: Analysis of powder diffraction performed on March 24, 2007.

2.4.2.2 Energy Measurement Intercomparison

Figure 39 shows the results of the two independent beam energy measurements (i.e. Compton spectroscopy and powder diffraction) along with the monochromator's setting for several acquisition dates. Although the percent dosimetry study described later in this work is focused on 35 keV beams, results at other beam energies are presented for completeness.

Averaged over all dates experimental dates, the powder diffraction measured energies underestimated the monochromator energy settings by 0.1±0.3 keV, and the Compton spectroscopy measured energies overestimated by 0.6±0.3 keV.

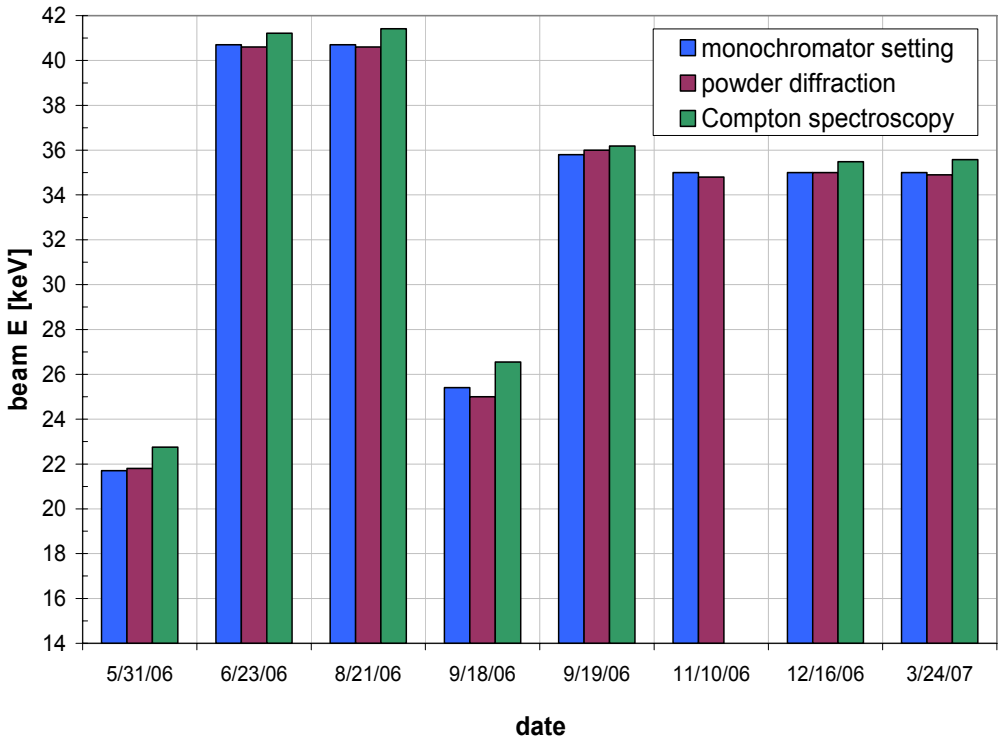

Figure 39: Beam energy measurement results for each experimental date.

2.5 Discussion

2.5.1 Beam Broadening

As mentioned in the results, the broadened beam was not uniform across its vertical direction. Future experiments, which require a uniform dose rate across the entire field, will need to consider adding a horizontal wedge to correct the inhomogeneity.

2.5.2 Energy Measurements

The three energy measurement modalities yielded measurements which agreed to within ±0.5 keV. However, not all modalities have equal practicality. The use of scintillation detectors is not recommended: the calibration is affected by insufficient warm-up time, detector-to-calibration source distance, and total area irradiated by the sources. Additionally, these energy measurements are very time consuming and synchrotron facilities may have long procedures for the admittance of radioactive sources. In contrast, powder diffraction is recommended as both a practical and reliable method for checking the mean beam energy. The resolution of this measurement is limited only by the user's ability to know the exact position of the films and the setup is generally forgiving in terms of systematic errors.

3. Aim 2, Ionization Chamber Depth-Dose Measurements in PMMA

Measure dose to water versus depth in a PMMA phantom using an air-equivalent ion chamber.

3.1 Goal

Planned radiotherapy experiments using cells and small animals on the tomography beamline at CAMD will require accurate dosimetry. Ion chamber dosimetry is the standard method used for calibrating dose and for measuring central axis depth dose for external beam therapy. Because the AAPM TG-61 protocol exists for using ionization chambers to measure dose for x-ray beams in the kilovoltage range (Ma *et al*, 2001) and because ionization chambers generally exhibit low energy dependence, ionization chamber dosimetry techniques have been utilized in the present study.

3.2 Theory of Ionization Chamber Dosimetry

Measured ionization chamber charge at several depths in a PMMA phantom, resulting from exposures to the monochromatic tomography beamline, can be converted to dose using AAPM's TG-61 dosimetry protocol for low-energy, polychromatic x-ray beams.

3.3 Materials and Methods

3.3.1 Conversion of Charge to Dose

Ionization chamber charge readings were converted to dose using the AAPM TG-61 protocol for 40-300 kV x-ray beam dosimetry (Ma *et al*, 2001). TG-61 gives recommendations for two beam energy ranges: 1) low-energy x-rays (40 kVp – 100 kVp) and 2) medium-energy x-rays (100 kVp – 300 kVp). The equivalent energy of a 100-kVp beam is approximately 33 keV which is slightly less than 35 keV, hence the

100 kVp – 300 kVp formalism for medium-energy x-rays (effective energy 33 keV – 100 keV) was followed.

For 100-300 kVp x-rays, the TG-61 protocol recommends that dose be measured at a 2-cm depth using an ionization chamber calibrated free in air in terms of air kerma at a radiation quality close to that being used for in phantom measurements (Ma *et al*, 2001).

Assuming these conditions, dose to water is given by:

$$D_w = Q_{corr} N_k P_{Q,cham} P_{sheath} \left(\overline{\mu}_{en} / \rho\right)_{air}^{w}, \qquad (3\text{-}1)$$

where:

Q_{corr} is the charge reading corrected for ambient conditions (22° C, 760 mm Hg),

$$Q_{corr} = M_{Raw} P_{pol} P_{ion} P_{TP}, \qquad (3\text{-}2)$$

where:

M_{raw} is the uncorrected raw charge reading collected by the electrometer,

P_{TP} is the temperature and pressure correction factor which corrects charge reading to 101.33 kPa and 273.2 K. with the formula:

$$P_{TP} = \frac{273.2 + T[^oC]}{295.2} \cdot \frac{101.33}{P[kPa]}, \qquad (3\text{-}3)$$

P_{pol} is the polarity correction factor and was computed by:

$$P_{pol} = \left| \frac{M_{raw}^{+} - M_{Raw}^{-}}{2M_{raw}} \right|, \qquad (3\text{-}4)$$

where:

M_{raw}^{+} and M_{raw}^{-} are uncorrected readings taken at positive and negative voltages respectively;

P_{ion} is the recombination factor and was computed by:

$$P_{ion} = \frac{1-\left(\frac{V_H}{V_L}\right)^2}{\frac{M_{Raw}^H}{M_{Raw}^L}-\left(\frac{V_H}{V_L}\right)^2}, \qquad (3\text{-}5)$$

where:

V_H and V_L are the voltages corresponding to the M_{raw}^+ M_{raw}^- measurements respectively.

Ion chamber recombination should be near unity due to the low dose rate and the DC nature of the beam and polarity effect should also be small. P_{ion} and P_{pol} were difficult to measure due beam fluctuations, particularly to the continuous decrease in synchrotron beam current over a course of readings necessary for their determinations. Our data indicated these factors were less than 0.5%. Therefore, P_{ion} and P_{pol} were assumed unity in the present study.

N_k is the air kerma calibration factor obtained from an accredited dosimetry calibration laboratory (ADCL). Values of 1.215 Gy·C^{-1} and 1.219 Gy·C^{-1} were obtained from 120 kVp x-ray (HVL=7.0 mm Al) and 80 kVp x-ray (HVL=2.96 mm Al) beam calibrations. Interpolating using Al half-value layers, a value of 1.219 Gy·C^{-1} for the 35 keV beam (HVL=3.33 mm Al, determined from NIST tables by Hubbell and Seltzer 1996) was obtained.

$P_{Q,cham}$ is the overall chamber correction factor, which accounts for the change in ion chamber response due to displacement of water by the chamber, presence of the stem, etc. Assuming that it was appropriate to use (1) $P_{Q,cham}$ = 0.995 for the similar NE2611/NE2561 chambers and for a 0.1 mm Cu HVL beam in TG-61 Table VIII and (2)

a field size correction factor of 1.005 by extrapolating data in TG-61's Figure 4 from 20 cm^2 to our approximately 7-cm^2 field size, $P_{Q,cham} = 1.00$.

P_{sheath} is the sleeve correction factor, and its value was taken to be 1.000 as measurements in this study were not performed with a build-up cap.

$\left(\mu_{en} / \rho\right)_{air}^{water}$ is the ratio of mass energy absorption coefficients of water to air. The value was taken as 1.015, calculated from interpolated mass energy absorption coefficient values of water and air from NIST tables for 35-keV (Hubbell *et al*).

While the TG-61 formula (Equation 3-1) is meant to be used at a depth of 2 cm in water, the same formula and factors were used to convert charge to dose for charge measured at all PMMA depths.

3.3.2 Air Ionization Charge Measurement

A 0.23-cm^3 Scanditronix-Wellhöfer model FC23-C cylindrical, air-equivalent ionization chamber (Scanditronix Wellhöfer GmbH, Schwarzenbruck, Germany), operating at -300 V, was used when collecting charge. Ion chamber leakage was ~10^{-15} A, approximately four orders of magnitude less than measurement currents. Ionization charge was measured using a calibrated, modified Keithley 614 electrometer (Keithley Instruments Inc., Cleveland, OH, USA).

3.3.3 The Homogenous Phantom

X-rays were incident on a polymethylmethacrylate (PMMA) slab phantom, consisting of stacked ¼″ and ½″ thick slabs and 10×10-cm^2 faces, oriented with beam's central axis normal to slab faces. The phantom accommodated either 5×5-cm^2 films or an ion chamber. For film exposures, one film was placed between slab faces per exposure. For ionization chamber measurements, a ½″ slab had an opening drilled that allowed insertion of a 0.23-cm^3 cylindrical ion chamber. For all beamline exposures involving

EBT film and ion chamber dosimetry, the phantom was placed on the movable stage to create a broad beam.

3.3.4 Ionization Chamber Readings

The ionization chamber was irradiated for an approximately 10 minute beam exposure upon initial use and immediately after voltage change to allow it to reach equilibrium, i.e. proper warm-up. Charge measurements, subsequently converted to dose, were preformed at several depths ranging from 0.58 cm to 9 cm, with the center of the chamber taken to be the effective point of measurement. Readings were typically acquired for 320 seconds (8, 40-s periods of scanning the phantom through the beam). Charge readings were linearly scaled to100-mA from the average beam current during exposure.

3.4 Results

3.4.1 Depth Dose Comparison

Depth-dose data for five independent measurement sessions are plotted in Figure 40. At 2-cm depth, determined from the dose of the two data points bracketing 2-cm using non-linear interpolation, ionization chamber doses ranged from 81.15 cGy to 101.83 cGy having a mean (± σ) of 88.4 ± 9.9 Gy (Table 3). The variation of these depth dose curves show that the dose per 100 mA of beam current, and hence, the incidence fluence rate per 100 mA beam current, is not consistent among experimental runs. The shape of the depth-dose curves for each of the five measurement sessions were compared by normalizing each curve to 100% at the 2 cm depth, and results are shown in Figure 41.

For depths greater than 1.5 cm, fractional depth-dose data from the 5 measurement sets agreed well with each other and the MCNP5 calculation. The maximum measured percent dose difference between any two data points at a common depth was 2.8% at a depth of 8.2 cm, and the average difference (± σ) between any 2 data sets was 1.5 ± 1.1%

(N=16). At depths of less than 1.5 cm, there were some points with fractional dose by as much as 3.0% greater than that of the MCNP5 curve.

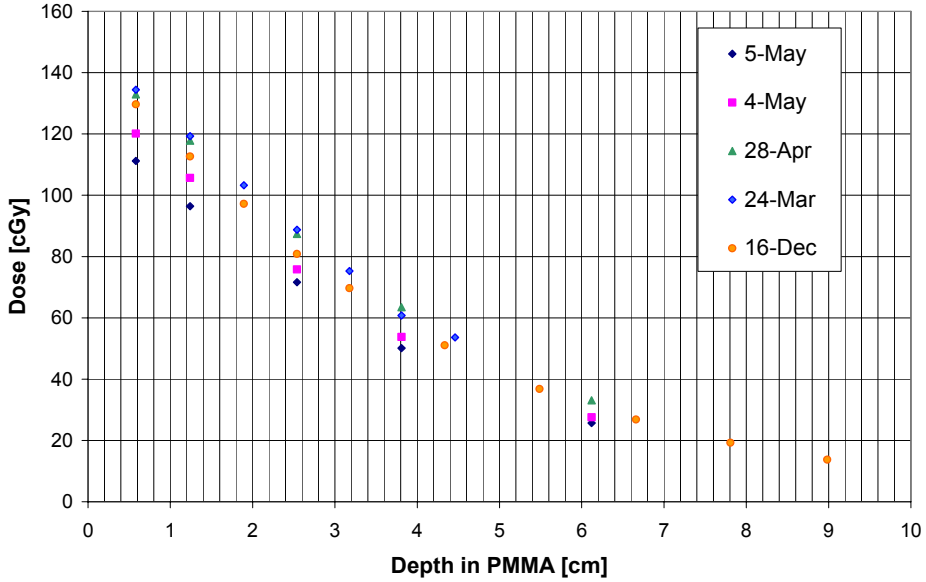

Figure 40: Comparison of ion chamber depth doses.

Table 3: Interpolated dose to water values obtained on separate dates at a depth of 2 cm in PMMA. Mean = 92.8 cGy; Standard deviation = 8.5 cGy.

Date	Depth 2[cm]
16-Dec	93.57
24-Mar	101.83
18-Apr	99.69
4-May	87.60
5-May	81.15

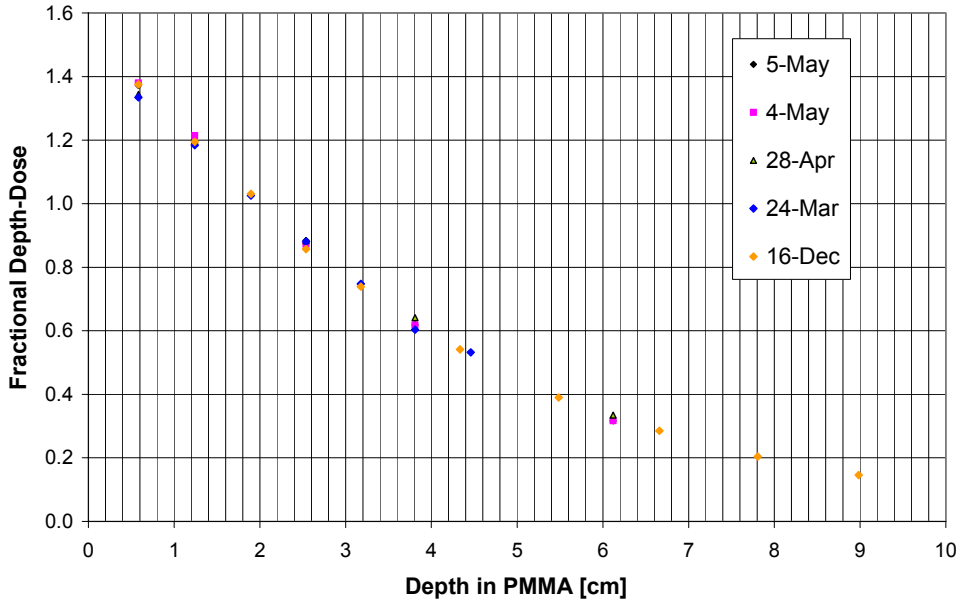

Figure 41: Fractional ionization chamber depth doses normalized at 2-cm depth.

3.5 Discussion

Ion chamber measured depth dose curves performed on different experimental dates showed that the beam's fluence rate per 100 mA beam current can change significantly between experimental dates. Hence, future experiments that will need to deliver known dose will require the use of a transmission ion beam monitor.

The good agreement attained between fractional depth dose curves taken on different experimental dates suggests that there was not a strong depth dependence of the conversion from charge to dose. This should be confirmed by future MCNP5 calculations that compare dose per fluence without an ion chamber to ionization per fluence with an ion chamber versus depth in PMMA.

4. Aim 3, Film Depth-Dose Measurements in PMMA

Measure dose to water versus depth in a PMMA phantom using EBT film.

4.1 Goal

To develop radiochromic Gafchromic EBT film dosimetry methods for use on CAMD's tomography beamline, to measure central-axis depth dose in PMMA using those methods, and to compare absolute and fractional depth-dose measurements with those obtained from ionization chamber measurements.

4.2 Theory of Radiochromic Film Dosimetry

Gafchromic EBT film was chosen for use as a second dosimeter because of its reported low energy dependence of its sensitivity (response/dose), high spatial resolution, and inherent ease in irradiation and analyzes. Unlike conventional radiographic film, which is sensitive to room light and must be exposed in a light tight envelope and developed in a dark room, radiochromic film can be exposed to ambient light for short periods of time with no appreciable effects, can be cut into any desired size, and is self developing getting progressively bluer with absorbed dose.

From results of Chiu-Tsao *et al* (2005) and the film manufacturer's "white paper" (ISP 2005) (see Section 1.3), it was anticipated that EBT film calibrations performed on a clinical 6 MV linac might be sufficient for establishing a dose-to-net optical density (NOD) curve for use with the kilovoltage synchrotron-generated beam. However, conflicting results of Butson *et al* (2006) (see section 1.3) prompted additional calibrations to be performed with keV range x-ray sources to test the film's energy dependence when using the digitization process specific to this research. These calibrations were performed using ^{125}I brachytherapy seeds (effective energy ≈ 30 keV) and orthovoltage x-ray beams (125 kVp and 75 kVp).

4.3 Materials and Methods

4.3.1 Film Preparation and Handling

EBT films sheets (8″×10″) were cut into 5×5-cm^2 squares with a small line drawn on along the edge and parallel to the long axis of the film sheet. This was done to ensure consistent film orientation on the flatbed scanner which will be further discussed in section 4.3.2.

Following recommendations from the Gafchromic White Paper (ISP, 2005), which states that while EBT film is relatively light insensitive, exposure to any light source should be avoided when possible, all films were stored in a light tight envelope before and after irradiation. Films were also stored in a refrigerator at approximately 40ºF when not is use following the white paper's recommendation that film storage is best practiced with temperatures cooler than room temperature (2005).

4.3.2 Film Scanning

Exposed films were digitized at least 24 hours after exposure using an Epson 1680 Professional flatbed scanner equipped with a transparent unit. Because EBT film becomes increasingly bluer with increasing dose and, therefore, has a maximum sensitivity to red light (ISP, 2005), only data from the scanner's red channel was stored as a 16-bit grayscale TIF image.

Typically, optical density of radiochromic film continues to increase during post-exposure with density growth proportional to the logarithm of time after exposure. However, post-exposure growth is reported in the Gafchromic EBT white paper to be substantially less than previous models of Gafchromic films (ISP, 2005) (Figure 42).

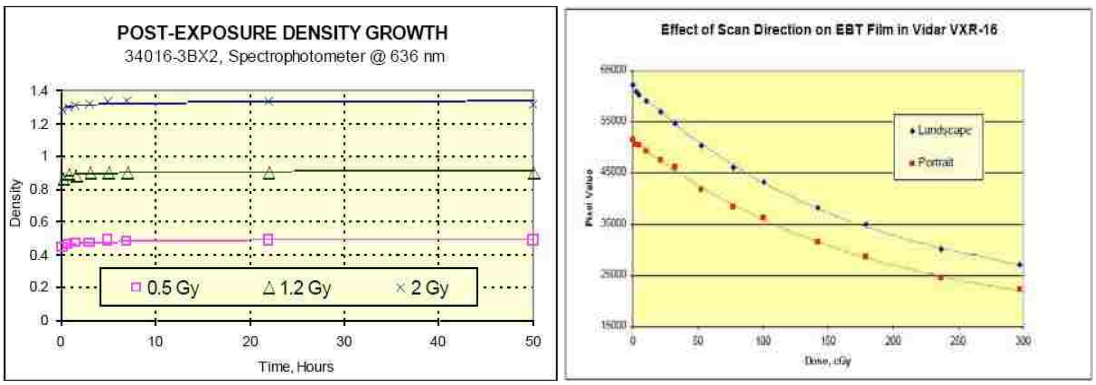

Figure 42: (Left) graph showing Gafchromic EBT post-exposure effects (ISP, 2005); (Right) graph showing film-scanner orientation effects (ISP, 2005).

It is also well documented that due to molecular polarization, the film's orientation relative to motion of the scanner's light source greatly affects pixel values. Reports have shown that pixel values can vary as much as 20% depending on the orientation in which it is placed on a flatbed scanner (ISP, 2005) (Figure 42). To account for this, a small line was drawn on all cut film pieces parallel to the long axis of the original uncut film sheet. This line was used to ensure that all films were scanned in the same orientation as the calibration films. In this research all films were placed with the long axis parallel to the long axis of the scanner (i.e. the portrait orientation).

It has been shown that the Epson 1680 flatbed scanner dose not produce a completely uniform scan across the entire scanning field. The results of experiments with L. Pealink *et al* (2007), report a difference of almost 8% measurement difference between films scanned on the sides of the scanner compared to those taken from the center. To ensure that that each film was positioned in the same spot on the center of the scanning face, a special cardboard sheet was constructed and placed on the scanning bed and all film squares were placed on a square cut-out located at the sheet's center.

Results of experiments performed by Pealink *et al* (2007) also showed that differences in pixel values up to 2.3% can be observed for an initial scan and subsequent scan which they attribute to drift in scanner light intensity (2007). Therefore,

immediately before digitization, the scanner was warmed by initiating five successive blank scans.

To compare results of calibration performed for this study with other published EBT film data, pixel values were converted to net optical density (NOD). The conversion to optical density was established by using a film step template containing a series of grey scales with corresponding optical density values (Figure 43). The step wedge was digitized and mean pixel values for each "step" were acquired through ImageJ and plotted against their corresponding optical densities. Plots were fit to fifth-order polynomials, the equations of which were used to convert pixel value to optical density for all subsequent film measurements. Net optical density was calculated by subtracting the optical density of an unirradiated film.

Figure 43: Kodak optical density photographic template used to transform Epson 1680 red-channel pixel values to optical density.

4.3.3 Film Calibration

Calibration curves of pixel values or net optical density versus dose to water were measured using four radiation sources: (1) 6 MV x-rays; (2) ^{125}I prostate brachytherapy seeds (ProstaSeed, model 125SL) (Figure 44); (3) 75-kVp and (4) 125-kVp x-rays.

4.3.3.1 6 MV Calibration Geometry

The 6 MV calibration was performed in a SolidWater™ phantom using a 6-10 Varian Clinac EX at Mary Bird Perkins Caner Center. Known doses were delivered to 2×2-cm^2 films placed at the standard calibration arrangement: 10×10-cm^2 field size, 100-cm source-to-surface-distance (SSD), and depth of 1.5-cm within the phantom. Under these setup conditions, one monitor unit corresponds to 1 cGy of dose to water at the film's center. Twenty such exposures were taken with doses ranging from 10 to 400 cGy.

4.3.3.2 ^{125}I Calibration Geometry

A calibration was performed with a 1×10-cm^2 strip of film using six calibrated ^{125}I brachytherapy seeds (ProstaSeed model 125SL). A picture of the cross section of the seed model used is shown in Figure 44. Each seed was placed into a separate, tight fitting hole drilled into a PMMA phantom. The phantom consisted of two 1×9×4.5-cm^3 blocks (labeled 'B' in Figure 45) each with three holes spaced 0.25 cm from each other and 1.0 cm from the block's edge. During calibration a strip of film was placed between two PMMA such that each seed was at a 1-cm distance. A metal clamp was placed around the blocks containing the seeds to minimize movement during of exposure. Additionally 4×9×9-cm^3 blocks of PMMA (labeled 'A' in Figure 45) were placed above and below the film to allow approximately full dose to film from scatter. Figure 46 shows the actual phantom when fully assembled. Upon commencing the film exposure, aluminum foil was wrapped around the entire apparatus to ensure that the film was not darkened by any outside light source.

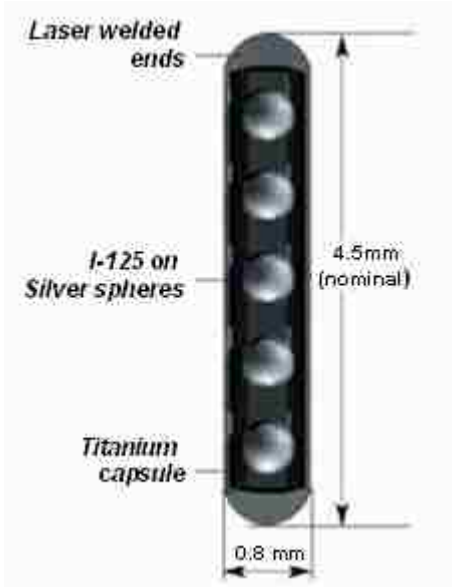

Figure 44: Schematic of ProstaSeed model 125SL.

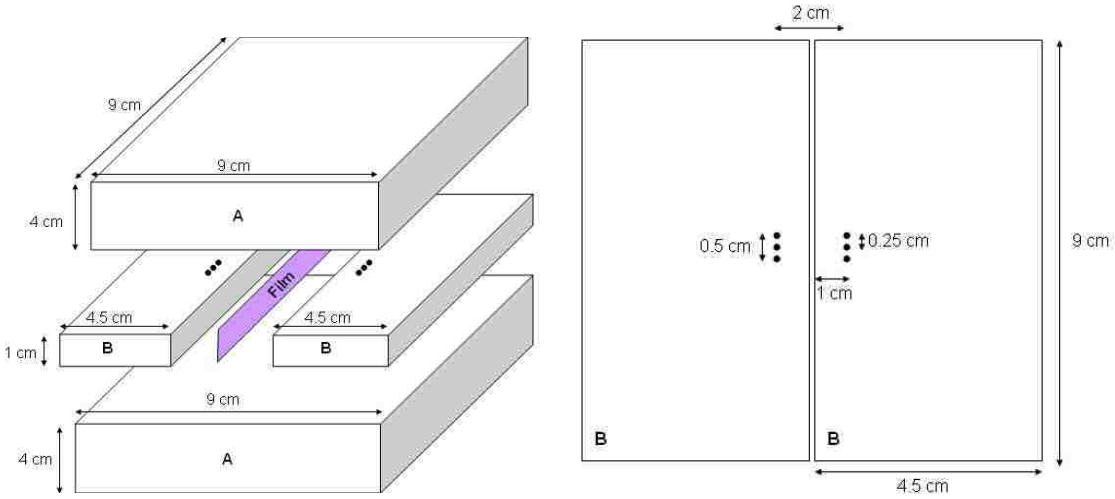

Figure 45: (left) schematic of ^{125}I calibration phantom geometry; (right) bird's eye view of blocks labeled 'B' in schematic showing film and brachytherapy seed positioning.

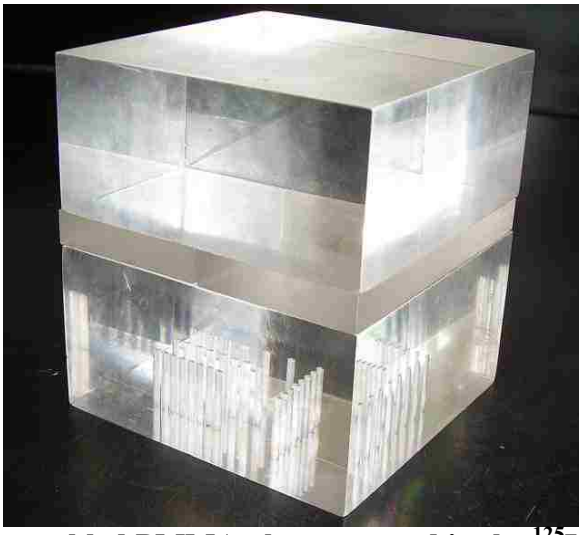

Figure 46: Photo of assembled PMMA phantom used in the ^{125}I calibration.

The dose contribution from a single seed was calculated using the AAPM TG-43 protocol:

$$\dot{D}_{water}(r,\theta) = S_k \cdot \Lambda \cdot \frac{G_L(r,\theta)}{G_L(r_o,\theta_0)} \cdot g_l(r) \cdot F(r,\theta), \qquad (4\text{-}1)$$

where:

S_k is the air kerma strength factor (U, U=cGy·hr^{-1}),

Λ is the dose rate constant (cGy·hr^{-1}·U^{-1}),

$G_L(r,\theta)/G_L(r_o,\theta_o)$, is the geometry correction factor,

$g_l(r)$ is the radial dose function,

$F(r,\theta)$ is the anisotropy factor (Rivard *et al*, 2004).

The air kerma strength factor, S_k, was obtained for each seed by acquiring the average charge collected in an IVB unsealed well-chamber (model HO11764) (pC), dividing by time of acquisition (min), and multiplying by the well chamber's current-to source strength factor (U/pC/min). The dose rate constant, Λ, values were taken from a report by Heintz *et al* (2001) (Λ = 0.950 cGy·hr^{-1}·U^{-1}). The geometry factor, $G_L(r,\theta)/G_L(r_o,\theta_o)$, was taken to be the inverse of the square of the seed distance

from each point on the film; seeds were placed at an appreciable distance from the film for this approximation to be appropriate, i.e. (r >> L Figure 47). The radial dose function, $g_L(r)$, was also obtained from values listed by Heintz *et al* (2001) (see Table 4). The anisotropy factors, $F(r,\theta)$ were taken as unity as film positions corresponding to the seed's transverse plane ($\theta = \pi/2$ in Figure 47) for which pixel values were taken is defined as such in the TG-43 formalism (Rivard *et al*, 2004).

Table 4: Coefficients for a fifth-order polynomial as a function of distance in water, r (cm), describing the radial dose function $g_l(r)$ (from Heintz *et al*, 2001).

$$g_l(r) = \sum_{i=0}^{5} A_i r^i$$

A0	1.2537
A1	-0.23884
A2	-0.02701
A3	0.013639
A4	-0.001531

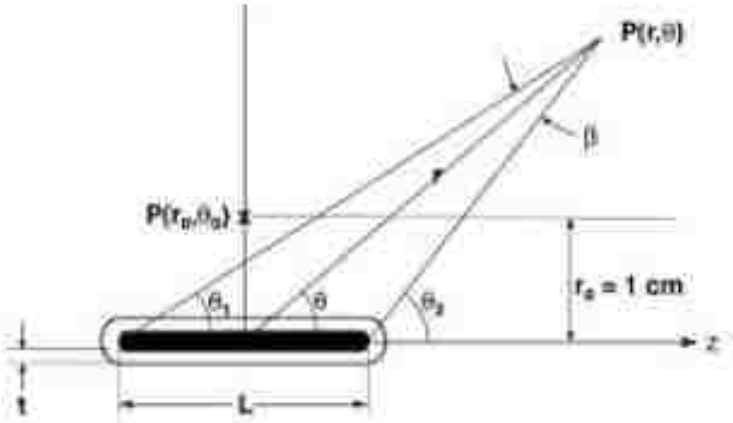

Figure 47: Illustration of seed coordinate system.

Equation (4-1) specifies the dose distributions in water, yet film irradiations in this study took place within PMMA. Therefore an additional correction was made by multiplying the ratio of ^{125}I dose-to-water in water to dose-to-water in PMMA as a function of distance from radiation source point in PMMA (Figure 48). This function was obtained by fitting the results of Luxton *et al* (1994) to a second order polynomial named $L(r)$ (Figure 49).

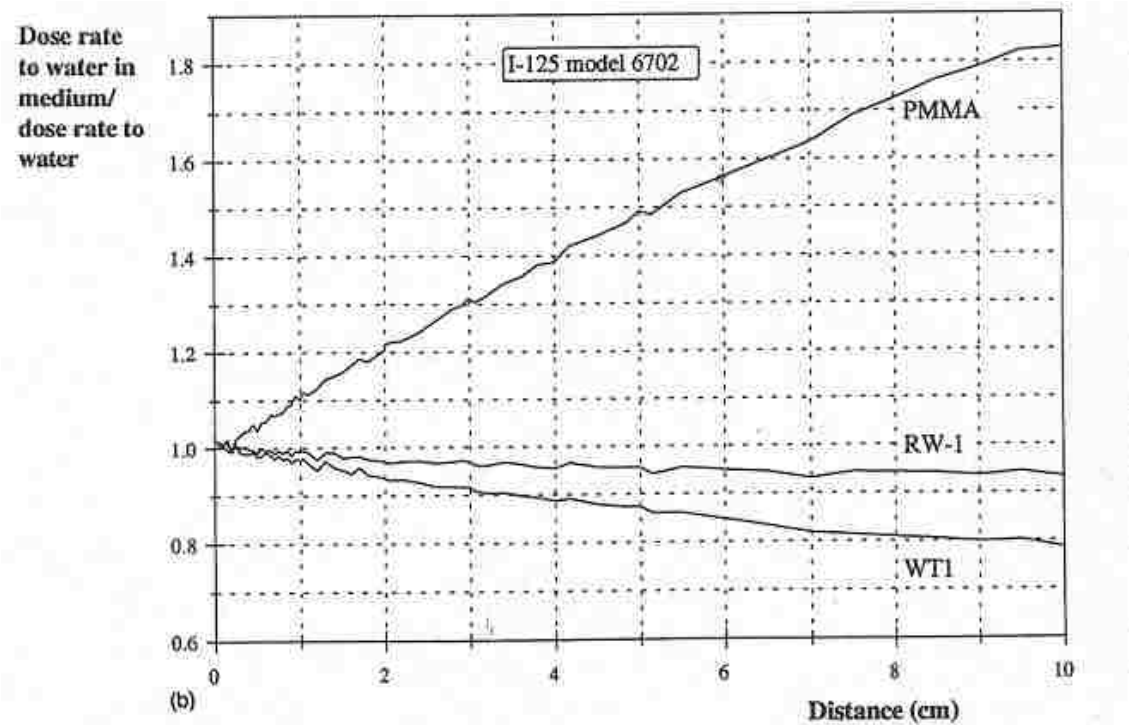

Figure 48: Reported data from Luxton *et al* (1994) showing ratio of dose to water in PMMA to dose-to-water in water as a function of distance in PMMA.

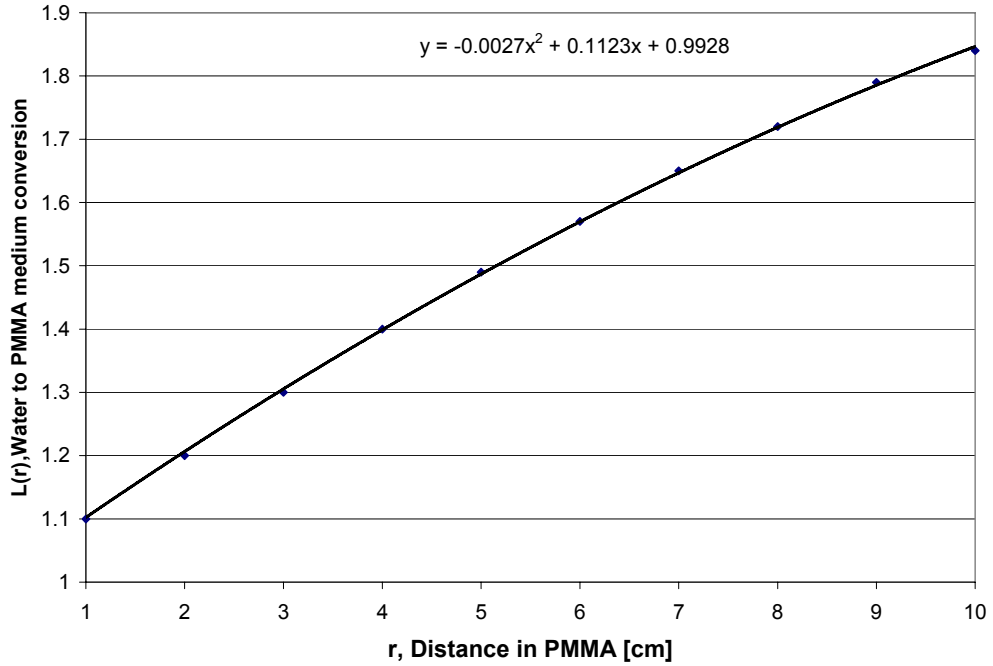

Figure 49: Data from Luxton *et al* (1994) fit to second-order polynomial.

Although Luxton's work did not include the specific seed model used in this research, its use was considered appropriate since previous dose calculations showed that

with the film-to-seed distance used in this study, the source geometry played a negligible role in total absorbed dose.

Because seed strengths were decaying over the time of exposure (^{125}I $T_{½}$ = 60.1 days), the TG-43 equation for was multiplied by the integral of the radioactive decay equation such that:

$$D_{Water}(\vec{r}) = \dot{D}_{water}(\vec{r}) \cdot \int_0^T e^{-\frac{\ln 2}{T_{1/2}}t}\, dt = \dot{D}_{water}(\vec{r}) \cdot \frac{T_{1/2}}{\ln 2}\left[e^{-\frac{\ln 2}{T_{1/2}}T} - 1 \right], \quad (4\text{-}2)$$

where:

$\dot{D}_{water}(\vec{r})$ is the dose rate at location $\vec{r}$ at the start of exposure, and

T is the total irradiation time (days) typically on the order of two weeks.

Pixel values were measured along a horizontal line profile (Figure 50). The vertical position of the line profile was correlated to the position calculated (i.e. the position giving an anisotropy factor of unity) by positioning the line profile a distance equivalent to one half of a seeds axial length from the bottom of the film.

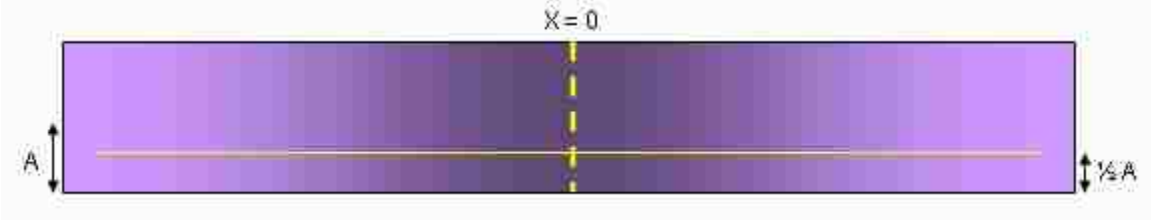

Figure 50: Illustration of film irradiated by brachytherapy seeds (length A) in PMMA phantom. Pixel values were taken across a line-profile located half the seeds length from the bottom corresponding to an anisotropy factor defined as unity in TG-43 formalism.

The resulting dose contribution from a single seed, combining equations (4-1) and (4-2), is given by:

$$D(r,\theta) = S_k \cdot \Lambda \cdot \frac{1}{r^2} \cdot g_L(r) \cdot L(r) \cdot \frac{T_{1/2}}{\ln 2}\left[e^{\frac{\ln 2}{T_{1/2}}t} - 1 \right] \qquad (4\text{-}3)$$

where *L(r)* represents the Luxton correction factor as function of seed-to-pixel distance. The value r was calculated as:

$$r = \sqrt{(x + x_0)^2 + 1} \qquad (4\text{-}4)$$

where:

x is the position on the line profile,

x_o is the horizontal position of a seed relative to x = 0.

x=0 was defined as the position of the on the film which was on the same horizontal position as the seeds placed between the three rows on either side of the film (Figure 50). This position was determined on the film as the point of maximum deposited dose, i.e. the point with the lowest pixel value. Each seed was assigned a value for x_o of -0.25, 0, or 0.25 cm depending on the order in the two rows of slots (Figure 51).

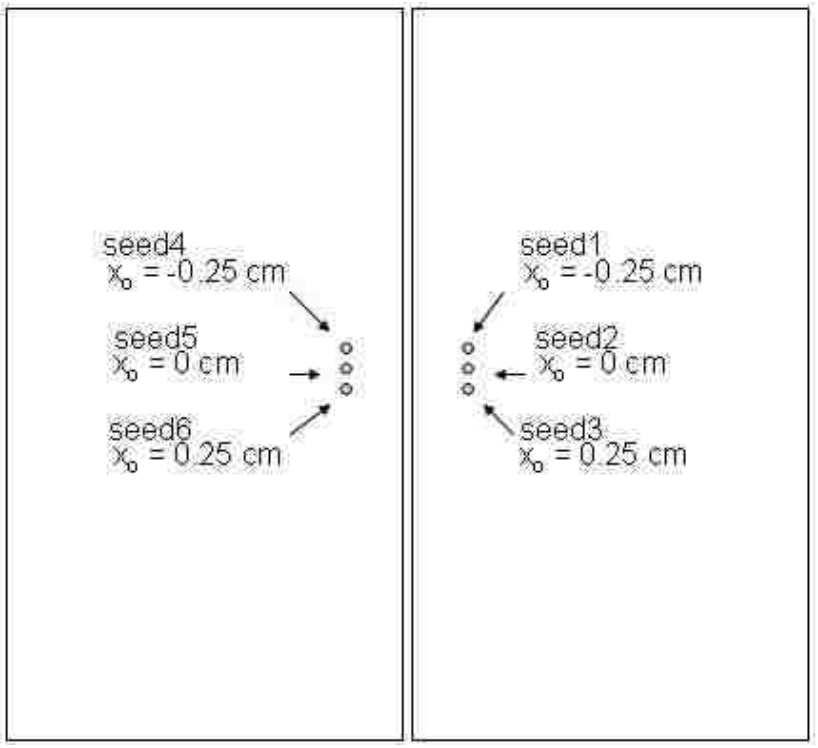

Figure 51: Seed assignment of x_o.

Table 5: Seed strengths and exposure times for five ^{125}I film calibrations.

	Source Strengths (cGy/hr)						
Date	Seed1	Seed2	Seed3	Seed4	Seed5	Seed6	Exposure (hr)
8/11/2006	0.410	0.395	0.400	0.386	0.400	0.401	360
11/14/2006	0.370	0.372	0.388	0.368	0.359	0.379	143.8
11/20/2006	0.341	0.344	0.358	0.339	0.331	0.349	221
1/19/2007	0.410	0.411	0.401	0.421	0.426	0.412	84
1/24/2007	0.389	0.391	0.381	0.400	0.405	0.391	174.5

4.3.3.3 Orthovoltage Calibration Geometries

Film calibrations were also performed using orthovoltage x-rays to irradiate separate films placed on the surface of a block of Solid Water™. X-rays were generated by a Philips Orthovoltage RT-250 at The University of Texas MD Anderson Cancer Center at Houston with assistance from Naresh Tolani, MS. Beams of 75 kVp (HVL 1.86 mm Al) and 125 kVp (HVL 2.9 mm Al) were used (Figure 52). Films, consisting of 5×5-cm^2 squares with orientation marked on the sides, were placed at the machines standard calibration setup: 50-cm SSD for a field size of 10×10-cm^2 at the surface of a Solid Water™ phantom.

Figure 52: Left) Philips Orthovoltage RT-250 treatment head Right) phantom setup (Courtesy of MD Anderson Cancer Center).

Dose was calculated as the Given Dose Rate (GDR – the dose which occurs on the skin during a patient trial) was the product of time of exposure, Air Dose Rate (ADR), and backscatter factor (BSF). BSF and ADR values, provided in the MD Anderson

machine data manual (Table 6), were checked against direct measurements taken just prior to film calibration. The Air Dose Rate was measured using a 0.23-cm^3 Scanditronix-Wellhöfer air equivalent ionization chamber (section 3.3.3) in air at a 50-cm source-to-chamber distance (SCD) and 10×10-cm^2 field size. The BSF was measured by the ratio of dose (using 6 MV calibration) from films irradiated in air to films irradiated on the surface of Solid Water™. Results agreed well with MD Anderson tables, and values from the MD Anderson tables were used to compute dose to film.

Table 6: Air dose rate (ADR), back scatter factor (BSF), and given dose for a Philips RT-250 orthovoltage unit when set to a 10×10-cm2 field size and 50 SCD on the surface of water (GDR).

	ADR [cGy/min]	BSF	GDR [cGy/min]
75 kVp	26.0	1.25	32.5
125 kVp	58.7	1.28	75.1

4.3.4 Film Dosimetry

When performing depth-dose measurements on the tomography beamline, 5×5-cm^2 films squares were placed either on the PMMA phantom's surface or between slabs (section 3.3.4). After exposure, at least 24 hours were allowed to elapse before digitization with a flat-bed scanner (section 4.3.2).

The 125-kVp calibration was used for subsequent conversion of film pixel value to dose as that beam's half value layer (HVL 2.9 mm Al) was closest to that of the 35-keV (HVL 3.3 mm Al) CAMD x-rays. A fifth order polynomial was fit through pixel values vs. Dose resulting form the 125-kVp calibration and the equation was used to convert all film depth-dose exposures to an absorbed dose.

4.4 Results

4.4.1 Film Calibration

4.4.1.1 6 MV Calibration

The 6 MV film calibration results are displayed in Figure 53. A calibration performed in an almost identical fashion (i.e. same model scanner, acquisition program, and program settings) by Dave Lewis of ISP Corp. is provided for comparison. The two independent calibrations agree well with each other.

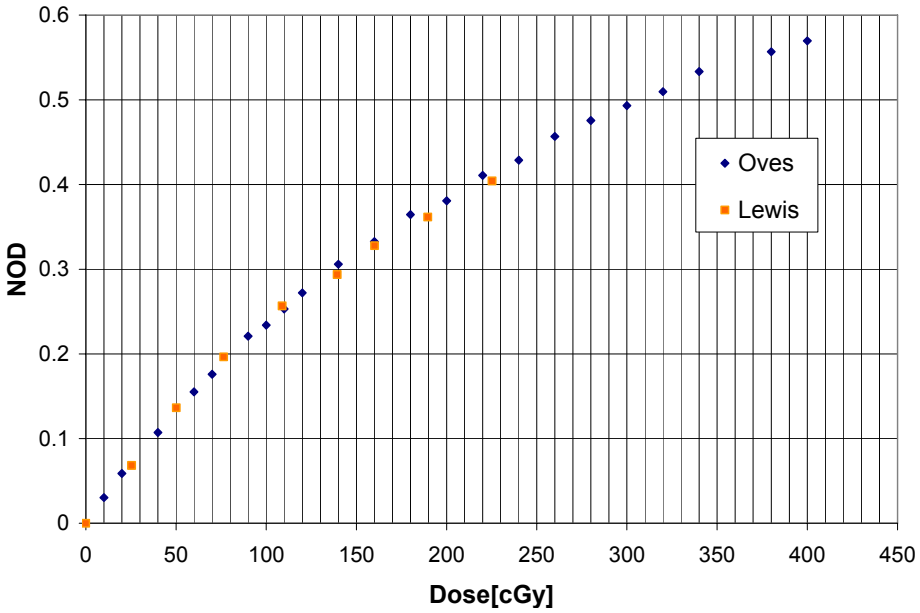

Figure 53: Comparison of 6 MV film calibration performed for this research (Oves) with that by Dave Lewis, ISP Corp. (Lewis, private communication 2007).

4.4.1.2 ^{125}I Calibration

Figure 54 shows a grayscale image for a ^{125}I calibration exposure. Figure 55 shows dose versus position on the line profile. Figure 56 shows net optical density versus position on the line profile. Figure 57 shows data from the previous two graphs combined to create a NOD vs. Dose calibration curve. Averaging data from this and four other measurements, the curve of Figure 58 was obtained and yielded a standard deviation (N=5) of 5%. Note that the ^{125}I curve gives a lower dose for the same pixel value as compared to the 6MV calibration curve (Figure 58).

Figure 54: Grayscale image of film strip exposed for 15 days in seed phantom.

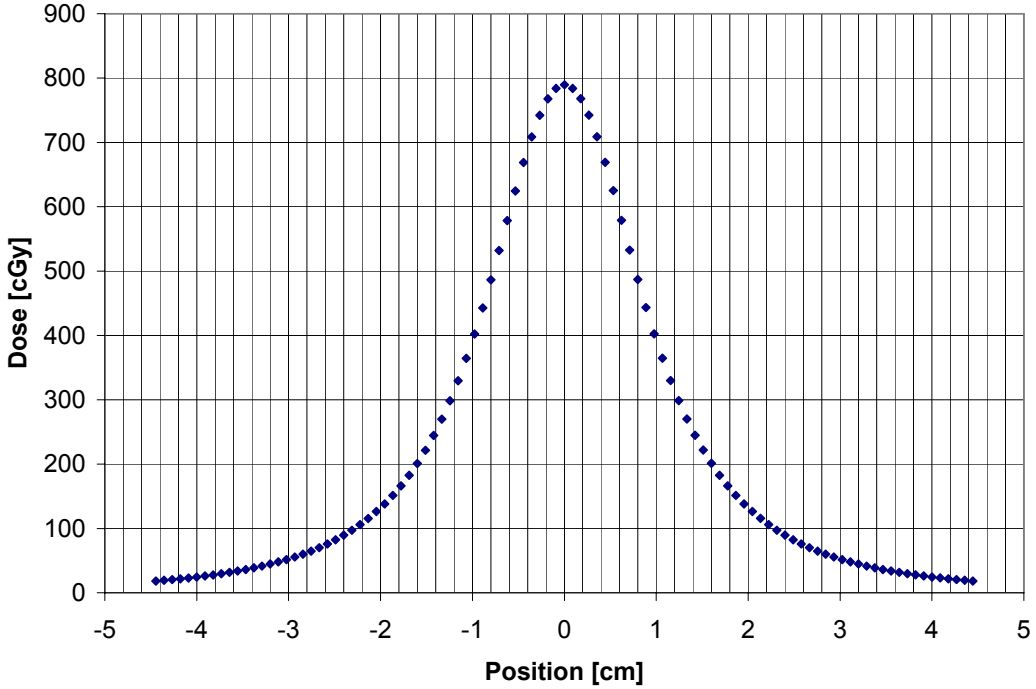

Figure 55: Calculated dose vs. position on film line profile for August 11, 2006.

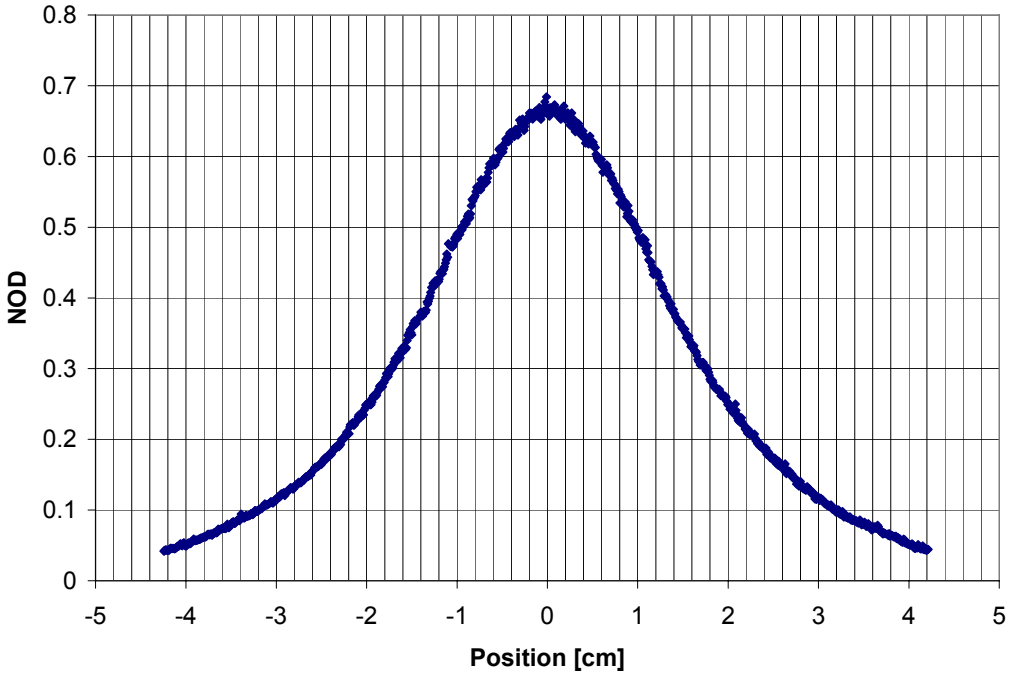

Figure 56: Measured net optical density vs. position on film line profile for August 11, 2006.

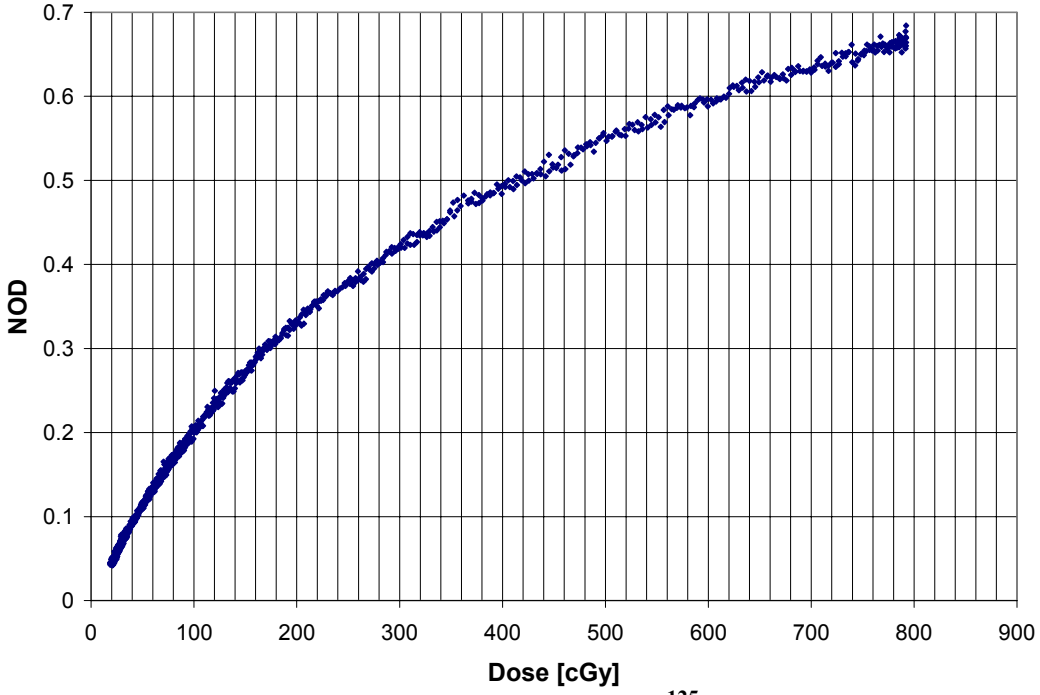

Figure 57: Film calibration curve obtained from ^{125}I seeds in PMMA phantom for August 11, 2006.

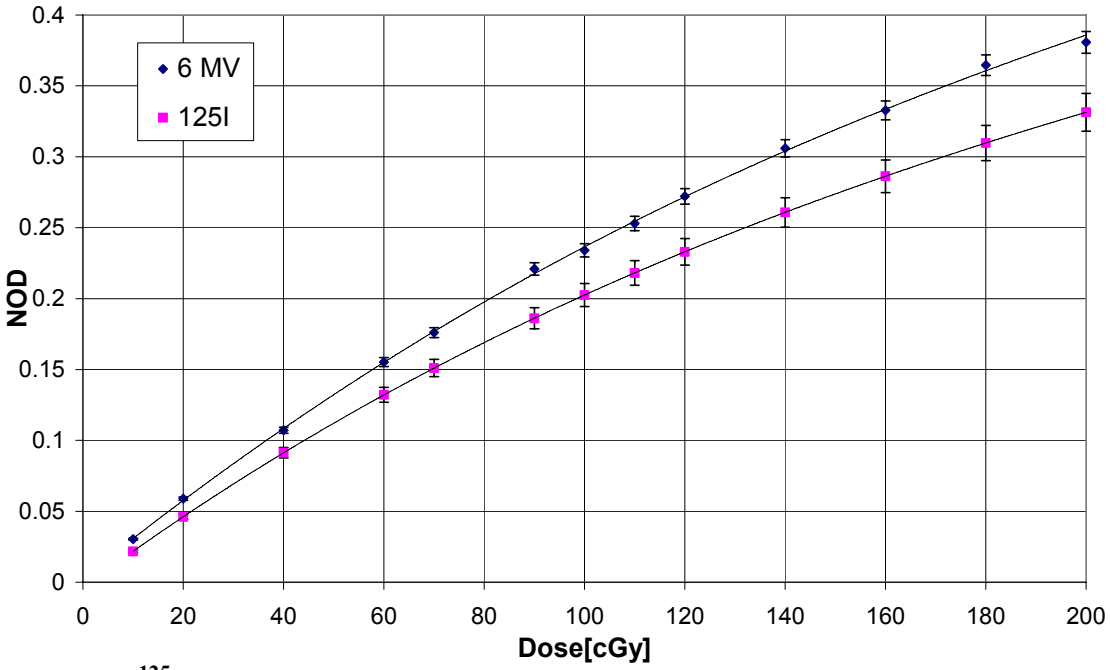

Figure 58: ^{125}I film calibration fit to fifth-order polynomial with 6 MV calibration for comparison. The error bars are the standard deviation of the mean of 5 independent measurements for the ^{125}I data and 3 measurements for the 6 MV calibration.

4.4.1.3 Orthovoltage X-ray Calibration

Orthovoltage calibration performed using 75-kVp (HVL = 1.86 mm Al) and 125-kVp (HVL = 2.96 mm Al) beams resulted in the calibration curves displayed in Figure 59. The 75-kVp beam was more sensitive, i.e. exhibited a slightly larger change in optical density per change in dose.

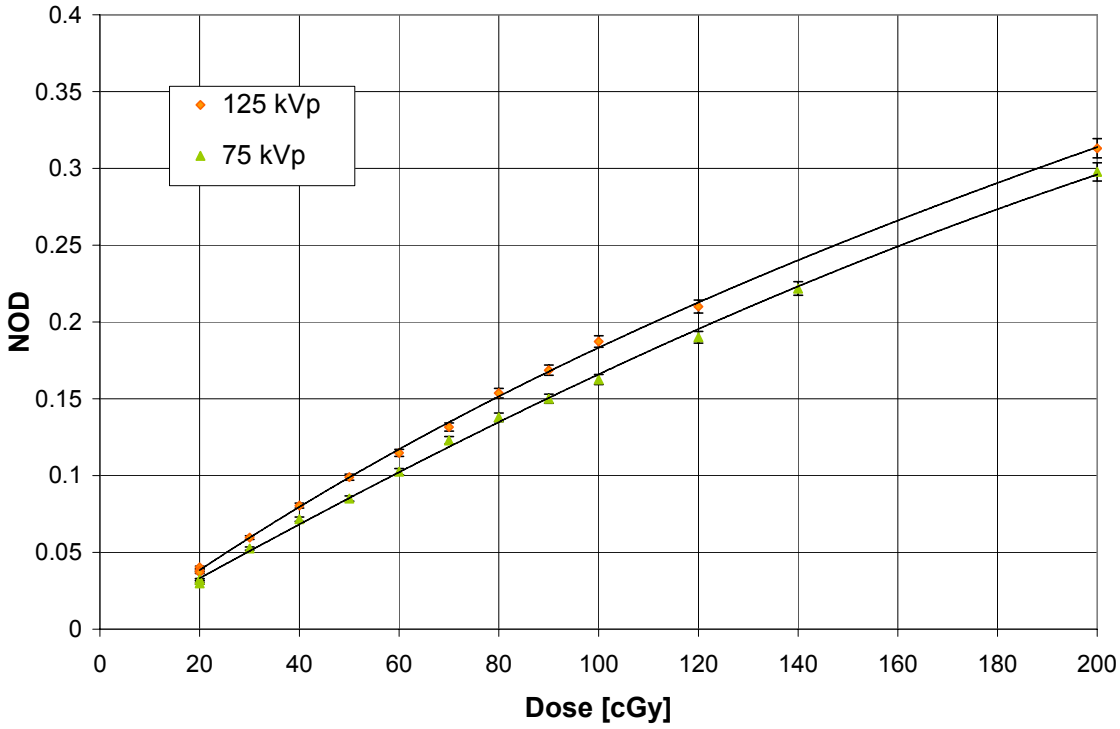

Figure 59: Calibration curves obtained from orthovoltage x-rays. Error bars are the standard deviation of the mean of 3 measurements.

4.4.1.4 Total Film Calibration Results

A comparison of all four calibration curves in the range of 0-2 Gy is shown in Figure 60. The 6 MV calibration curve exhibited the greatest sensitivity, i.e. the largest change in optical density per change in dose. The two orthovoltage calibrations exhibited the smallest change in optical density per absorbed dose with the 125 kVp and 75 kVp giving a 19% and 25% lower response than the 6 MV calibration at 2 Gy dose respectively.

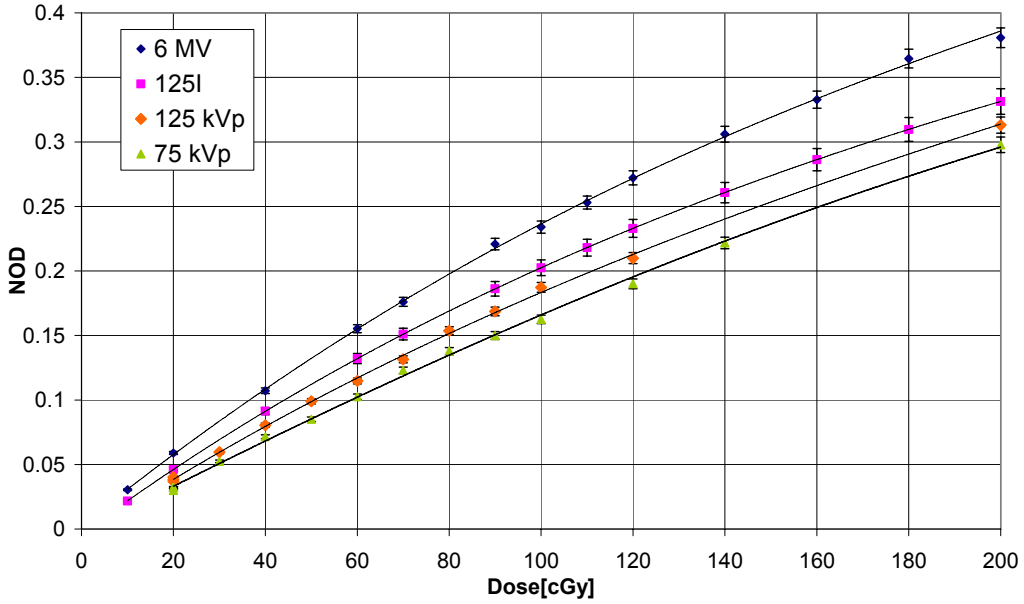

Figure 60: Comparison of 6 MV, ^{125}I, 125-kVp, and 75-kVp film calibrations.

Table 7 compares all four calibration methods at the 2-Gy exposure level. There was a variation in film response of 25%. Although Butson *et al* (2006) showed the film responded 7% less to 75-kVp and 125-kVp beams, our results showed 19% and 24% less, i.e. a significantly greater effect on beam quality. Table 8 compares the doses from each of the four curves for a net optical density of 0.3. Compared to 125 kVp, Table 8 shows that for a NOD of 0.3, the 75-kVp calibration overpredicts dose by 9%, the ^{125}I calibration underpredicts dose by 9%, and the 6 MV calibration underpredicts by 27%. These results are significantly different then those previously reported by ISP (2005) and Chui-Tsao *et al* (2005).

Table 7: Comparison of net optical density relative to the 6 MV calibration at 2-Gy absorbed dose for 4 calibration methods.

Beam	6MV	^{125}I	125 kVp	75 kVp
NOD	0.388	0.331	0.316	0.294
Relative NOD	1	0.853	0.814	0.756

Table 8: Comparison of dose predicted from calibration curves in Figure 60 for a net optical density of 0.3. Doses relative to 125 kVp results are also shown.

Beam	6MV	^{125}I	125 kVp	75 kVp
Dose cGy	138	172	188	204
Relative Dose cGy	0.73	0.91	1.00	1.09

4.4.2 Film Depth-Dose Measurements

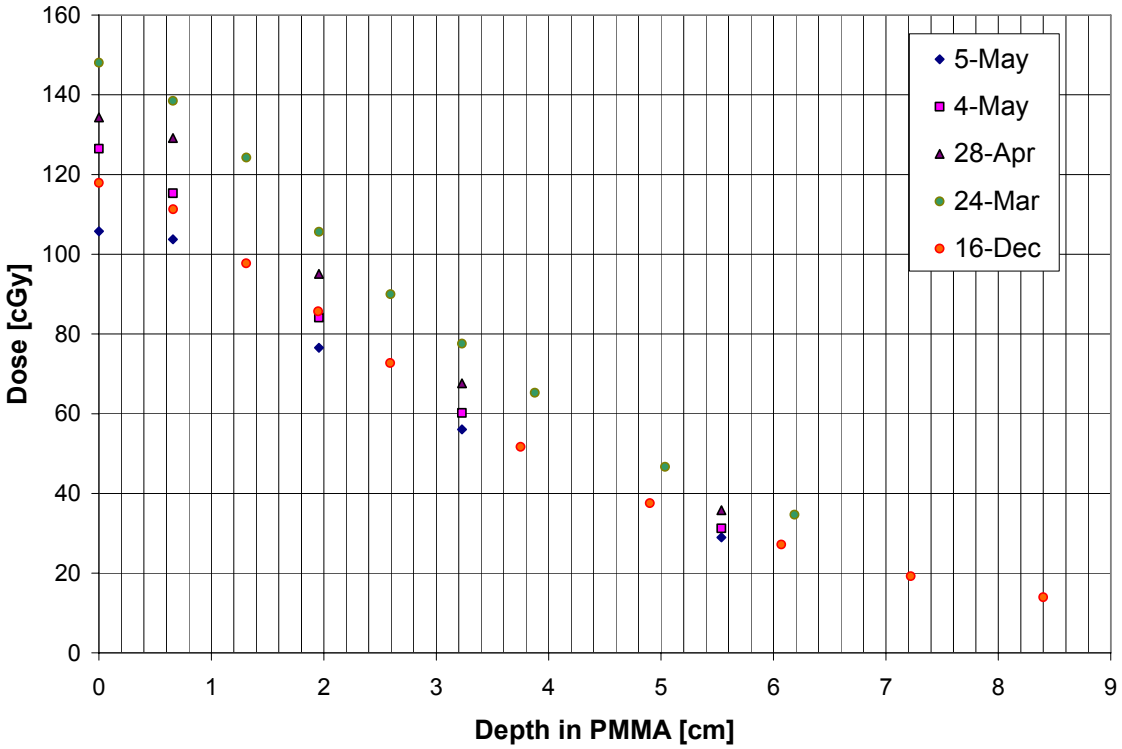

Figure 61: Film depth-dose comparisons from different experimental dates.

Depth-dose data for five independent measurement sessions, shown in Table 9, are plotted in Figure 61. Data at 2 cm were determined from the dose of the two nearest data points bracketing 2 cm using a non-linear, logarithmic interpolation. At 2-cm depth, ionization chamber doses ranged from 75.8 cGy to 105.2 cGy (Table 9).

The shapes of depth-dose curves for each of the 5 measurement sessions were compared by normalizing each curve to 1.00 at a depth of 2-cm. Figure 62 compares the curves by plotting points from all 5 fractional depth-dose measurements on one graph.

Table 9: Dose-to-water values obtained on separate dates at a depth of 2 cm in PMMA. Mean=88.5 cGy, Standard Deviation = 11.4 cGy.

Date	Film Dose [cGy]
5-May	75.8
4-May	83.2
18-Apr	94.0
24-Mar	105.2
16-Dec	84.1

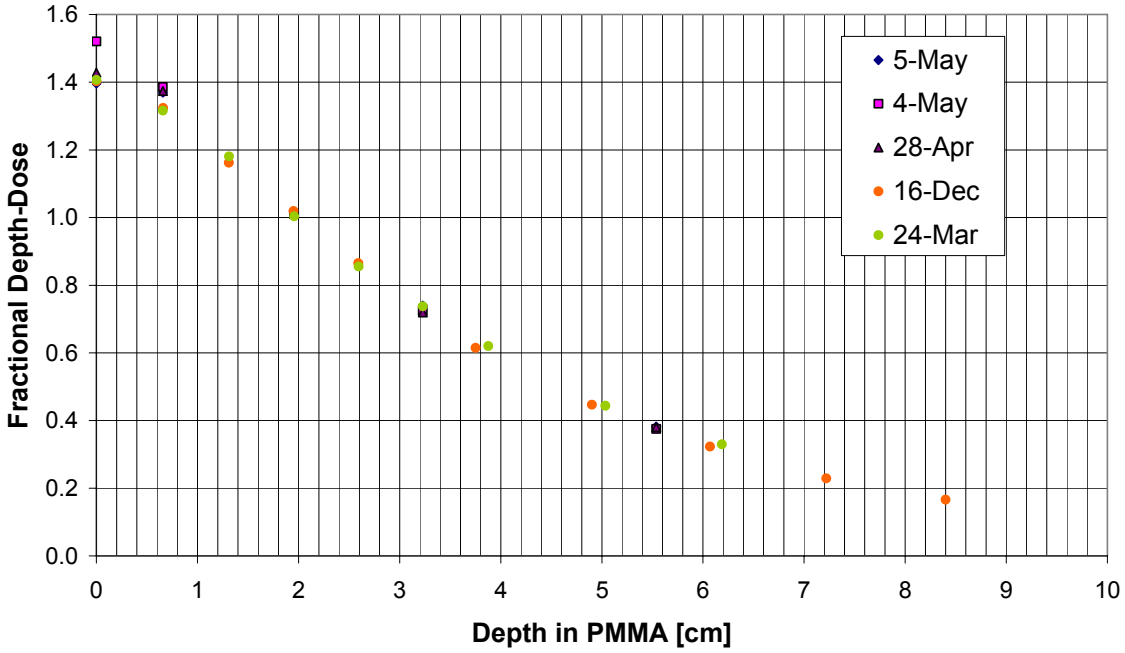

Figure 62: Fractional film depth-dose curves from film normalized by interpolated dose at 2 cm.

At depths greater than 1.5-cm, data from the 5 measurement sets agreed well with each other. The maximum measured fractional difference between any two data points at a common depth was -2.7% at a depth of 8.1 cm, and the average difference (± σ) between any 2 data sets was 1 ± 0.9% (N=16).

4.4.3 Ionization Chamber and Film Absolute Depth-Dose Comparison

Figure 63 through Figure 67 compare depth-dose measurements between ionization chamber and film for five independent measurement sessions. Table 10 compares ionization chamber and film measured doses at a 2-cm depth for each date. Both data sets show considerable variation in measured dose with fractional standard deviations of 9.2% and 12.9% indicating that ring current is not likely a good monitor of beam fluence for the tomography beamline. Table 10 also shows that, using the methodology reported in this study, film-measured doses underestimated ion chamber-measured doses by 5.1±2.3%.

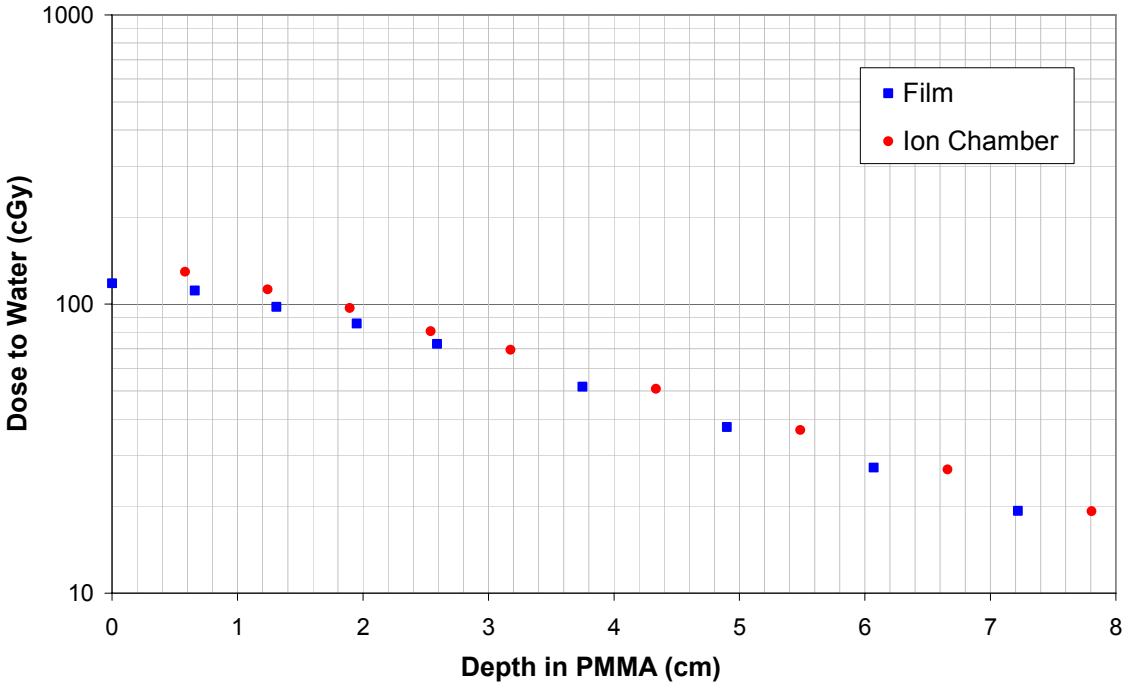

Figure 63: Film and ion chamber depth doses measured on December 16, 2006.

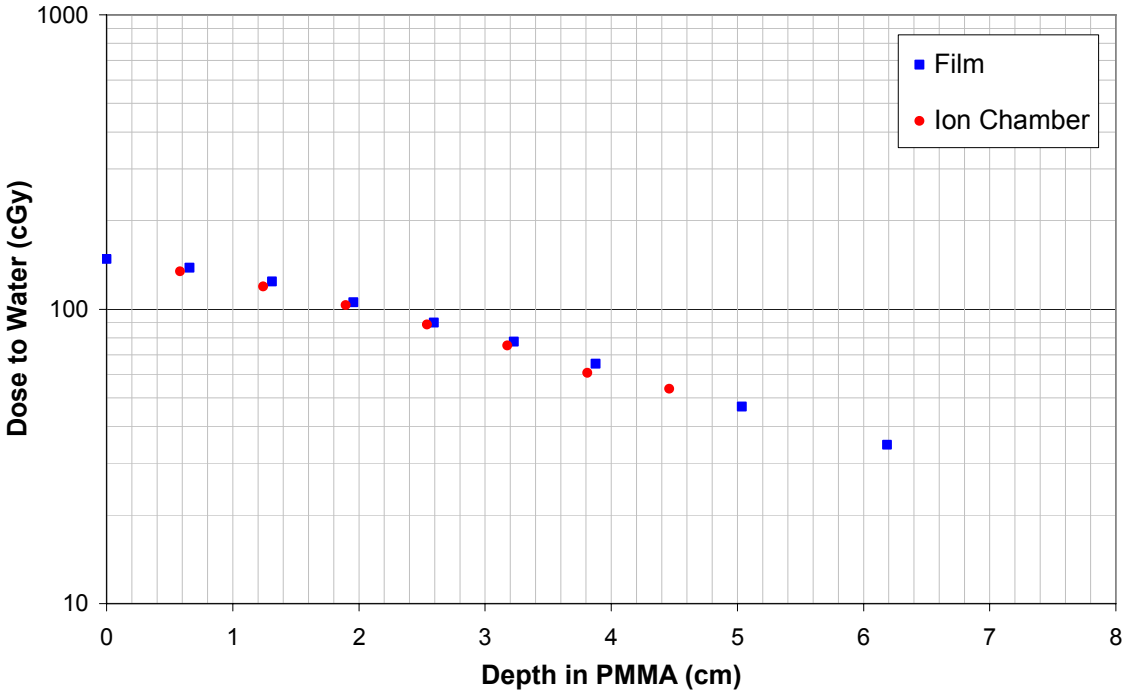

Figure 64: Film and ion chamber depth doses measured on March 24, 2007.

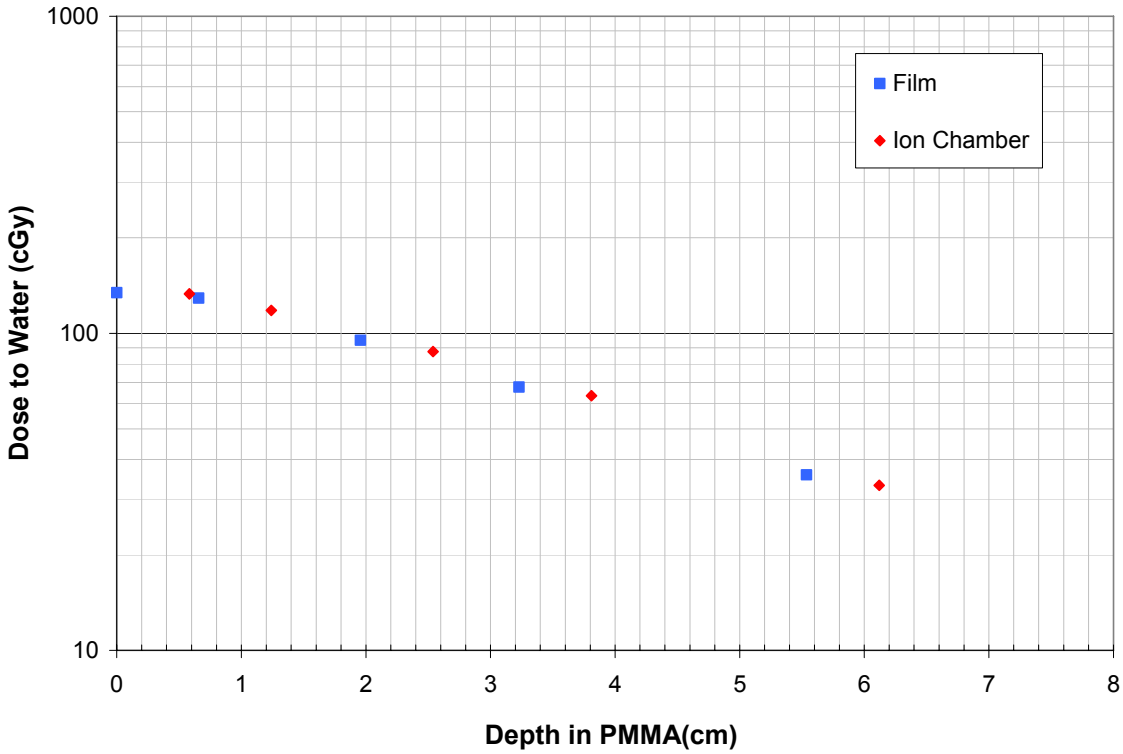

Figure 65: Film and ion chamber depth doses measured on April 28, 2007.

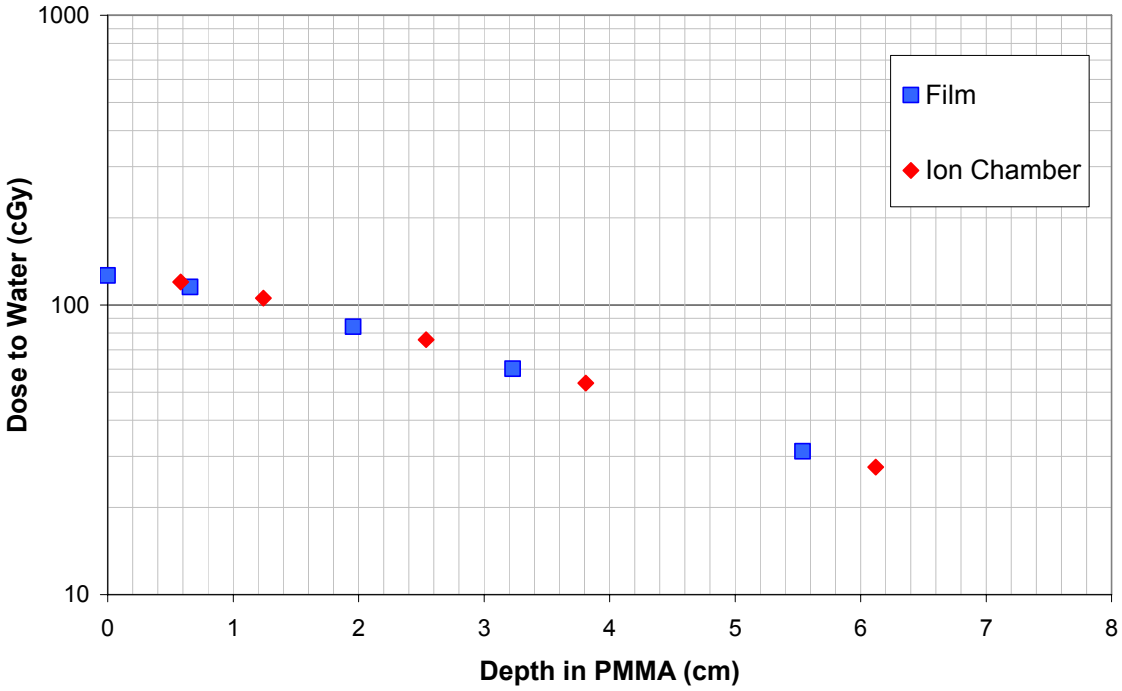

Figure 66: Film and ion chamber depth doses measured on May 4, 2007.

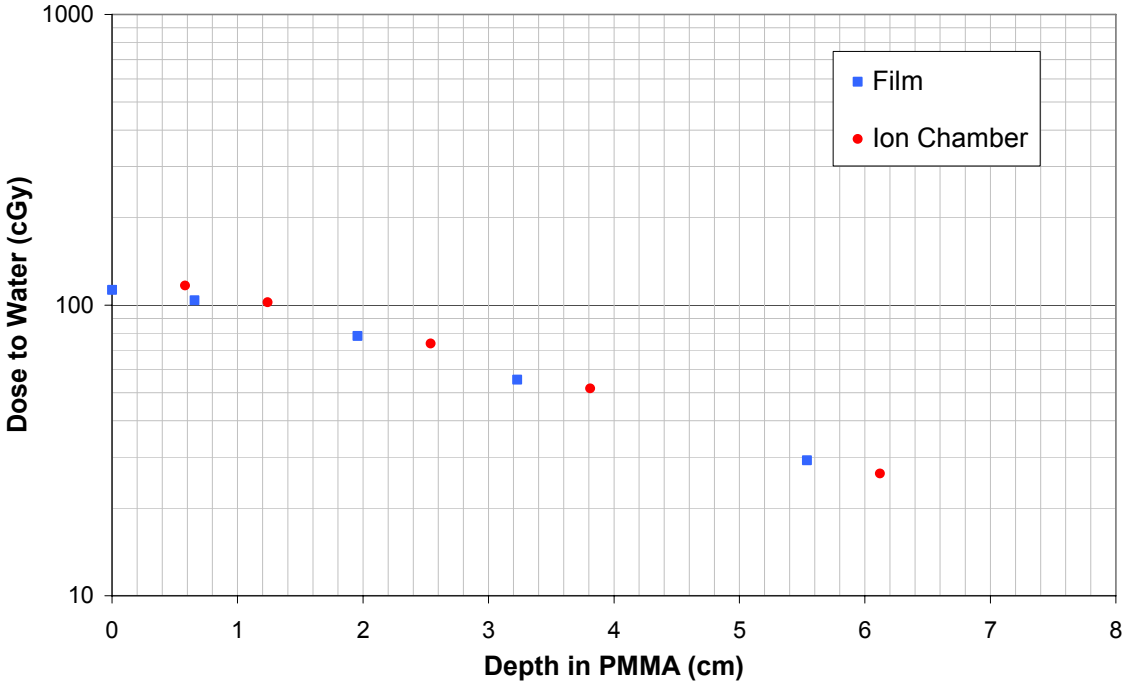

Figure 67: Film and ion chamber depth doses measured on May 5, 2007.

Table 10: Comparison of interpolated dose values at 2-cm depth for film and ionization chamber doses.

Date	Film Depth 2[cm]	IC Depth 2[cm]	%Difference
16-Dec	84.1	93.6	-10.7
24-Mar	105.2	101.8	3.3
18-Apr	94.0	99.7	-5.8
4-May	83.2	87.60	-5.2
5-May	75.8	81.2	-6.9
Mean	92.8	88.5	-5.1
σ_{mean}	3.8	5.1	2.3
σ	8.5	11.4	5.1
(σ/mean)×100%	9.2%	12.9%	

4.4.4 Ionization Chamber and Film Fractional Depth-Dose Comparison

To compare the shapes of the ion chamber and film fractional depth-dose curves, a polynomial (4th order) was fit to the log of the relative dose versus depth in PMMA for all data points at d>1.5 cm. Results showed that the two fractional depth-dose curves agreed well (Figure 68). The greatest differences were at the deeper depths with the maximum difference being fractional dose of film underestimating fractional dose of the ion chamber by 5.5% at a depth of 8.1 cm.

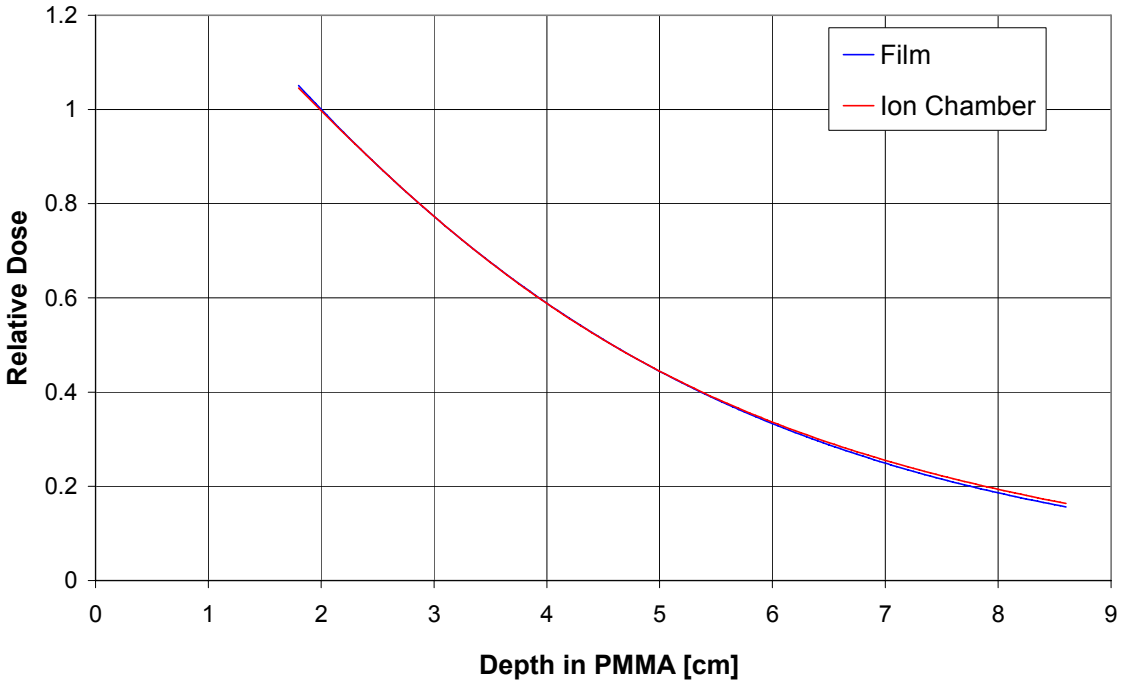

Figure 68: Ionization chamber and film fractional depth doses curves of established by fitting relative depth dose curves.

4.5 Discussion

Calibration of EBT film shows a strong energy dependence contrary to results published by ISP (2005) and Chui-Tsao *et al* (2003). This might in part be due to the wavelength of light used to analyze the film may influencing the energy dependence exhibited. It may be worthwhile to analyze the calibration films with different wavelengths of light to study the response difference between films with the same absorbed dose delivered from different beam energies.

For all calibrations except for those performed with ^{125}I brachytherapy seeds, the response of the film increases with decreasing effective beam energy. For doses lower than 4 Gy, the ^{125}I calibration curve lies above both the 75-kVp (E_{eff} = 2.7 keV) and 125-kVp (E_{eff} = 31 keV) orthovoltage calibrations; however, its effective beam energy (~29 keV) lies between them. Beyond 4 Gy, the ^{125}I curve (NOD vs. Dose) crosses the

125-kVp curve. In the ^{125}I calibration curve, because higher absorbed doses correspond to a higher dose rates, the response discrepancy may be partly a result of a dose rate effect.

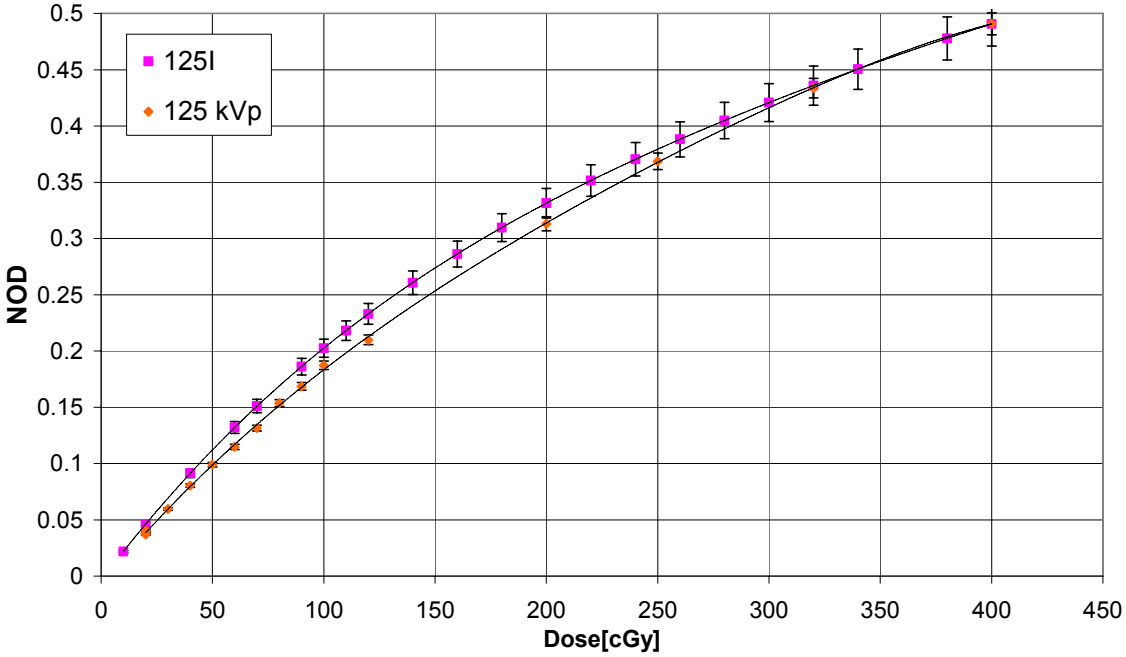

Figure 69: Calibration comparison from ^{125}I seeds and 125-kVp orthovoltage calibration. Note the better agreement at higher doses.

When considering the strong energy dependence, some error in absolute dose measurements when using EBT film was expected as the films were not calibrated with a beam identical to the 35-keV synchrotron beam in which research was performed; rather the 125-kVp calibration was used

5. Aim 4, Comparison of Measurements with Fluence-Based Dose Calculations

Compare results of film and ion chamber dose measurements to dose determined from fluence measurements (MCNP5 Monte Carlo).

5.1 Goal

Compare film and ionization chamber measured depth-dose with dose calculated from the product of measured fluence and MCNP-calculated dose per fluence.

5.2 Theory

The CAMD tomography beam was modeled in MCNP5 Monte Carlo simulations as a parallel, 2.5×2.8 cm^2, monochromatic, 35-keV beam (from Dugas *et al*, 2007). The PMMA slab phantom was modeled as a solid block of PMMA surrounded by air, and Monte Carlo output (dose per incident fluence) was scaled using a fluence calculated from measured Compton scattered photons measured using a thin-windowed NaI(Tl) detector.

5.3 Materials and Methods

5.3.1 Beam Fluence Measurement

The scintillation detector was used to measure the fluence of the CAMD synchrotron-generated beam by counting the number of interactions in its active volume during the previously described Compton spectroscopy experiment (section 2.3.5.1).

As mentioned in section 2.3.5.1., the CAMD synchrotron-generated beam was too intense for the NaI(Tl) detector to be positioned directly in the beam path. However, the beam's fluence could be indirectly determined by analyzing the Compton scattered radiation. Since the mean beam energy, the target material's chemical composition and thickness, and solid angle subtended by the detector's face are known, the initial beam fluence could be found through calculation and application of the Klien Nishina cross-

section. To reiterate, the experimental setup of the Compton spectroscopy experiments (section 2.3.5.1), is shown in Figure 70.

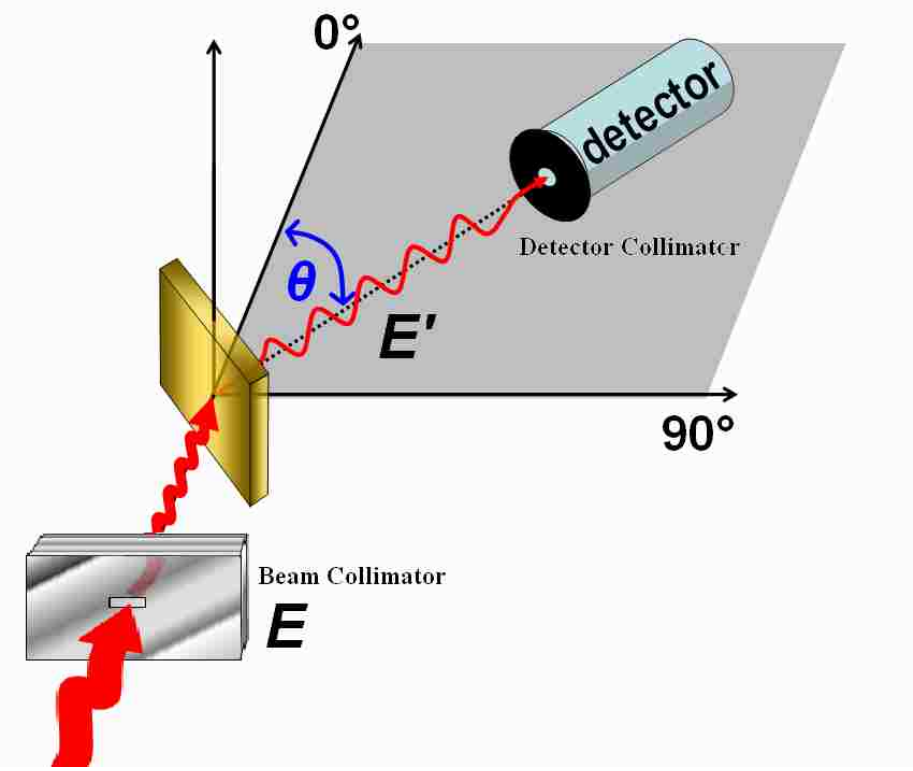

Figure 70: Compton scatter experimental setup for fluence measurements.

The incident beam's central-axis photon fluence rates, $\dot{\phi}_o$ ($s^{-1} \cdot cm^{-2}$), were calculated using:

$$\dot{\phi}_o = \dot{C}_m \left[N_A \cdot \rho \cdot (Z/A) \cdot (t/\cos\theta) \cdot \Delta\Omega \cdot A_{beam} \cdot \varepsilon \cdot (d_e\sigma / d\Omega) \right]^{-1}, \qquad (5\text{-}1)$$

where:

$\dot{C}_m$ is the net peak count rate,

N_a is Avogadro's number,

ρ is the density of polyethylene (0.884 $g \cdot cm^{-3}$),

Z is the net atomic number of polyethylene, (16),

A is the molecular weight of polyethylene, (28.06 g/mol),

t is the polyethylene scatterer thickness (0.08 cm or 0.05 cm),

θ is the scattering angle(15º, 30º, 45º or 60º),

$\Delta\Omega$ is the solid angle subtended by acquired Compton scattered photons,

A_{beam} is the area of the collimated beam (cm^2),

ε is the detector's intrinsic efficiency, and

$\left(d_e\sigma / d\Omega\right)$ is the Klien-Nishina cross section (cm^2).

$\dot{C}_m$, the net peak count rate , was obtained by summing the net counts under the full energy and iodine escape peaks (Figure 71) and dividing by the total time of acquisition (1000 seconds); the solid angle, $\Delta\Omega$ (1.24E-4 Sr), was determined by dividing the area of the detector-collimator aperture (0.195 cm^2) by the square of the scatterer-detector distance (39.7 cm); A_{beam}, the area of the collimated beam area was determined from the beam collimator's aperture; ε, the detector's intrinsic efficiency was taken as unity, as Knoll *et al* (2002) indicates that a NaI(Tl) detector at this thickness (0.1 cm) operates at full efficiency for photon energies near the iodine k-shell binding energy (Figure 72); and $(d_e\sigma / d\Omega)$, the Klien-Nishina collision cross section, was calculated using the formula given by Evans *et al* (1955) for polarized incident radiation:

$$(d_e\sigma / d\Omega) = \frac{{r_0}^2}{2}\left(\frac{E'}{E}\right)^2\left(\frac{E}{E'} + \frac{E'}{E} - 2\sin^2\theta\cos^2\eta\right), \qquad (5\text{-}2)$$

where:

r_o is the classical electron radius (2.818E-13 cm),

E and is the initial beam energy (keV),

E' scattered photon energy (keV), and

η is the angle between the uncollided beam-Compton scattered photon plane and the beam's plane of polarization.

E′ was calculated using the Compton scattering (Equation 2-1) from the measured Compton-scattered peak energy centroids. Experiments performed by Dugas *et al* (2007) found that the beam is highly polarized in the horizontal plane, and thus, $\eta = 0$.

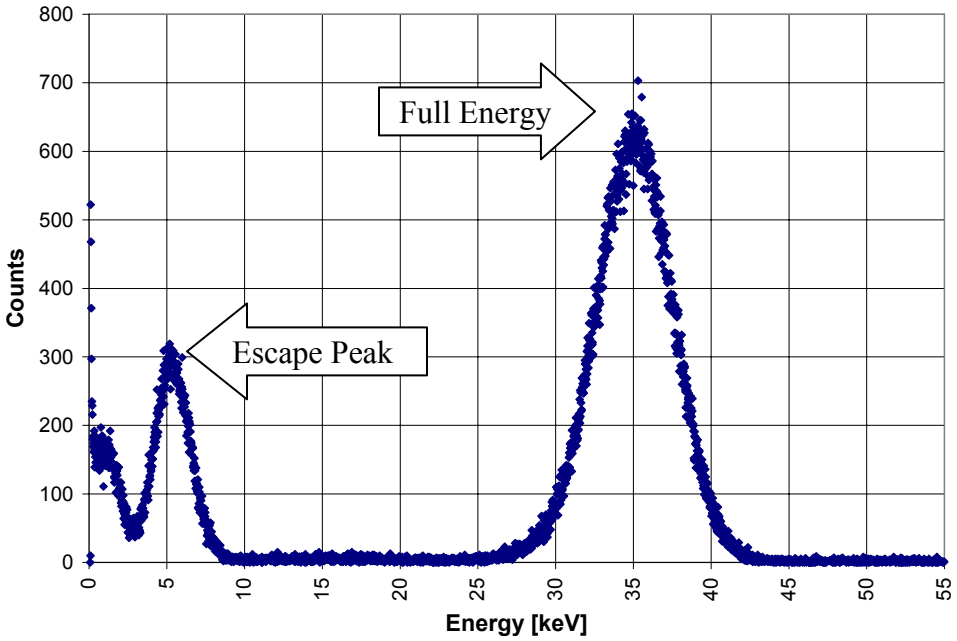

Figure 71: Multi-channel analyzer spectrum showing full energy and iodine escape peaks of 35-keV photon scattered through 45°.

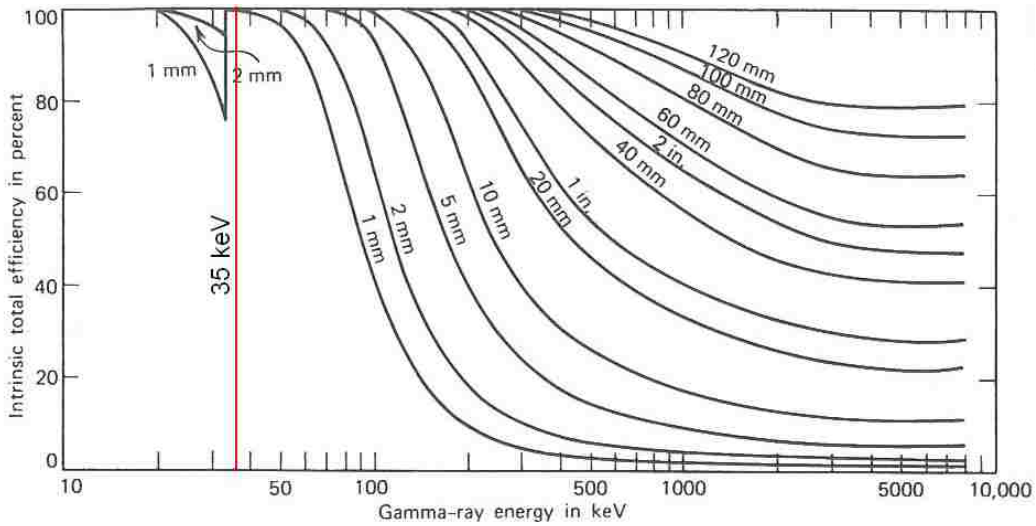

Figure 72: NaI(Tl) detector efficiency for gamma ray energies in varying active volume thicknesses (Knoll, 2000).

5.3.2 Monte Carlo Simulation

Monte Carlo simulations were performed using the general Monte Carlo N-particle Transport Code (MCNP5) by Dugas *et al* (2007). The PMMA slab phantom geometry was simulated as an 11×11×12.5-cm^3 homogenous PMMA volume surrounded by air. The beam was modeled as a parallel monoenergetic 35-keV photon beam originating from a uniform 2.8×2.5-cm^2 distribution located 10 cm upstream from the phantom surface. Energy deposition ($MeV \cdot g^{-1} \cdot \gamma^{-1}$) was tallied in $(0.1\ cm)^3$ voxels along the beam's central axis. Dose for each voxel was reported at the voxel's center. It was assumed that the energy deposition ($MeV \cdot g^{-1} \cdot \gamma^{-1}$) equaled the dose ($MeV \cdot g^{-1}$) per incident particle ($D_{mc} \cdot \gamma^{-1}$).

The Monte Carlo dose to water at depth *d* was determined by:

$$D^{MC}(d) = \left(D/\phi\right)_d^{MC} \cdot \phi_{BB} \cdot \left(\mu_{en}/\rho\right)_{PMMA}^{Water}, \qquad (5\text{-}3)$$

where:

ϕ_{BB} is the fluence of the broad beam (cm^{-2}),

$\left(\mu_{en}/\rho\right)_{PMMA}^{Water}$ is the mass energy absorption coefficient ratio of water to PMMA values obtained from NIST (1.015) (Hubbell *et al*), and,

$\left(D/\phi\right)_d^{MC}$ is the dose per fluence output of the MCNP5 Monte Carlo calculations,

The broad-beam fluence is determined from the measured fluence rate of the collimated beam by:

$$\phi_{BB} = \dot{\phi}_o \cdot \left(\frac{h_0}{h_{BB}}\right) \cdot T_{irr}, \qquad (5\text{-}4)$$

where:

h_o is the height of the slit for the narrow beam (≈ 0.1 cm),

h_{bb} is the height of the broad beam, which was determined from film measurement, and equal the amplitude of the stage movement (≈ 2.5 cm) (section 2.3.4), and

T_{irr} is the irradiation time dictated by the movable stage program (320 seconds) (section 2.3.4).

5.4 Results

5.4.1 Comparison of Measured Depth-Dose with Fluence-Scaled, Monte Carlo Simulations

Figure 73 through Figure 77 compares results of depth dose measurements using Gafchromic EBT film and ionization chamber dosimetry methods with simulated MCNP5 depth doses scaled using fluence measurements obtained on the same date. Results for each of the five figures correspond to five independent dose intercomparisons at different dates over an approximately five-month period.

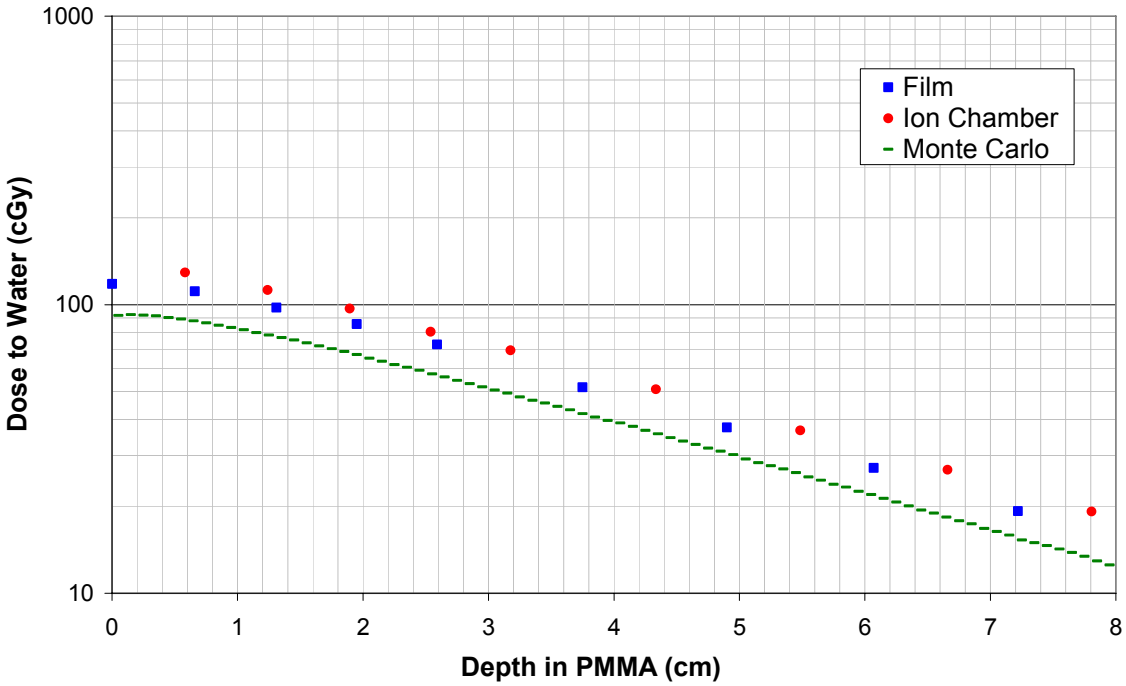

Figure 73: Depth dose measurements with Monte Carlo simulations from December 16, 2006.

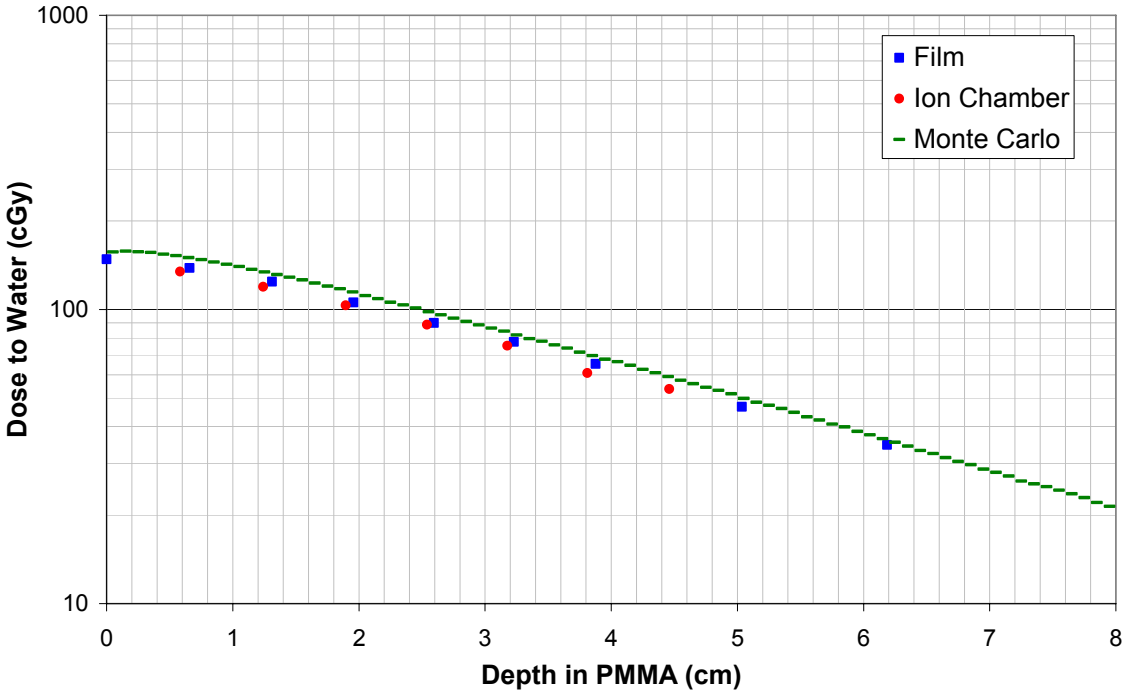

Figure 74: Depth dose measurements with Monte Carlo simulations from March 24, 2007.

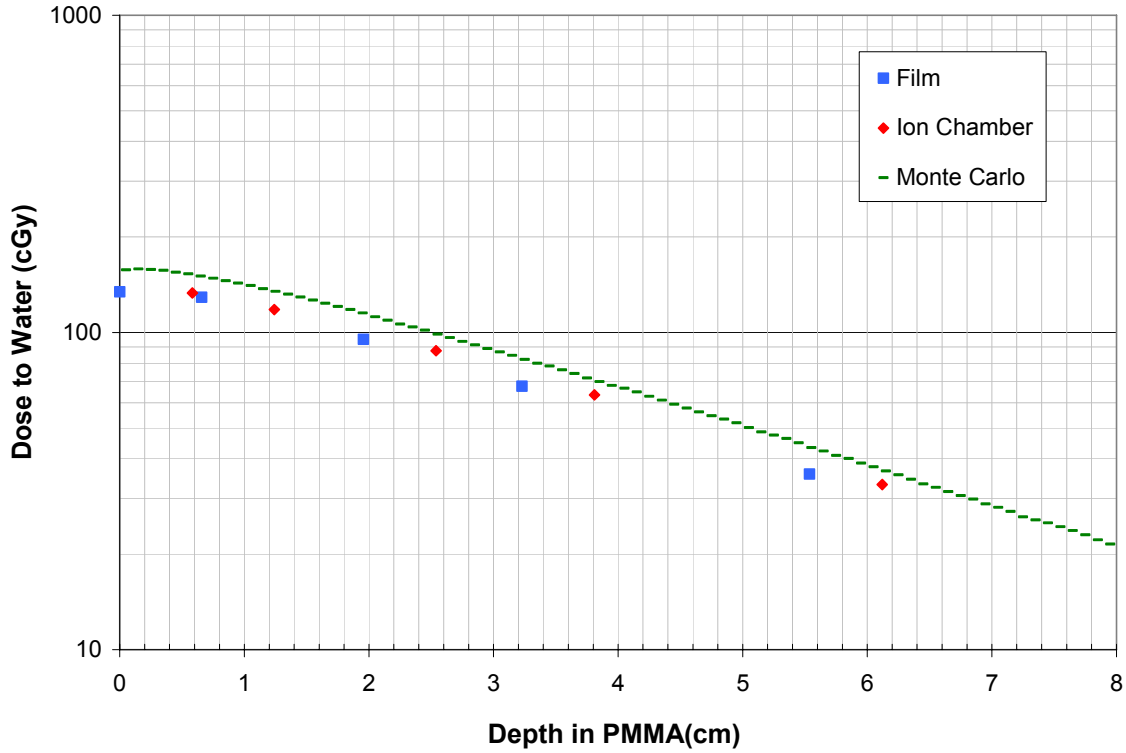

Figure 75: Depth dose measurements with Monte Carlo simulations from April 28, 2006.

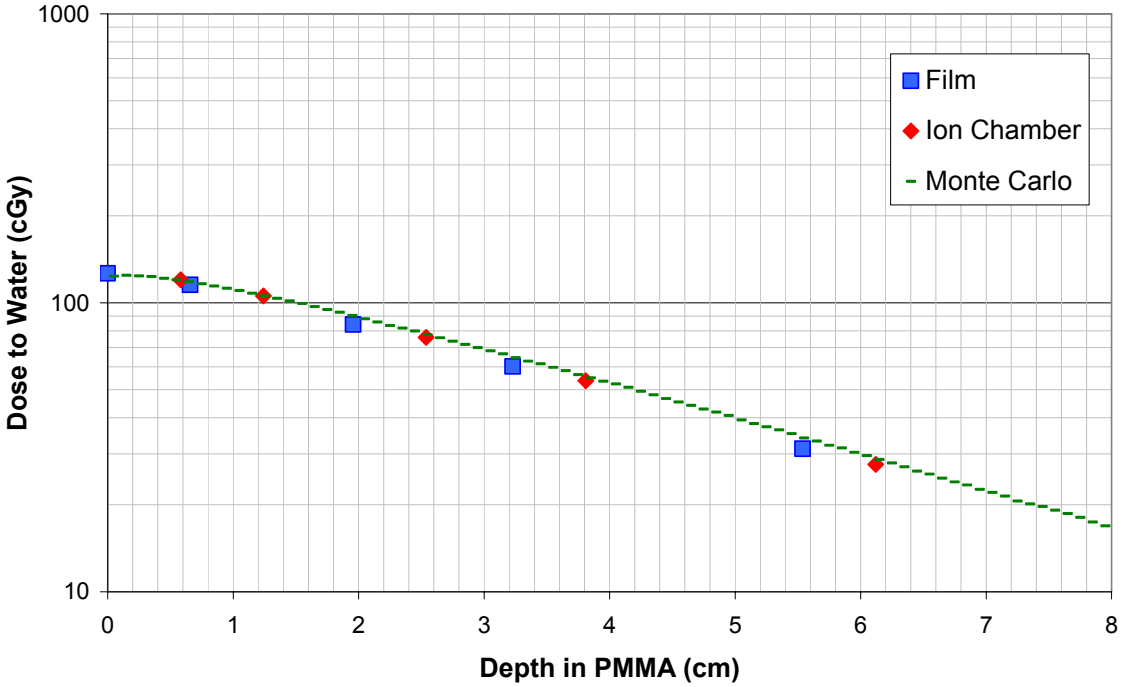

Figure 76: Depth dose measurements with Monte Carlo simulations from May 4, 2007.

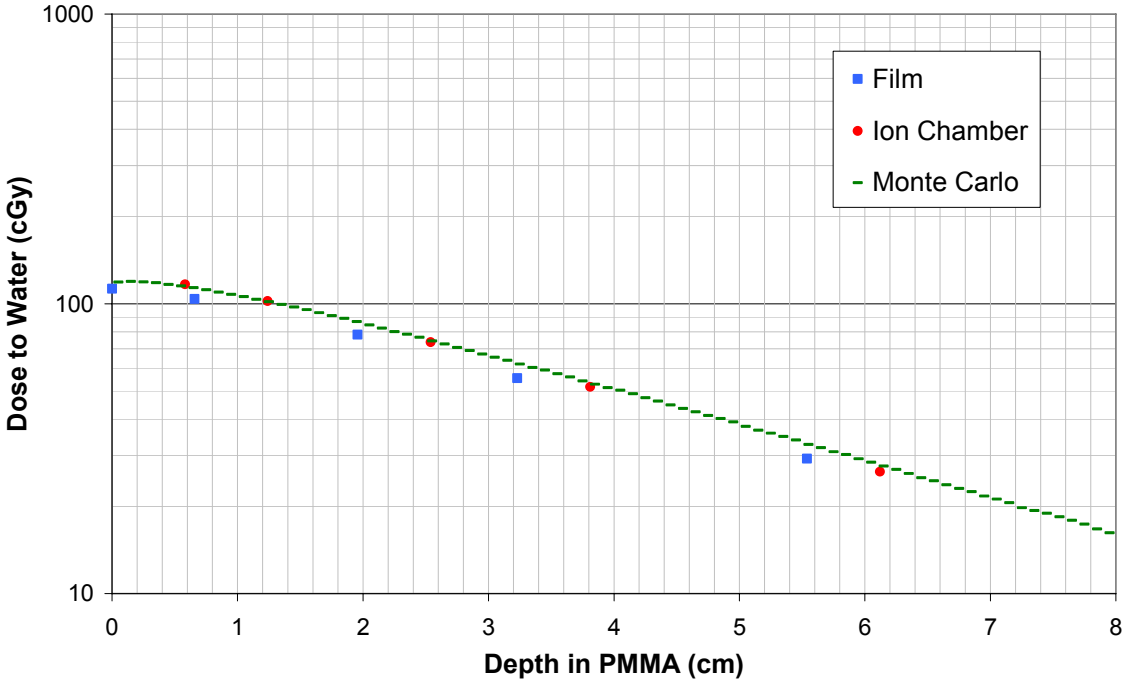

Figure 77: Depth dose measurements with Monte Carlo simulations from May 5, 2007.

The ionization chamber-Monte Carlo disagreement, averaged over all ion-chamber dose points for all experimental dates, was -6.4±0.8%, while film-Monte Carlo disagreement averaged -9.1±0.7%. The best ion chamber-Monte Carlo agreement and film-Monte Carlo agreement occurred on May 5, 2007, with ionization chamber measured dose underestimating Monte Carlo-based dose by 1.5±0.86% and film measured dose underestimating Monte Carlo based dose by 9.0±2.3%. The worst ion chamber-Monte Carlo agreement and film-Monte Carlo agreement occurred on April 28, 2007, with an ionization chamber measured dose underestimating Monte Carlo based dose by 11.4±1.1% and a film measured dose underestimating Monte Carlo based dose by 16.4±1.7%. The Monte Carlo based dose simulation on December 16, 2006 was taken as an outlier and was not considered in the average depth dose comparisons.

5.4.2 Fractional Depth-Dose Comparisons

The Monte Carlo output, converted to a fractional depth dose by normalizing all dose values to 1.00 at 2 cm, was compared to ionization chamber and film measured fractional depth doses (Figure 78 and Figure 79).

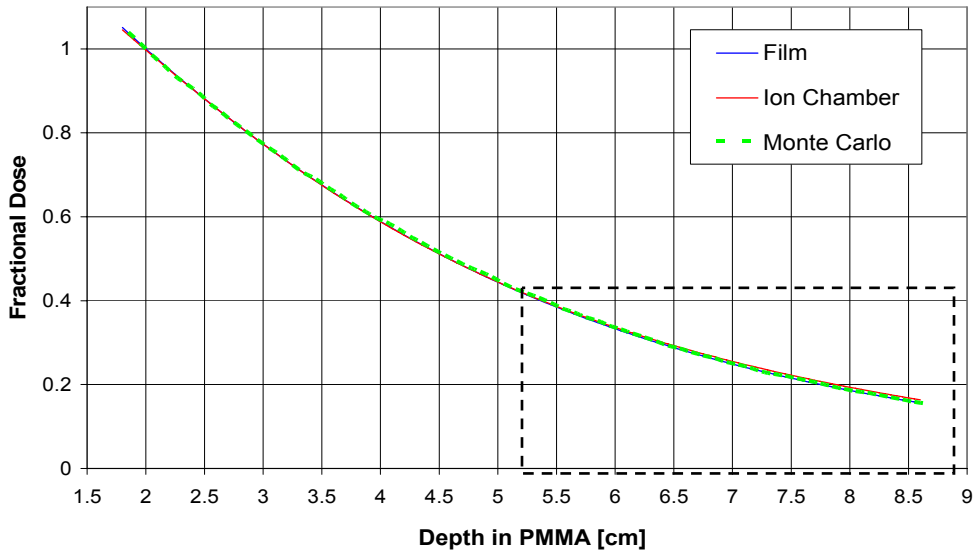

Figure 78: Average fractional dose versus depth curves of all fractional ionization chamber and film measured data compared to Monte Carlo. Figure 79 shows the boxed portion enlarged.

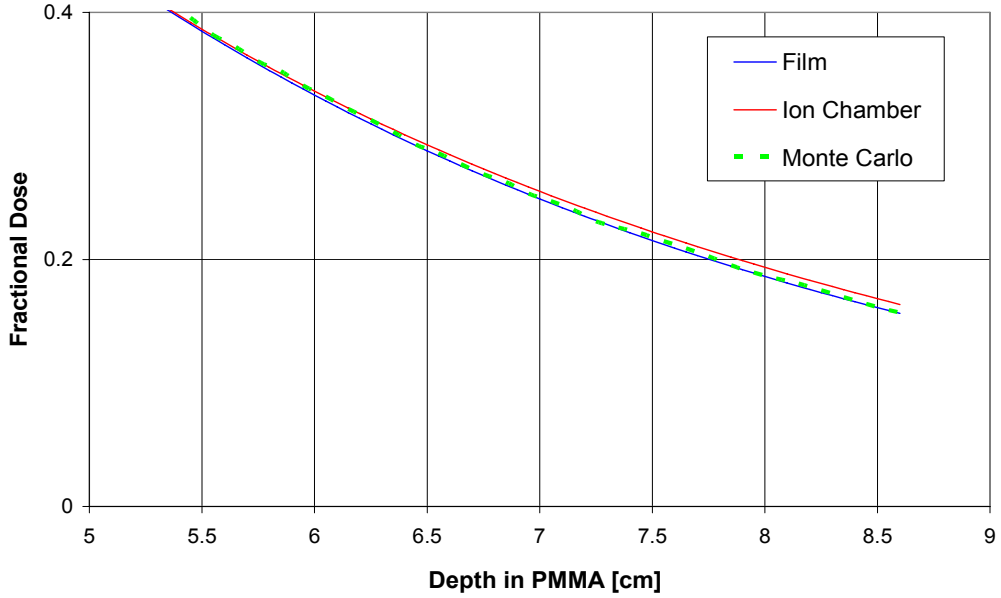

Figure 79: Boxed portion of Figure 78 enlarged to show detail.

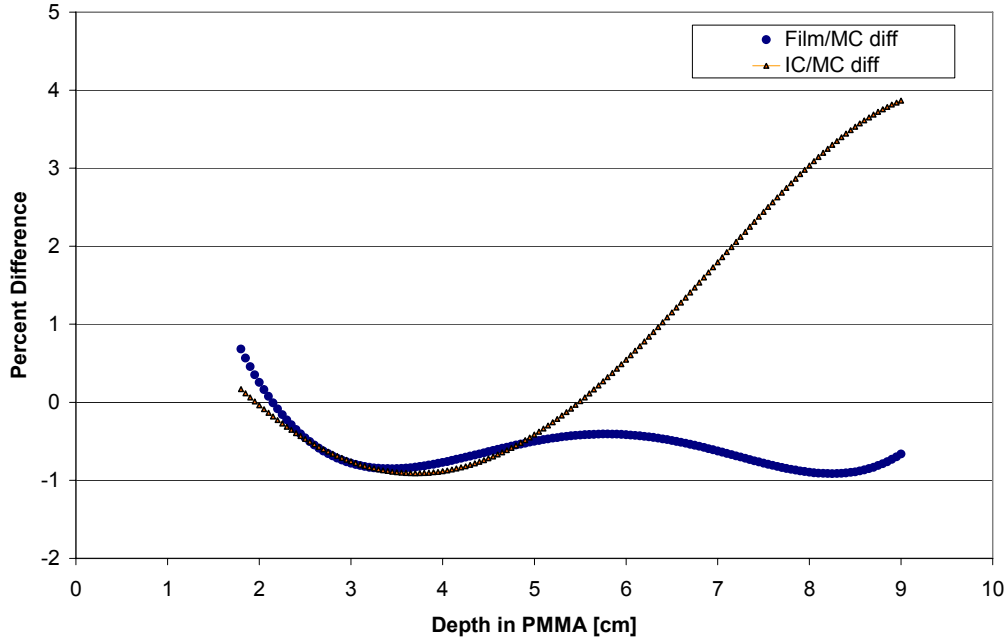

Figure 80: Percent difference of film and ionization measurements chamber compared to Monte Carlo simulations plotted against depth in PMMA.

Figure 80 shows that the ionization chamber fractional depth-dose measurements exhibited greater disagreement when compared to the fractional Monte Carlo-calculated curves than did the film fractional depth-dose measurements. The maximum ionization

chamber-Monte Carlo relative disagreement was 3.85% at 9.0-cm depth while maximum disagreement with film was 0.92% at 8.25-cm depth.

5.5 Discussion

The ionization chamber's depth-dose curves are closest to those of the Monte Carlo except for data acquired in March, 2007. The reason why the March film depth-dose curve was higher than ionization chamber is unknown, but likely due to random error.

Measured fractional film depth-dose curves agreed better with fractional Monte Carlo fractional depth-dose curves than did measured fractional ionization chamber curves. This possibly indicates a need for depth dependence in the factors used in TG-61 for converting ionization to dose. However, because the disagreement is still relatively small, even at a depth of 9 cm, ionization chamber measurements should still be appropriate for future dosimetry experiments, as cell and small animal experiments will not require dose determination at depths greater than a few centimeters.

6. Conclusions and Recommendations

The hypothesis of this thesis is that depth-dose measured in a PMMA phantom using an air-equivalent ionization chamber and radiochromic film dosimeters in a PMMA phantom irradiated by a 35-keV, monochromatic x-ray beam (CAMD tomography Beamline) will agree to within 5% of each other and to within 5% of dose determined from fluence-scaled Monte Carlo dose simulations.

6.1 Summary of Results

At a 2-cm depth in PMMA, film-measured dose to water underestimated ion chamber-measured dose to water by 5.0±2.1%. Over depths ranging from 0-8cm in PMMA, film-measured fractional dose to water agreed well with ion chamber-measured fractional dose, the greatest difference being film-measured fractional dose underestimating ion chamber-measured fractional dose by 5.5% at a depth of 8.1 cm. Averaged over all depths ranging from 0-8 cm in PMMA and over four independent depth-dose measurement sessions, ion chamber-measured dose underestimated dose based on fluence measurements and MCNP4 calculations by 6.4±0.8%. Averaged over all depths ranging from 0-8 cm in PMMA and over four independent depth-dose measurement sessions, film-measured dose to water underestimated dose to water based on beam fluence measurements and MCNP4 calculations by 9.1±0.7%. Over depths ranging from 0-8cm in PMMA, ion chamber-measured fractional dose to water agreed well with MCNP4-calcualted fractional dose, the greatest difference being ion chamber-measured fractional dose to water underestimating MCNP4-calcualted fractional dose by 3.85% at a depth of 9.0 cm. Over depths ranging from 0-8cm in PMMA, film-measured fractional dose to water agreed well with MCNP4-calcualted fractional dose, the greatest difference being

film-measured fractional dose underestimating MCNP4-calcualted fractional dose by 0.92% at a depth of 8.25 cm.

6.2 Conclusions

Results of this research were unable to prove or disprove the hypothesis for the ion-chamber and film dose measurements at a 2-cm depth.

Results of this research showed the hypothesis was proved false for the agreement between either ion chamber-measured dose to water or film-measured dose to water and dose determined from fluence-scaled Monte Carlo dose simulations.

Variation in Beam Output: Spread in measured dose values, but not in the measured fractional dose values from multiple data sessions, indicated that beam current was not a reliable monitor of beam output.

Conversion of Ionization to Dose: Small differences between ion chamber-measured fractional dose to water and MCNP4 percent depth-dose calculations at deeper depths indicated that ionization to dose conversion factors depend on depth.

Conversion of Film Density to Dose: Small differences between film-measured fractional dose to water and MCNP4 percent depth-dose calculations at deeper depths indicated that there is not a significant variation in factors converting film density to dose as function of depth.

6.3 Recommendations for CAMD Beamline

Energy Settings: The monochromator settings, calibrated using K-edge absorptions, should be used to dial in the energy. Silicon powder diffraction is a quick and accurate method for verifying beam energy and is recommended

Beam Uniformity: The beam should be made uniform (symmetric) in the horizontal direction by either a variable width (trapezoidal) vertical jaws or by a 1D aluminum wedge.

Beam Monitor: The x-ray beam current should be monitored using a transmission ion chamber to provide monitor units in lieu of the ring current.

Beam Measuring Equipment: The CAMD tomography beamline, when used for medical radiology, should be equipped with the beam measurement equipment used to perform ion chamber dosimetry, radiochromic film dosimetry, Compton scattering measurements, and powder diffraction energy measurements.

6.4 Recommendations for Future Studies

Ion Chamber Dosimetry: The TG-61 protocol should be expanded to include monochromatic keV photon beams. Initial work should determine appropriate TG-61 factors using Monte Carlo calculations, and an inclusion of depth-dependence of factors would also be useful

Film Dosimetry: Radiochromic film should be calibrated against ion chamber-measured dose in the monochromatic keV photon beam.

Dosimetry Intercomparisons: The data from this study can be reanalyzed following any new or more appropriate ion chamber dosimetry protocol. Additional dosimetry intercomparisons should be made using more accurate methods for fluence measurements (i.e. ensuring systematic error is less than 1%) for comparison with ion chamber dosimetry.

References

Boudou C, Biston M C, Corde S, Adam J F, Ferrero C, Esteve F, and Elleaume H, 2004, Synchrotron Stereotactic Radiotherapy: Dosimetry by Fricke Gel and Monte Carlo Simulations. Phys Med Biol 2004;49:5135-5144.

Butson M J, Cheung T, and Yu K.N, 2006, Weak Energy Dependence of EBT Gafchromic Film Dose Response in the 50kVp-10 MVp X-ray range. Applied Radiation and Isotopes 64 60-62

Carroll F E, 2002, Tunable Monochromatic X-rays: A New Paradigm in Medicine, American Roentgen Ray Society 179 583-590

Carroll F, 2003, Tunable, Monochromatic X-rays: An Enabling Technology for Molecular/Cellular imaging and Therapy. Journal of Cellular BioChemistry 90 502-508

Chiu-Tsao S T, Ho Y, Shankar R, Wang L, and Louis H, 2005, Energy Dependence of Response of New High Sensitivity Radiochromic Films for Megavoltage and Kilovoltage Radiation Energies. Med. Phys 32 (11) 3350-3354

Dugas J P, Oves S, Sajo E, Matthews K L, Ham K, and Hogstrom K R, 2007, Monochromatic Beam Characterization for Auger Electron Dosimetry and Radiotherapy at CAMD, European Journal of Radiation (submitted for publication)

Edwards C R, Green S, Palethorpe J E, and Mountford P J, 1997, The Response of a MOSFET, p-type Semiconductor and LiF TLD to Quasi-Monoenergetic X-rays. Phys Med Biol 1997;42:2383-2391.

Evans R D, 1955, The Atomic Nucleus, McGraw-Hill

Girolami B, Larsson B, Preger M, Schaerf C, and Stepanek J, 1995, Photon Beam for Radiosurgery Produced by Laser Compton Backscattering from Relativistic Electron, Phys. Med. Biol. 1581-1596

Hall E J, and Giaccia A J, 2005, Radiobiology for the Radiologist, Lippincott Wiliams & Wilkins

Heintz B H, Wallace R E, and Hevezi J M, 2001, Comparison of I-125 Sources Used for Permanent Interstitial Implants, Med. Phys vol. 28 (4) 671-682

Hubbell J H and S M Seltzer, Tables of X-Ray Mass Attenuation Coefficients and Mass Energy-Absorption Coefficients from 1 keV to 20 MeV for Elements $Z = 1$ to 92 and 48 Additional Substances of Dosimetric Interest, http://physics.nist.gov/PhysRefData/XrayMassCoef/cover.html

ISP corp. 2005 Gafchromic EBT: Self-Developing Film for Radiotherapy Dosimetry

Karnas S J, Yu E, McGarry R C, and Battista J J 1999 Optimal Photon Energies for IUdR K-edge Radiosensitization with Filtered X-ray and Radioisotope Sources Phys, Med. Biol. 44 2537-2549

Kassis A I and Adelstein S J, 2005, Radiobiologic Principles in Radionuclide Therapy, Nuclear Med. 46: 4S-12S

Knoll G, 2000, Radiation Detection and Measurement, John Wiley & Sons. Inc

Kron T, Duggan L, Smith T, Rosenfeld A, Butson M, Kaplan G, Howlett S, and Hyodo K,1998, Dose Response of Various Radiation Detectors to Synchrotron Radiation, Phys Med Biol 43 (11) 3235-59

Laster B H, Thomlinson W C, and Faichild R G, 1993, Photon Activation of Iododeoxyuridine: Biological Efficacy of Auger Electrons, Radiation Research 133, 219-224

Lewis D F, Measurement Consistency and Single Pixel Noise of Two Epson Flatbed Scanners and Vidar VXR-16. available: http://www.ispcorp.com/products/dosimetry/content/gafchromic/content/products/imrtqa/pdfs/scanconno.pdf

Luxton G, 1994, Comparison of Radiation Dosimetry in Water and in Solid Phantom Materials for I-125 and Pd-103 Brachytherapy Sources: EGS4 Monte Carlo Study. Med. Phys, 21 (5) 631-641

Ma C M, Coffey C W, DeWerd L A, Liu C, Nath R, and Seltzer S M, 2001, AAPM Protocol for 40-300 kV
X-ray Beam Dosimetry in Radiotherapy and Radiobiology. Medical Physics 28 (6) 868-893

Margaritondo G, 2002, Elements of Synchrotron Light: for Biology, Chemistry, and Medical Research, Oxford University Press

Pealink L, Neve W D, and C De Wagter 2007, Precautions and Strategies in Using a Commercial Flatbed Scanner for Radiochromic Film Dosimetry, Phys Med Biol 52 231-242

Rivard M J, Coursey B M, DeWerd L A, Hanson W F, Huq M S, Ibbott G S, Mitch M G, Nath R, Williamson J F, 2004, Update of AAPM Task Group No. 43 Report: A revised AAPM protocol for brachytherapy dose calculations, Med Phys 31 (3) 633-674

Vita

Scott Oves was born and raised in Buena Park, California. He attended junior high and high school in the Anaheim Unified School District and graduated from Western High School in 2000. Also in that year, he achieved the rank of Eagle Scout from the Boy Scouts of America. The following August, he entered The University of Delaware and received a Bachelor of Science degree in physics in 2004. Since 2004, he has been enrolled in the Graduate School at Louisiana State University and is a candidate for the master's degree in medical physics.